AFRL-RY-WP-TP-2020-0068

REGISTRATION ALGORITHMS FOR FLASH INVERSE SYNTHETIC APERTURE LiDAR

John Andrew Hennen
University of Dayton

APRIL 2020
Final Report

AIR FORCE RESEARCH LABORATORY
SENSORS DIRECTORATE
WRIGHT-PATTERSON AIR FORCE BASE, OH 45433-7320
AIR FORCE MATERIEL COMMAND
UNITED STATES AIR FORCE

REPORT DOCUMENTATION PAGE

Form Approved
OMB No. 0704-0188

1. REPORT DATE *(DD-MM-YY)*
April 2020

2. REPORT TYPE
Thesis

3. DATES COVERED *(From - To)*
11 December 2019 –11 December 2019

4. TITLE AND SUBTITLE
REGISTRATION ALGORITHMS FOR FLASH INVERSE SYNTHETIC APERTURE LiDAR

5a. CONTRACT NUMBER
FA8650-12-D-1377

5b. GRANT NUMBER

5c. PROGRAM ELEMENT NUMBER
62204F

6. AUTHOR(S)
John Andrew Hennen

5d. PROJECT NUMBER
2003

5e. TASK NUMBER
N/A

5f. WORK UNIT NUMBER
Y0TW

7. PERFORMING ORGANIZATION NAME(S) AND ADDRESS(ES)

University of Dayton
300 College Park
Dayton, OH 45469

8. PERFORMING ORGANIZATION REPORT NUMBER

9. SPONSORING/MONITORING AGENCY NAME(S) AND ADDRESS(ES)

Air Force Research Laboratory
Sensors Directorate
Wright-Patterson Air Force Base, OH 45433-7320
Air Force Materiel Command
United States Air Force

10. SPONSORING/MONITORING AGENCY ACRONYM(S)
AFRL/RYMM

11. SPONSORING/MONITORING AGENCY REPORT NUMBER(S)
AFRL-RY-WP-TP-2020-0068

12. DISTRIBUTION/AVAILABILITY STATEMENT
Approved for public release; distribution is unlimited.

13. SUPPLEMENTARY NOTES
PAO case number 88ABW-2019-5931, Clearance Date 11 December 2019. © 2020 University of Dayton. Dissertation submitted to The School of Engineering of the University of Dayton in partial fulfillment of the requirements for the Degree Ph.D. in Electro-Optics. This work was funded in whole or in part by Department of the Air Force. The U.S. Government has for itself and others acting on its behalf an unlimited, paid-up, nonexclusive, irrevocable worldwide license to use, modify, reproduce, release, perform, display, or disclose the work by or on behalf of the U.S. Government. Report contains color.

14. ABSTRACT

This research demonstrates registration algorithms specific to Inverse Synthetic Aperture LiDAR (ISAL) complex data volumes. Two registration approaches are considered, a mutual information registration algorithm (MIRA) and an enhanced, range bin-summed cross-correlation algorithm. For implementing these in the context of an ISAL signal, a theoretical mapping of the reflected target plane field to an aperture plane for multi-pixel detection is done. The theory for implementing both MIRA and cross-correlation enhancements is detailed and applied to a simulated sensitivity analysis that compares algorithm convergence and performance for different SNR, sub-aperture shift distances, and low pixel supports. To the best of the authors' knowledge, this is the first application of 3D complex volume mutual information registration to LiDAR aperture synthesis. The enhanced cross-correlation algorithm showed significant gain in registration operability with respect to SNR and sub-aperture shift, giving new options for potential ISAL system design. An experimental Flash LiDAR system was constructed utilizing a multi-pixel temporal homodyne detection approach for simultaneous azimuth, elevation, range and phase imaging of target and this system was used to benchmark registration sensitivity for real data volumes. This is the first known application of a fast focal plane array for low support Flash temporal homodyne LiDAR for aperture synthesis.

15. SUBJECT TERMS
lidar

16. SECURITY CLASSIFICATION OF:
a. REPORT Unclassified
b. ABSTRACT Unclassified
c. THIS PAGE Unclassified

17. LIMITATION OF ABSTRACT:
SAR

18. NUMBER OF PAGES
164

19a. NAME OF RESPONSIBLE PERSON (Monitor)
David Rabb

19b. TELEPHONE NUMBER *(Include Area Code)*
N/A

Registration Algorithms for Flash Inverse Synthetic Aperture LiDAR

Dissertation

Submitted to

The School of Engineering of the

UNIVERSITY OF DAYTON

in Partial Fulfillment of the Requirements for

The Degree

Ph.D. in Electro-Optics

by

John Andrew Hennen

UNIVERSITY OF DAYTON

Dayton, Ohio

December 2019

University of Dayton

REGISTRATION ALGORITHMS FOR FLASH INVERSE SYNTHETIC APERTURE LIDAR

Name: Hennen , John Andrew

APPROVED BY:

Matthew P. Dierking, Ph.D.
Advisory Committee Chairman
Professor Electro-Optics and Photonics

Partha P. Banerjee, Ph.D.
Committee Member Professor
and Chair Electro-Optics and Photonics

David J. Rabb, Ph.D.
Committee Member
Professor Electro-Optics and Photonics
Technical Advisor, Laser Radar Branch
Air Force Research Laboratory

Bryce E. Schumm
Committee Member
Technical Advisor, Laser Radar Branch
Air Force Research Laboratory

Edward A. Watson, Ph.D.
Committee Member
Professor Electro-Optics and Photonics

Robert J. Wilkens, Ph.D., P.E.
Associate Dean for Research and Innovation
Professor School of Engineering

Eddy M. Rojas, Ph.D., M.A., P.E.
Dean
School of Engineering

ABSTRACT

REGISTRATION ALGORITHMS FOR FLASH INVERSE SYNTHETIC APERTURE LIDAR

Name: Hennen, John Andrew
University of Dayton
Advisor: Dr. Matthew P. Dierking

This research demonstrates registration algorithms specific to Inverse Synthetic Aperture LiDAR (ISAL) complex data volumes. Two registration approaches are considered, a mutual information registration algorithm (MIRA) and an enhanced, range bin-summed cross-correlation algorithm. For implementing these in the context of an ISAL signal, a theoretical mapping of the reflected target plane field to an aperture plane for multi-pixel detection is done. The theory for implementing both MIRA and cross-correlation enhancements is detailed and applied to a simulated sensitivity analysis that compares algorithm convergence and performance for different SNR, sub-aperture shift distances, and low pixel supports. To the best of the authors' knowledge, this is the first application of 3D complex volume mutual information registration to LiDAR aperture synthesis. The enhanced cross-correlation algorithm showed significant gain in registration operability with respect to SNR and sub-aperture shift, giving new options for potential ISAL system design. An experimental Flash LiDAR system was constructed utilizing a multi-pixel temporal homodyne detection approach for simultaneous azimuth, elevation, range and phase imaging of target and this system was used to benchmark registration sensitivity for real data volumes. This is the first known application of a fast focal plane array for low support Flash temporal homodyne LiDAR for aperture synthesis.

TABLE OF CONTENTS

LIST OF FIGURES

LIST OF TABLES

LIST OF ACRONYMS

Acronym	**Description**
ADC	Analog to digital converter
AOM	Acousto-optic modulator
CR	Cross range
EO	Electro-optic
FPA	Focal Plane Array
HAL	Holographic aperture Ladar
ICP	Iterative closest points algorithm
IF	Image formation
InGaAs	Indium Gallium Arsenide
IPR	Ideal Point Response
IR	Infrared
ISAL	Inverse synthetic aperture Ladar
LFM	Linear frequency modulation
LO	Local oscillator
MTF	Modulation transfer function
MO	Master oscillator
MSE	Mean squared error

Acronym	**Description**
PDF	Probability Density Function
PHD	Phase history data
PRF	Pulse Repetition Frequency
PSF	Point spread function
RF	Radio Frequency
SAL	Synthetic Aperture LiDAR
SAR	Synthetic Aperture RADAR
SNR	Signal to Noise Ratio
SVD	Singular Value Decomposition algorithm

LIST OF SYMBOLS

Symbol	**Description**
A	Real amplitude
a_{ij}	Transformation index
ξ,	Chirp Rate
θ_0	Chirp initial frequency
BW	Bandwidth in modulated signal
c	Speed of light
D	Real aperture diameter
MSE	Mean squared error metric
E_{sig}	Complex return signal
E_{LO}	Complex local oscillator signal
f	Frequency
h	Impulse response function

Symbol	**Description**
I	Integrated signal power
IF	Intermediate frequency
k	Wavenumber
k_x, k_y, k_z	Spatial frequency
L	Length of the synthetic aperture baseline
λ	Wavelength
M, N	Pixel Dimensions
ϕ	Azimuthal angle
ψ_0	Constant phase offset
ψ_n	Uniformly distributed nth phase
$p(t)$	Transmit signal impingent on scatterers
ΔR	Range resolution
r_{fg}	Cross-Correlation between images f and g
Γ_{fg}	Cross-Correlation between f and g spectra

Symbol	**Description**
R	Range from synthetic aperture center to scene center
$\mathcal{R}_{x,y,z}$	Rotation Matrix
R_n	Range from synthetic aperture center to the nth scatter
$s(t)$	Return signal from reflecting scatterers
σ_n	Reflectivity for nth scatterer
T	Chirp pulse duration
τ	Slow-time
τ_c	Speckle Correlation time
T	Fast-time
$tilt(\tau)$	Phase tilt applied to slow time sample
θ	Roll angle
U_{synth}	Synthetic pupil
u_τ	Real optical field
$v_\perp$	Lateral target velocity

Symbol	**Description**
ω	Angular frequency
w_0	Gaussian Beam Waist
γ	Elevation angle
$x(t)$	Slow-time position of aperture
x_0	Cross-range coordinate for SA center and scene center
x_n	Cross-range position of nth target
z_0	Range from SA center to center of target area
$Z(x, y)$	Total range depth in data cube simulation.
Z	Data cube depth coordinate

CHAPTER 1

INTRODUCTION

Inverse Synthetic Aperture LiDAR (ISAL) is an active imaging technique that provides significant resolution improvement over conventional optical systems. This technique takes advantage of target motion with respect to a stationary real aperture to synthesize a larger effective aperture. The cross-range resolution of the integrated image improves beyond the real aperture's diffraction limit. Range resolution is provided by the transmitted waveform bandwidth. By tracking the spatial and temporal evolution of the phase and amplitude of a reflected optical beam, the phase history data needed for the synthetic aperture is recovered. For single pixel data collection, the phase history will be two dimensional, consisting of range and cross-range coordinates; however, in the imaging ISAL case, the PHD will be 4 dimensional where each fast-time sample is a complex volume. Integration and analysis of the phase history in the aperture plan can reconstruct the target image and describe the motion. SAL and ISAL use registration algorithms for motion compensation in order to align and re-phase the volumes for synthetic aperture image formation [1, 2].

The proposed research introduces new algorithms and techniques that characterize non-cooperative target motion for ISAL image formation sufficient to achieve improved synthetic aperture cross-range resolution. The limitations of such methods are explored and include signal to noise ratio (SNR), detection support and rotation rate.

1.1 Historical Background

Synthetic Aperture Radar (SAR) is a radar imaging technique that takes advantage of a real aperture that moves through space. The real aperture temporally samples the reflected field at different locations to synthesize a larger effective aperture. In conventional imaging, the size of the receiving aperture constrains the possible image resolution to the diffraction limit [3]. While increasing the aperture size can increase resolution, the required apertures are impractical for many applications. In common practice, the sensor platform ideally moves only in one dimension providing resolution gain in only that direction [3]. If the real aperture follows a circular trajectory, the platform rotates around the target and this is referred to as circular SAR. Inverse Synthetic Aperture Radar (ISAR), is geometrically similar to circular SAR except the target rotates and the sensor location is fixed.

The diffraction limited resolution in azimuth and elevation depends on the dimensions of the collecting aperture. The range resolution is defined by the bandwidth of the transmitted signal propagated to and from the target scene. Pulse modulation allows a long, high average power pulse to be transmitted which is then compressed to provide range resolution equivalent to the modulation bandwidth. Many different modulation schemes are in use. A commonly used waveform in synthetic aperture imaging is the Linearly Frequency Modulated (LFM) waveform. A large body of work has been developed around the use of LFM waveforms both for SAR and for SAL[1,3,4]. LFM waveforms are relatively easy to produce and provide the required range compression. LFM waveforms are flexible, ranging from sub-millimeter range resolution with selectable center frequency to multiple sparse segmented bandwidth chirps all of which can be used to increase system performance [4, 5, 6, 7].

There are some key differences between radio frequency imaging and optical frequency imaging. Techniques for RADAR were developed throughout the last century and many of these techniques have counterparts in LiDAR. Fundamental structural differences reside in data acquisition and analysis in either frequency regime. SAL baselines and interrogation times are much shorter than the SAR equivalent, leaving a much shorter coherent processing interval (CPI).

SAL/ISAL systems typically use a high temporal bandwidth single pixel photo-detector that achieves high range resolution through range compression, and high resolution, multi-pixel cross-range images are created by aperture synthesis. This is accomplished by coherently combining subsequent single pixel range images and compressing the motion-induced phase across the slow-time record.

Recently, improvements were made in range compression for spatial heterodyne systems or Holographic Aperture LADAR (HAL) [7]. Both temporal detection signal processing and spatial heterodyne signal processing can be thought of as reconstructing images from frequency content contained in interference fringes. These fringes are temporal in ISAL systems. In digital holography, the information is encoded spatially across image pixels. Typical spatial heterodyne systems utilize a larger, slower pixel array for images with two dimensions (azimuth and elevation) in cross-range. Using fast focal plane arrays, it is possible to create a “hybrid” imaging approach where the azimuth and elevation pixel support of spatial heterodyne systems are combined with the high bandwidth range compressions approaches of temporal detection SAL systems. This allows for three dimensional imaging through temporal signal processing. This “parallel “ISAL” approach has the advantages of simultaneously generating a 3D phase history data volume sample with relatively high range resolution and limited support in both cross-range dimensions. Multiple PHD volumes are combined to form the synthetic aperture. This is the approach utilized in this dissertation.

Long Range ISAL systems typically operate at low SNR and low sampling support and resolution. Each multi-pixel real aperture volume measurement, separated in slow time, will be stitched together with image registrations techniques to form the synthetic aperture. Image registration can also be utilized to compare the fields from translating or rotating targets through a variety of algorithms such as the Iterative Closest Points algorithm (ICP) or the Singular Value Decomposition algorithm (SVD) [8]. This research focuses on the development and characterization of an enhanced algorithm for two dimensional image registration utilizing a cross-correlation technique [9].

1.2 Dissertation Overview

This dissertation begins with an analytical background in ISAL, then moves to theoretical techniques for registration and multi-dimension imaging and concludes with supporting simulations and experimental methods for testing the algorithms and demonstrating a low support temporal homodyne imaging system.

Chapter 2 includes a detailed description of the ISAL signal of interest, with the necessary assumptions and approximations. The target field is propagated to the aperture plane, and the process of collecting the data at the aperture and/or image plane is presented. ISAL waveforms are presented with a description of experimental range compression and phase retrieval. The chapter ends with a brief discussion of registration algorithms and coordinate transformations used in this imaging scenario.

Chapter 3 introduces supporting theory for Mutual Information (MI) registration algorithms This includes the MI metric itself, a description of how it can be efficiently calculated, descriptions of the transformation functions relating it to image registration and an overview of possible optimization algorithms appropriate for this application.

Chapter 4 introduces the range-summed cross-correlation registration algorithm, which is a minor noise mitigation modification on the commonly used cross-correlation technique for registering complex valued images [10]. This algorithm is treated as the baseline registration approach and is used as the standard basis for comparison between MIRA and the enhanced cross-correlation algorithm. This chapter includes the metrics for comparison between the baseline algorithm and MIRA.

Chapters 5 describes the simulations employed to explore these algorithms and imaging modalities. This includes details on target design, sub-aperture field generation, range compression, detector simulation and noise addition. There are two imaging configurations included in these field simulations. The first is an aperture plane detection approach similar to that used in digital holography. It uses a large support, complex target and provides a basis for comparison to previous registration approaches. This approach is simpler to simulate than image plane integration and still generates complex data volumes for registration testing. It was the first approach as a preliminary comparison between competing registration algorithms. The baseline cross-correlation algorithm and the mutual information registration algorithms are compared through a sensitivity analysis iterating over noise, support and aperture separation. The chapter concludes with an algorithm preference and the motivation for moving forward with algorithm enhancements.

Chapter 6 introduces the enhanced cross-correlation registration algorithm for ISAL data volumes. This technique is an extension of the baseline cross-correlation technique which corrects for biases introduced by low SNR large shifts between sub-apertures. The theory behind this is detailed and the correlation function space differences are illustrated. New convergence metrics intended to directly compare performance between the enhanced cross-correlation algorithm and the baseline cross-correlation algorithm are shown.

Chapter 7 employs a sensitivity analysis between the baseline cross-correlation approach and the enhanced cross-correlation approach. The sensitivity analysis is based on an image plane coherent detection of a simulated laboratory target. This configuration is used to explore the application of the registration techniques to small detection support multi-pixel parallel SAL systems and the method is very similar in design to the sensitivity analysis comparing baseline cross-correlation with MIRA from chapter 5. This chapter concludes with a statement of expanded flexibility in ISAL imaging scenarios made possible by these algorithm enhancements.

Chapter 8 gives a detailed description of the laboratory experiment designed to validate the simulated results shown in Chapter 8. A “parallel ISAL” system with stretch processing is introduced as well as a scaled laboratory target. The scaling, between the laboratory configuration and a practical field system are presented as well.

Chapter 9 presents an overall summary of the research. The conclusions in comparing mutual information to baseline cross-correlation are brought forward and applicable reasons are given for the algorithm preference (baseline cross-correlation). The efficacy of the enhanced cross- correlation registration algorithm is summarized including the contributions for each algorithm component, the regions of applicability and the limitations of the enhancements. A summary of contributions from this dissertation to the field of coherent LiDAR aperture synthesis and possible future work.

CHAPTER 2

COHERENT LIDAR AND ISAL BACKGROUND

The goal of a 3D Coherent ISAL system is to reconstruct an image with the best possible range and cross-range resolution, that might otherwise be limited by the diffraction limit (which limits CR resolution) or system bandwidth (which limits range resolution). Overcoming the diffraction limit as a strategy for CR resolution gain is most attractive at long ranges, when the diffraction limited spot interrogating a target is large. At long ranges, signal to noise ratio, SNR also becomes important. The laser power required to detect a signal at a particular range can be solved from the LiDAR range equation:

$$P_R = \frac{P_T \sigma}{A_{illum}} \; \frac{A_{rec}}{\pi R^2} \eta_{sys} \eta_{atm} \, , \tag{1}$$

where the variables are defined. From inspecting Eq. (1),it is clear that a continuous waveform gives a higher overall SNR. The range resolution of a LiDAR system follows

$$\Delta z_p = \frac{c}{2BW} \;\; \Delta R = \frac{c}{2BW} \, , \tag{2}$$

where $\Delta z_p$is the distance between range planes z_p , BW is the system bandwidth, and c is the speed of light. For a system using unmodulated pulses, the limiting and bandwidth is proportional to the pulse width.

A powerful technique to achieve high resolution returns with continuous waveform offering better possible SNR is range compression through waveform angle modulation where the waveform bandwidth is expanded There are a number of options available for frequency modulation that are suited to specific applications. This chapter is devoted to the LFM homodyne detection technique, where temporal fringes in the signal are obtained by mixing the return signal with a path-matched copy of itself, or local oscillator (LO). This process is also known as Stretch-Processing. This signal mixing will return high resolution range information on the target and has the advantage of operating as matched filter for parsing low SNR signals as well. ISAL requires careful phasing between sub-apertures and therefore requires coherent processing, where the phase along with the amplitude is measured. Stretch processing is a coherent processing technique and therefore is a viable method for gathering the phase information necessary for aperture synthesis. The output of this process, when applied to a multi-pixel system is a complex valued data volume. The azimuth cross-range, elevation cross-range, range and phase information in this data volume may be processed over an ISAL coherent processing interval (CPI) for improved cross-range resolution. Volumetric data registration over the CPI is what makes an ISAL imaging approach possible. This chapter begins with a description of ISAL systems, underlying general assumptions, and assumptions for the particular imaging scenario of interest. A detailed mapping between the target space signal and the aperture/image space recovered signal is made, taking into account target range and rotation and this volumetric signal may be treated as general.

2.1 Circular Synthetic Aperture LiDAR and ISAL

The resolution of conventional imaging systems is limited by the finite size of the collecting aperture. Large monolithic apertures can be impractical even when operating at optical frequencies. To overcome the aperture size limitations, synthetic aperture techniques may be used of which, there are several operating modes such as strip-map mode and spotlight mode [1].

For high resolution imaging of targets of interest, spotlight mode is required, where the optical beam continuously illuminates the same target region and signal returns are collected at different angles as the receive aperture moves. If the system is moving in an arc around the target with constant range over time, this is referred to as circular SAL [3] as shown in Figure 1.

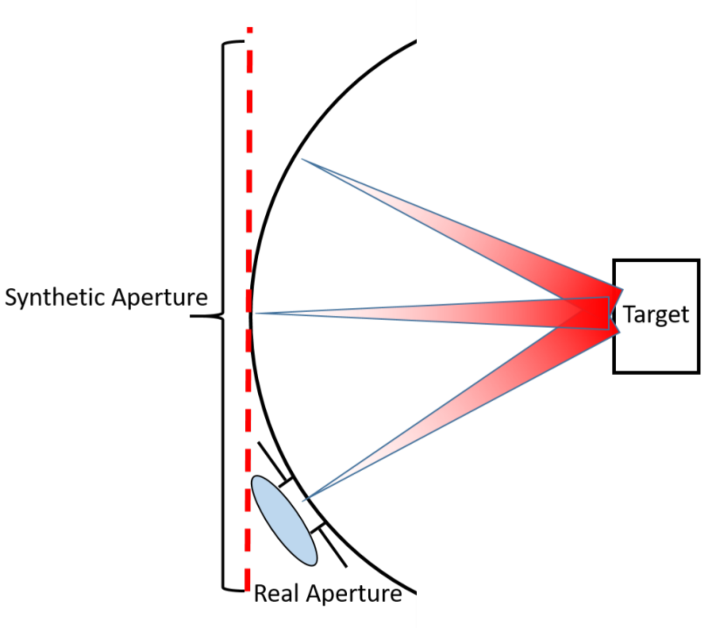

Figure 1: Circular SAL diagram: The interrogating beam keeps a constant range from the center of the target, and follows a circular trajectory. For very small angles, this trajectory can be approximated as linear instead.

Following the concepts above, the circular baseline of the sensor forms the synthetic apertures, with range and spot on target kept constant. A longer baseline can increase resolution as long as the sub apertures can still be phased. In ISAL, the target's rotation with respect to a stationary detector creates the angular diversity needed for resolution gain. If there is an effective circular path between the target center and the observation points, spotlight circular SAL and ISAL can be modeled equivalently. To form a SAL or ISAL image, a series of fast-time range profiles of the target are recorded employing temporal coherent detection. The fast-time records collected for each subsequent interrogating pulses form the slow-time samples which are combined to create a synthesized aperture.

An aperture is synthesized by registering the measured pupil volumes in three dimensions referred to as along-track (AT), cross-track (CT) and range where CT is the dimension with resolution gain. A simplified diagram of an AT collection is illustrated in Figure 2

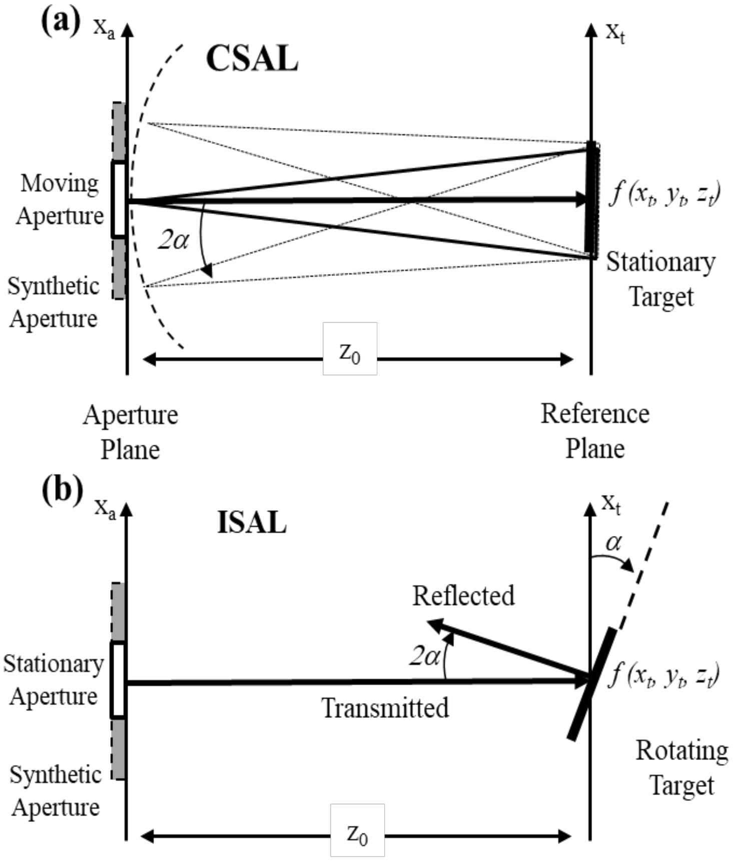

Figure 2: Sensor/Target nomenclature for CSAL and ISAL: a)Circular SAL (CSAL) has a transmit aperture interrogate a target ($f(x_t, y_t, z_t)$ at distance z_0 along a circular trajectory. b) ISAL is mathematically equivalent with the target rotating an angle α, resulting in a 2α reflection angle at the aperture.

CSAL and ISAL are directly compared in the figure, where an angle of rotation α of the ISAL target reflectivity function $f(x_t,y_t,z_t)$ will rotate the field at the aperture by 2α due to reflection and this will be collected at different effective aperture coordinates (x_a,y_a). CSAL, due to a circular baseline keeps the rotating target impingent on a flat and stationary surface. The interrogating source is in this case is a laser, which means that the signal will be speckled.

Speckle is a coherent light phenomenon that arises from wavelength order roughness on a surface, which imparts arbitrary phase onto reflected or transmitted light. While the intensity variation appears random in nature, it is actually a deterministic property of rough reflecting surfaces and is trackable. It is the speckle field, integrated in a finite aperture that composes the initial pre-processed image. This method depends on speckle correlation time and limits maximum target velocity and will constrain the interrogation time on the target. To synthesize an aperture, the speckle fields collected from different slow-time samples need to be properly registered. For multi-pixel systems, image registration algorithms can accomplish this. Image registration is most commonly used to stitch sub-images together such as in the creation of panoramic images, but can also be applied to aperture synthesis and motion tracking. There are many options available for registration [11], one approach is through maximization of mutual information between reference and test images. Another powerful algorithm is a cross-correlation technique which directly calculates registration parameters without the need to optimize a cost function. For the case of rotation about the x and y axes, the aperture field, *g*, is collected for a single range bin and slow-time sample location, $g(x_a\text{-}\alpha\tau, y_a\text{-}\beta\tau; z_p, \tau)$ is related to the target field through a Fourier transform pair following

$$g(x_a - \alpha\tau, y_a - \beta\tau; z_p; \tau) \Leftrightarrow g(x_t, y_t; z_p)\exp\left[-2\pi j(x_t\alpha\tau + y_t\beta\tau)\right], \tag{3}$$

where z_p is the target range bin location, α and β are the azimuth and elevation angles of rotation respectively and τ is the time sampling done between sub-apertures, referred to as “slow-time”. Equation (3) shows the aperture field is shifted proportionally to the rotation induced phase tips/tilts in the target plane this assumes a “Stop and Hop” model, where the constant rotation of a target is sampled with each fast-time waveform at each discrete slow-time sample of the propagated field. To synthesize an aperture, the range compressed complex volumes measured at each slow-time location are registered combined into a larger 3D composite. Each plane of the volume is created as in Figure 3

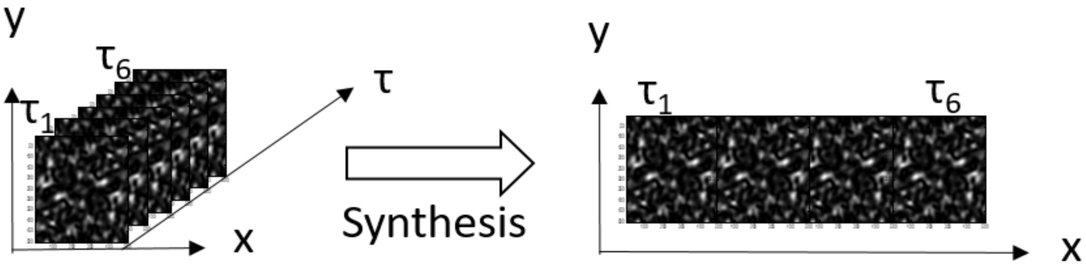

Figure 3: Single range plane aperture synthesis example. Sub-Aperture Samples are collected between times τ_1 and τ_6 .

From the figure, speckle field samples collected at subsequent slow-time coordinates are re-organized to a coherent synthesized larger speckle fields. Once synthesized a larger overall aperture results, leading to higher resolution in the dimension of synthesis.

2.2 Volumetric ISAL

This dissertation considers low support complex volume registration methods applied to remote LiDAR data for use in 3D imaging. This specific scenario comes with exploitable target motion assumptions which can be used to more easily and concisely model the field evolutions in the aperture.

2.2.1 Target and Assumptions

The imaging scenario of interest is of a rigid body at a relatively long range. Therefore there are some basic assumptions for such a target that will affect the measurement model.

Assumption 1: **Rigid Body**: All scatterers are bound and no intra target motion occurs. Any movement of one scatterer will affect the other scatterers instantaneously.

Assumption 2: Constant Motion: The target is assumed to have constant angular motion in any one direction. This means tilts in phase between slow-time samples is attributed only to scatterer distance from rotation center and not target acceleration.

Assumption 3: Small Motion: The target undergoes small motions, on the order of 1 degree per second, such that time between successive frames of the target is not large enough to cause speckle de-correlation, i.e, the speckles in the aperture plane will move less than the physical aperture. In addition, there will be no discernable motion of scatterers between range bins in the collected signal.

Assumption 4: **Aberration Free**: Turbulence is not included in this analysis. The models and assume perfect, aberration free propagation of the reflected speckle field from the target. Shot noise and thermal noise are included.

The overall theoretical and experimental approach to characterizing target motion, and image reconstruction techniques, are based on these assumptions. To form an inverse synthetic aperture, the target is observed as it undergoes rotations (tip and/or tilt) with motion slow enough to be tracked consistently. This produces a nearly linear phase shift across the spatially resolved phase history. Rotation about the optical axis, or “Roll” will not be considered for this application. The ranges of detection give tip and tilt motions a much greater effect on the field evolution at the aperture plane. While roll may be applied for separate target state estimation applications, it is typically ignored in aperture synthesis techniques.

2.2.2 Volumetric Rotating Target

The signal in Eq. (3) will be affected by target rotation. The motion of the scatterers in a rotating target is dependent on the position of the scatterer with respect to the target center and the target’s rotation rate and axes.

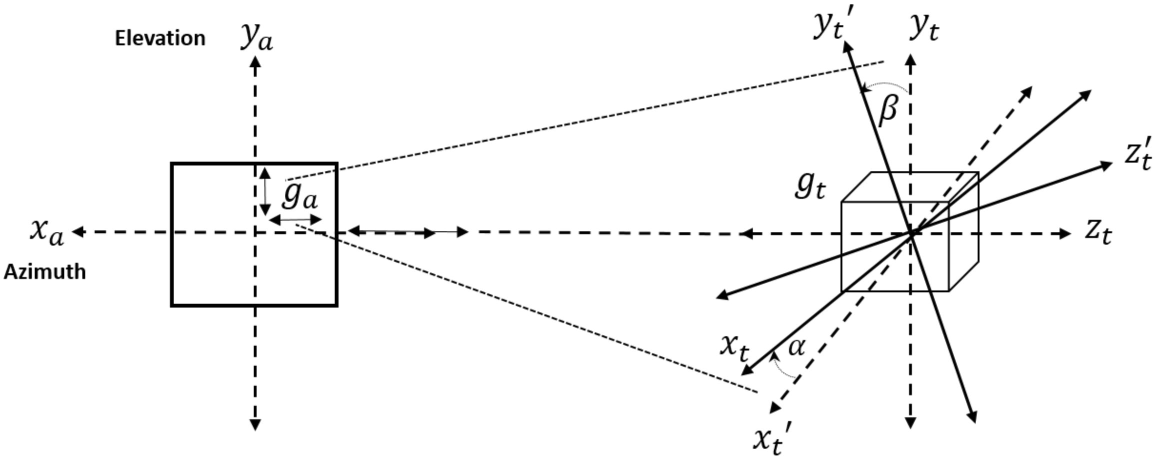

Figure 4: Point cloud rotation sampled in a 2D aperture plane. Target plane coordinate transformation between $x_t$and x_t' depends on azimuth angle rotation α and coordinate transform between $y_t$and y_t' depends on β . Transform between $z_t$and z_t' coordinates is also affected by azimuth and elevation rotation. The field at the target is g_t and the field at the aperture is g_a , where detected 2D field motion at the aperture is mapped to 3D motion of the target.

Expanding on the two dimensional ISAL sampling shown in Figure 2, Figure 4 shows how a 3D target, rotating simultaneously in elevation and azimuth (ignoring roll) shifts the collected field at the aperture plane.). This rotation can be modeled as a coordinate change from coordinates (x_t, y_t, z_t) to (x_t', y_t', z_t'), which will have an effect on the reflected field collected at range R from the target by a 2D detector with high temporal bandwidth at aperture coordinates (x_a, y_a) about an axis is described by rotation matrices the targets original coordinate system as

$$\mathrm{R}_x = \begin{bmatrix} 1 & 0 & 0 \\ 0 & \cos\alpha & -\sin\alpha \\ 0 & \sin\alpha & \cos\alpha \end{bmatrix} \qquad \mathrm{R}_y = \begin{bmatrix} \cos\beta & 0 & \sin\beta \\ 0 & 1 & 0 \\ -\sin\beta & 0 & \cos\beta \end{bmatrix}, \tag{4}$$

where R_x is azimuth rotation (about the y axis) and R_y is elevation rotation (about the x axis) where α, and β are the rotation angles about x,y, and z, respectively. This analysis will deal with small rotation angles and rates, and therefore falls under the paraxial (small angle) approximation allowing the revision of these matrices to

$$\mathrm{R}_x \approx \begin{bmatrix} 1 & 0 & 0 \\ 0 & 1 & -\alpha \\ 0 & \alpha & 1 \end{bmatrix} \qquad \mathrm{R}_y \approx \begin{bmatrix} 1 & 0 & \beta \\ 0 & 1 & 0 \\ -\beta & 0 & 1 \end{bmatrix}. \tag{5}$$

For multi-dimensional rotation (ignoring roll) the composite rotation matrix is a linear combination of the other two, following

$$R_{xy} = R_x R_y = \begin{bmatrix} 1 & 0 & \alpha \\ \alpha\beta & 1 & -\beta \\ -\alpha & \beta & 1 \end{bmatrix}. \tag{6}$$

A transformation coordinates (x_t, y_t, z_t) to (x_t', y_t', z_t') due to rotation can be expressed by

$$\begin{bmatrix} x_t' \\ y_t' \\ z_t' \end{bmatrix} = R_x R_y \begin{bmatrix} x_t \\ y_t \\ z_t \end{bmatrix} = \begin{bmatrix} x_t + z_t\alpha \\ y_t + x_t\alpha\beta - z_t\beta \\ z_t + y_t\beta - x_t\alpha \end{bmatrix}, \tag{7}$$

where the new coordinates of a scatterer are proportional to the angular rotations of the axes, and the scatterers original position. As an example, consider a rotation about the Y axis, corresponding to a tilt or yaw in the target

$$\begin{bmatrix} x_t^{'} \\ y_t^{'} \\ z_t^{'} \end{bmatrix} = \begin{bmatrix} 1 & 0 & \beta \\ 0 & 1 & 0 \\ -\beta & 0 & 1 \end{bmatrix} \begin{bmatrix} x_t \\ y_t \\ z_t \end{bmatrix} = \begin{bmatrix} x_t - \beta x_t \\ y_t \\ z_t + \beta z_t \end{bmatrix}. \tag{8}$$

Following Eq.(8), (x_t, y_t, z_t) has new coordinates (x_t', y_t', z_t') after rotation where these new coordinates will be perturbations in the original x_t and z_t by ± β factors. Following the prescribed motion assumptions, such small perturbations will not be enough to produce any change in coordinates, i.e., the scatterers will not move significantly within a range or cross-range bin. However, this small perturbation can be detected through phase changes within a range and cross range bin. By comparing the phase of identical resolution cells of the data cube between chirp pulses, a phase tilt will emerge with largest changes in phase at the points farthest from the target center of rotation.

For a system with range resolution limited to bins of width Δz_p as shown in Eq. (2), the continuous range to each scatterer can be written

$$z_t + z_0 = \left(z_t - z_p\right) + z_p + z_0 \ , \tag{9}$$

where $(z_t - z_p)$ is the distance of the scatterer within the p^th^ range bin.

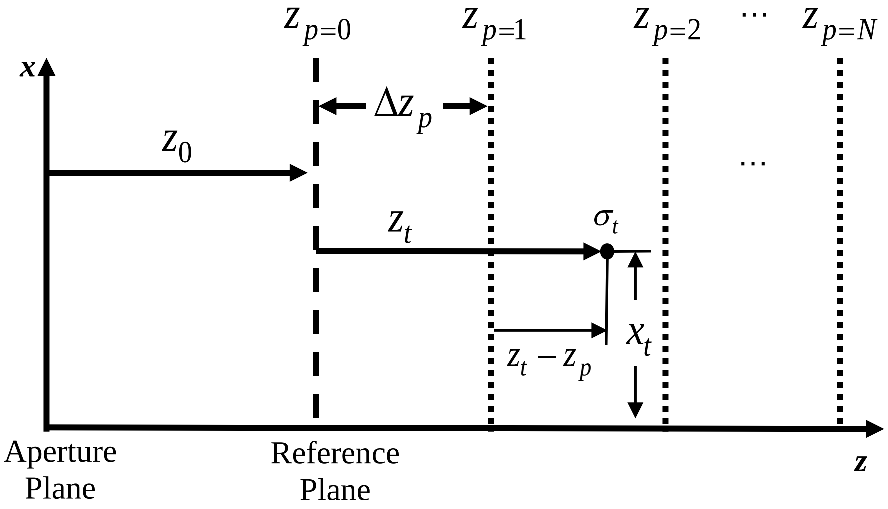

Figure 5: Geometry for propagation distance between continuously distributed scatterers in segmented range bin samples and the aperture plane.

From the figure, the reference plane $z_{p=0}$ is in the target vicinity and located a distance from the aperture plane of z_0. The target scatters have a cross-section σ_t at locations (x_t, y_t, z_t), where y_t is omitted from the figure for clarity. The distance between measurable range bins, Δz_p , dictated by the range resolution of the system following Eq. (2)

2.3 Reflected Field at the Target

The propagation begins with a transmitter located at the center of the aperture plane (x_a, y_a, z_a) which illuminates a continuous volume target, $f_c(x_t, y_t, z_t)$, defined as

$$f_c\left(x_t, y_t, z_t\right) = \sigma_t\left(x_t, y_t, z_t\right), \tag{10}$$

where $\sigma_t (x_t ,y_t ,z_t)$ is the scattering cross section at location $\left(x_t, y_t, z_t\right)$ in the target volume. For the case of illumination by perfect plane waves, the phase difference between the field at the transmitter and detector will be purely piston.

2.3.1 Transmit Phase

For practical systems with finite phase curvature over finite propagation distances, there is an additional curvature term in the phase of the field illuminating the target following illustrated in Figure 6

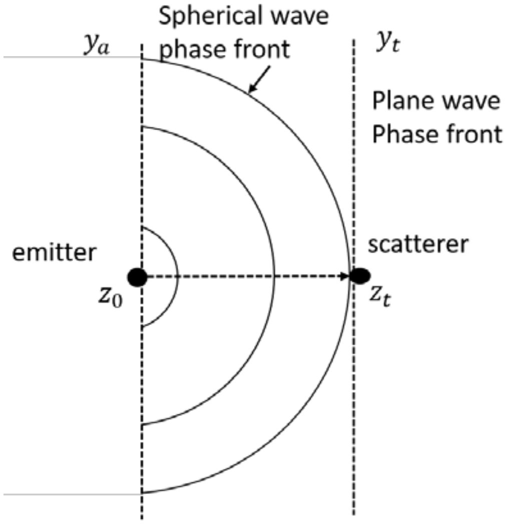

Figure 6: Illumination Phase demonstration, where phase differences occur between a real spherical wave illumination and plane wave illumination at the target. The orthogonal x_a, x_t planes at the aperture and scatterer are omitted for clarity.

For finite fields and propagation distances the field at the target immediately after reflection and before propagation back to the aperture plane is defined as

$$g(x_t, y_t, z_t) = f_c(x_t, y_t, z_t)\exp\left[jk(z_t + z_0) + \frac{jk}{2(z_t + z_0)}(x_t^2 + y_t^2) \right], \qquad (11)$$

where k is the wavenumber. The first phase term in Eq. (11) is due to the total range to from the aperture to the scatterer, (z_t + z_0), and the second is the quadratic phase of the transmitted beam incident on the target.

2.3.2 Field for Rotating Targets

For a constantly rotating target, inter-slow time sampled collection of the shifting speckle pattern will move across the aperture as through scatterer position shifted by a fixed amount dependent on scatterer location relative to the center of rotation. This motion is described through rotation matrices:

$$R_{xy} = R_x R_y = \begin{bmatrix} 1 & 0 & \alpha \\ \alpha\beta & 1 & -\beta \\ -\alpha & \beta & 1 \end{bmatrix} \rightarrow \begin{bmatrix} x_t' \\ y_t' \\ z_t' \end{bmatrix} = R_x R_y \begin{bmatrix} x_t \\ y_t \\ z_t \end{bmatrix} = \begin{bmatrix} x_t + z\alpha \\ y_t + x_t\alpha\beta - z_t\beta \\ z_t + y_t\beta - x_t\alpha \end{bmatrix}, \qquad (12)$$

where α and β are the azimuthal and elevation angles respectively and the usual sine and cosine terms have taken their paraxial representations. If higher order angular contributions to coordinate transformation are ignored, then order of rotation matrix multiplication does not matter and the rotation matrix associated with small azimuth and elevation translations is

$$\begin{bmatrix} x_t' \\ y_t' \\ z_t' \end{bmatrix} \approx \begin{bmatrix} 1 & 0 & \alpha \\ 0 & 1 & -\beta \\ -\alpha & \beta & 1 \end{bmatrix} \begin{bmatrix} x_t \\ y_t \\ z_t \end{bmatrix} = \begin{bmatrix} x_t + z_t\alpha \\ y_t - z_t\beta \\ z_t + y_t\beta - x_t\alpha \end{bmatrix}, \qquad (13)$$

which gives a phase shift on the rotating target scatterers following

$$\Delta\psi_{rot}(x_t, y_t, z_t) = \exp\left[2jk\left(\alpha x_t - \alpha z_t\right)\right]\exp\left[2jk\left(-\beta y_t + \beta z_t\right)\right]. \tag{14}$$

To translate this phase shift to terms applicable to finite resolution range bins consider the differences in phase shifts undergone by scatterers at real range coordinates z_t with scatterers at the approximated coordinates centered on a singular range bin z_p. It is the phase shift over slow-time due to rotation that is of interest and not the exact phase of scatterers with respect to the reference or target planes that is important. The first real measurement in slow-time of the target will yield an arbitrary modulo 2π phase. The next slow-time measurement provided α and β are small enough that no target scatterers move more than one wave out of phase from the previous location, will return an equivalent phase evolution term as in Eq.(14), but with respect to the finite range bins, or

$$\Delta\psi_{rot}(x_t, y_t; z_p) = \exp\left[2jk\left(\alpha x_t - \alpha z_p\right)\right]\exp\left[2jk\left(-\beta y_t + \beta z_p\right)\right]. \tag{15}$$

2.4 Fresnel Propagation from Target Field to Aperture Field

A standard method of modeling a propagating field between two planes separated in range is the Fresnel, or near-field approach. This approach employs reasonable approximations to a Green's function integral approach and retains accuracy in the far-field as well as the relatively near field. For clarity, this process will be separated into a simple, stationary target propagation between planes, employing the target model and fields shown so far. This will then be expanded to the case of rotating targets, where the contributing phase terms in the propagation follow Eq. (15)

2.4.1 Stationary Target Propagation

Rewriting the target field given in Eq. (11) in terms of the discrete range bins yields

$$g(x_t, y_t, z_t) = f_c(x_t, y_t, z_t)\exp\left[jk\left(\left(z_t - z_p\right) + z_p + z_0\right) + \frac{jk}{2\left(\left(z_t - z_p\right) + z_p + z_0\right)}(x_t^2 + y_t^2) \right], \quad (16)$$

where the first phase term is the piston phase associated with propagation from the aperture plane to the target scatterer. Separating the range bin distance, $(z_t - z_p)$, from the first exponential term and recognizing that it is small with respect to $(z_p + z_0)$ in the denominator of the second term, the field is rewritten as

$$g(x_t, y_t, z_t) \approx f_c(x_t, y_t, z_t)\exp\left[jk\left(z_t - z_p\right)\right]\exp\left[jk\left(z_p + z_0\right) + \frac{jk}{2\left(z_p + z_0\right)}(x_t^2 + y_t^2) \right], \quad (17)$$

where the first exponential factor is due to the distance within the range bin. Combining the continuous target function, $f_c(x_t,y_t,z_t)$, with the intra-range bin phase, the target, $f\,(x_t,y_t;z_p)$, is described in terms of the discrete range bins as

$$f\left(x_t, y_t; z_p\right) = f_c(x_t, y_t, z_t)\exp\left[jk\left(z_t - z_p\right)\right] = \sigma_t\left(x_t, y_t; z_p\right)\exp\left[jk\left(z_t - z_p\right)\right]. \quad (18)$$

The range bin phase factor is modulo 2π based on the wavelength, and may rotate through many cycles within each range-bin. Inserting Eq.(18) into Eq.(17), the target field at each range bin is

$$g(x_t, y_t; z_p) = f(x_t, y_t; z_p)\exp\left[jk(z_p + z_0) + \frac{jk}{2(z_p + z_0)}(x_t^2 + y_t^2) \right], \quad (19)$$

where the intra-range bin phase for each scatterer is incorporated into the target function $f(x_t, y_t; z_p)$. For a single slow-time sample, the goal is to map the stationary target field of Eq. (17) to the aperture plane. The Huygens approximation may be utilized to propagate a field through space following

$$g(x_a, y_a; z_p) = \frac{z_0}{j\lambda} \iint_{\Sigma} f(x_t, y_t; z_p) \frac{\exp(jkr_{ta})}{r_{ta}{}^2} dx_t dy_t \,, \tag{20}$$

where λ is the wavelength, and the range from a point to the target volume in the aperture plane is

$$\begin{aligned} r_{ta} &= \sqrt{(x_a - x_t)^2 + (y_a - y_t)^2 + (z_0 + z_p)^2} \\ &= (z_0 + z_p)\sqrt{1 + \left(\frac{x_a - x_t}{z_0 + z_p}\right)^2 + \left(\frac{y_a - y_t}{z_0 + z_p}\right)^2} \quad . \end{aligned} \tag{21}$$

Using the binomial expansion, the range to the aperture plane from a single finite range bin z_p on target is

$$r_{ta}(x_a, y_a; z_p) = \left(z_p + z_0\right)\left[1 + \frac{x_t{}^2}{2\left(z_p + z_0\right)^2} + \frac{y_t{}^2}{2\left(z_p + z_0\right)^2}\right] = (z_p + z_0) + \frac{1}{2}\left[\frac{x_t{}^2}{\left(z_p + z_0\right)} + \frac{y_t{}^2}{\left(z_p + z_0\right)}\right]. \tag{22}$$

This binomial expansion is the basis for the Fresnel approximation of this propagation approach or

$$g(x_a, y_a; z_p) = \iint f(x_t, y_t, ; z_p) \exp\left\{\frac{jk}{2\left(z_p + z_0\right)}\left[\left(x_a - x_t\right)^2 - \left(y_a - y_t\right)^2\right]\right\} dx_t dy_t \,. \tag{23}$$

Equation (23) can be written as the convolution

$$g(x_a, y_a; z_p) = \iint f(x_t, y_t; z_p) h(x_a - x_t, y_a - y_t; z_p) dx_t dy_t . \tag{24}$$

with the free space impulse response of

$$h(x_t, y_t; z_p) = \frac{\exp\left[jk\left(z_p + z_0\right)\right]}{j\lambda\left(z_p + z_0\right)} \exp\left\{\frac{jk}{2\left(z_p + z_0\right)}[x_a{}^2 + y_a{}^2]\right\} . \tag{25}$$

Substituting Eq. (25) into Eq. (24) and following the Fresnel approach above yields the field at the aperture

$$\begin{aligned} g\left(x_a, y_a; z_p\right) = \frac{\exp\left[jk(z_p + z_0)\right]}{j\lambda(z_p + z_0)} \iint_{-\infty}^{\infty} f\left(x_t, y_t; z_p\right) \exp\left[jk(z_p + z_0) + \frac{jk}{2(z_p + z_0)}\left(x_t{}^2 + y_t{}^2\right)\right] \\ \times \ \exp\left\{\frac{jk}{2(z_p + z_0)}\left[\left(x_a - x_t\right)^2 + \left(y_a - y_t\right)^2\right]\right\} dx_t dy_t . \end{aligned} \tag{26}$$

2.4.2 Contribution of rotation to aperture field

Inserting the phase contribution due to coordinates rotation of Eq. (15) into Eq. (26) gives

$$\begin{aligned} g\left(x_a, y_a; z_p\right) = \frac{\exp\left[jk\left(z_p + z_0\right)\right]}{j\lambda z_p + z_0} \iint f\left(x_t, y_t; z_p\right) \exp\left[k\left(z_p + z_0\right) + \frac{k}{2\left(z_p + z_0\right)}\left(x_t{}^2 + y_t{}^2\right)\right] \\ \times \exp\left\{2k\left[\alpha x_t - \alpha z_p\right]\right\} \exp\left\{2k\left[-\beta y_t + \beta z_p\right]\right\} \\ \times \exp\left\{\frac{jk}{2(z_p + z_0)}\left[\left(x_a - x_t\right)^2 + \left(y_a - y_t\right)^2\right]\right\} dx_t dy_t , \end{aligned} \tag{27}$$

where the second line is due to target rotation. Expanding the convolution term:

$$
\begin{aligned}
g\left(x_a, y_a; z_p\right) = \frac{\exp\left[j\frac{2\pi}{\lambda}\left(z_p + z_0\right)\right]}{j\lambda\left(z_p + z_0\right)} \iint f\left(x_t, y_t; z_p\right) & \\
\times \exp\left[k\left(z_p + z_0\right) + \frac{k}{2\left(z_p + z_0\right)}\left(x_t^{\,2} + y_t^{\,2}\right)\right] & \\
\times \exp\left\{2k\left[\alpha x_t - \alpha z_p\right]\right\} \exp\left\{2k\left[-\beta y_t + \beta z_p\right]\right\} & \\
\times \exp\left\{\frac{jk}{2\left(z_p + z_0\right)}\left[\left(x_a^{\,2} - 2x_t x_a + x_t^{\,2}\right) + \left(y_a^{\,2} - 2y_a y_t + y_t^{\,2}\right)\right]\right\} dx_t dy_t\,, &
\end{aligned}
\tag{28}
$$

and moving the exponentials unrelated to variables of intergration out of the integral yields

$$
\begin{aligned}
g\left(x_a, y_a; z_p\right) = {} & \frac{\exp\left[jk\left(z_p + z_0\right)\right]}{j\lambda\left(z_p + z_0\right)} \exp\left[\frac{jk}{2\left(z_p + z_0\right)}(x_a^{\,2} + y_a^{\,2})\right] \\
& \times \exp\left\{-2jk\left[\beta z_p - \alpha z_p\right]\right\} \exp\left[jk\left(z_p + z_0\right)\right] \\
& \times \iint f\left(x_t, y_t; z_p\right) \exp\left[\frac{k}{2\left(z_p + z_0\right)}\left(x_t^{\,2} + y_t^{\,2}\right)\right] \exp\left[2jk\left(\alpha x_t - \beta y_t\right)\right] \\
& \times \exp\left\{\frac{jk}{2\left(z_p + z_0\right)}\left[\left(-2x_t x_a + x_t^{\,2}\right) + \left(-2y_a y_t + y_t^{\,2}\right)\right]\right\} dx_t dy_t\,.
\end{aligned}
\tag{29}
$$

The squared terms in the 3rd and 4th lines of Eq. (29) are combined to get

$$
\begin{aligned}
g\left(x_a, y_a; z_p\right) = {} & \frac{\exp\left[jk\left(z_p + z_0\right)\right]}{j\lambda\left(z_p + z_0\right)} \exp\left[\frac{jk}{2\left(z_p + z_0\right)}(x_a{}^2 + y_a{}^2)\right] \\
& \times \exp\left\{-jk\left[\beta z_p - \alpha z_p\right]\right\} \exp\left[jk\left(z_p + z_0\right)\right] \\
& \times \iint f\left(x_t, y_t; z_p\right) \exp\left[\frac{jk}{\left(z_p + z_0\right)}\left(x_t^2 + y_t^2\right)\right] \\
& \times \exp\left[j\frac{k}{\left(z_p + z_0\right)}\left(2(z_p + z_0)\alpha x_t - x_t x_a - 2(z_p + z_0)\beta y_t - y_a y_t\right)\right] dx_t dy_t \,.
\end{aligned}
\tag{30}
$$

The Integral term above may be rewritten as

$$
\begin{aligned}
& \iint f\left(x_t, y_t; z_p\right) \exp\left[\frac{k}{\left(z_p + z_0\right)}\left(x_t^2 + y_t^2\right)\right] \\
& \times \exp\left\{j\frac{k}{\left(z_p + z_0\right)}\left[\left(2\alpha(z_p + z_0) - x_a\right)x_t - \left(2\beta(z_p + z_0) - y_a\right)y_t\right]\right\} dx_t dy_t \;,
\end{aligned}
\tag{31}
$$

which can be represented in terms of spatial frequencies under the substitution

$$
\rho_x = \frac{k}{\left(z_p + z_0\right)}\left[x_a - 2\alpha\left(z_p + z_0\right)\right] \qquad \rho_y = \frac{k}{\left(z_p + z_0\right)}\left[y_a - 2\beta\left(z_p + z_0\right)\right],
\tag{32}
$$

and reinsterted into Eq. (30) yielding

$$
\begin{aligned}
g\left(x_a, y_a; z_p\right) = {} & \frac{\exp\left[jk\left(z_p + z_0\right)\right]}{j\lambda\left(z_p + z_0\right)} \exp\left[\frac{jk}{2\left(z_p + z_0\right)}(x_a{}^2 + y_a{}^2)\right] \\
& \times \exp\left\{-jk\left[2\beta z_p - 2\alpha z_p\right]\right\} \exp\left[jk\left(z_p + z_0\right)\right] \\
& \iint f\left(x_t, y_t; z_p\right) \exp\left[\frac{k}{\left(z_p + z_0\right)}\left(x_t^2 + y_t^2\right)\right] \exp\left[-j\left(\rho_x x_t - j\rho_y y_t\right)\right] dx_t dy_t .
\end{aligned} \tag{33}
$$

Equation (33) is simply a 2D Fourier transform of the target field with respect to x_t and y_t with multiplicative piston phase terms outside the integral. The final field at the aperture in this scenario is then expressed as

$$
\begin{aligned}
g\left(x_a, y_a; z_p\right) = {} & \frac{\exp\left[jk(z_p + z_0)\right]}{j\lambda(z_p + z_0)} \exp\left\{-jk\left[2\beta z_p - 2\alpha z_p\right]\right\} \exp\left[jk(z_p + z_0)\right] \\
& \times \exp\left[\frac{jk}{2(z_p + z_0)}\left(x_a{}^2 + y_a{}^2\right)\right] \\
& \times F_{xy}\left\{\left(x_a - (z_p + z_0)2\alpha\right), \left(y_a + (z_p + z_0)2\beta\right); z_p\right\},
\end{aligned} \tag{34}
$$

Where the first exponential is the phase from propagating to the range bin, the second exponential is extra phase from scatterers moving in a range bin, the third and fourth exponentials are the illumination phase. And F_{xy} is the 2D Fourier transform of the target reflectivity function $f(x_t, y_t; z_p)$ Equation (34) maps the field of a slowly rotating, long distance three dimensional volume target to the aperture plane. The phase terms outside the Fourier transform contribute piston phase to the aperture plane field, while the arguments inside the transform term manifest as α and β dependent spatial shifts such as those shown in Eq. (14).

The surface roughness of many targets is on the order of the interrogating wavelength, and therefore the modulo 2π phase of the signal in Eq. (34) will lead to field interference during propagation and manifest at the aperture as a speckle pattern. For a well-designed system, the size of these speckles will be 1-2 pixels in diameter and will match the size of a back-projected diffraction limited spot on the target. The speckles themselves will consist of the raw field incident on the detector. The end result is a speckled volumetric signal collected from either the field at the aperture plane following Eq. (34), or at the image plane by focusing the field to form an image. This coherent volume signal, may still be subdivided into slow-time samples, the details of which are saved for section 2.7

2.5 Signal Detection

The final step in detection is to integrate the speckle fields into a measureable power at the detector and add noise introduced by the hardware and wave/particle nature of the photons at this step. In practice, the integration and noise addition may occur at the aperture plane for holographic systems or at the image plane for temporal systems. For imaging systems, the appropriate phase terms and Fourier transform associated with a focusing lens must be added to the aperture field before integration.

2.5.1 Aperture Plane Detection

For detection at the aperture plane, no lens is added to the system and the detected signal will be the pixel integrated propagated field of Eq.(34). This field will be cropped by a 3D aperture function which will control the 3D bandwidth of the detected field.

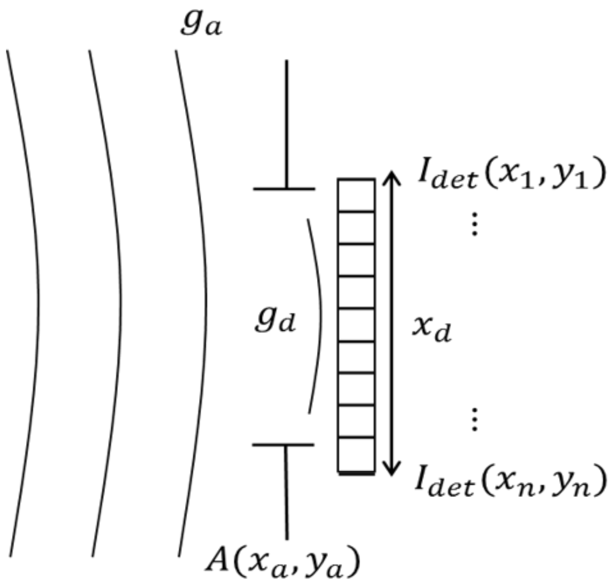

Figure 7: Aperture plane detection. The propagating field from the target immediately before the aperture is g_a, the Aperture function $A(x_a,y_a)$ samples this and the resulting lower bandwidth field is g_d. Pixels sample the field and output a current detected power or photocurrent $I_{det}(x_n,y_n)$ at each pixel location.

Aperture plane detection can also be done with a square aperture. Signal support for a square aperture is defined as the diameter, in pixels, of the aperture. A properly sampled field at the detector will have the smallest speckles still larger than a single detection pixel, and this is demonstrated in Figure 8 with a very low support case.

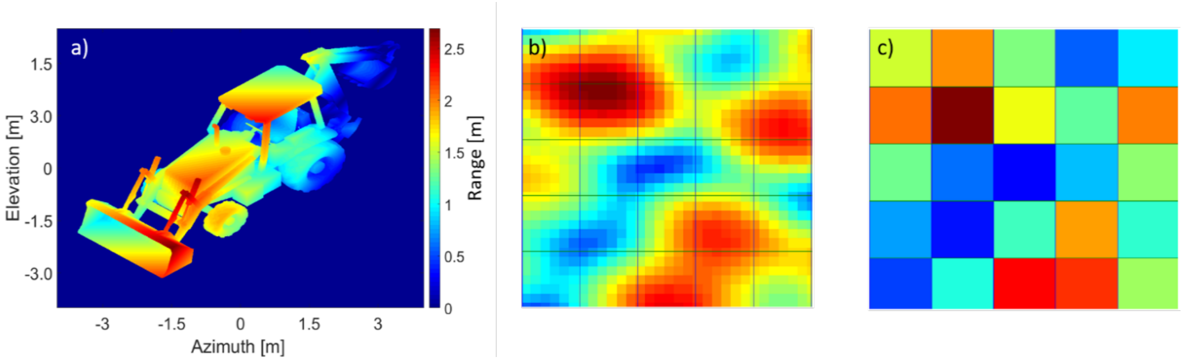

Figure 8: Nyquist sampled aperture support at 5x5 pixels for a single range bin. The 3D target is a), which is assumed to be divided into range bins. A small portion of the propagated field sampled by a square aperture is b), which shows speckles critically sampled by a 5x5 detection grid. Such a grid may be the detection pixels on a camera at the aperture plane, and after integration in the pixels c) results.

2.5.2 Spatial Integration and Detection

The finite nature of the detector means that this continuous field on the aperture plane is integrated within each of the pixels following

$$\bar{g}\left(x_p, y_p; z_p\right) = \iint g(x_a, y_{a,}; z_p)dx_a dy_a, \tag{35}$$

where $\bar{g}(x_p, y_p; z_p)$ is the range compressed power output for a real detector with column sampling x_p and row sampling y_p. Equation (35) is for a detector located at the aperture which is typical for digital holography. It may be modified for image plane integration if the aperture field is first imaged with a focusing lens.

2.6 Complex Signal Volume Recovery

After integration within the pixels on the detector array, the complex signal volume is recovered through range compression. For experimental systems, this is accomplished through an optical matched filter by convolving the return signal with a reference signal, which generates a beat signal, and taking the Fourier transform, which maps the temporal aspect of the field to frequency, corresponding to range, with bin width shown as in Figure 5, dependent on signal bandwidth following Eq. (2). For simulated complex signal volumes, the same effect is generated by creating a data volume with the specified bin number, propagating each corresponding target plane to the aperture volume and integrating the resulting field within each voxel. The result is a lower resolution complex signal volume at the aperture.

2.7 Noise at Detection

A well-designed system will be shot noise limited, but the effects of this shot-noise on algorithm accuracy and precision are primary metrics of interest. A reproducible and accurate measure of the SNR is defined as the ratio of the average power in the signal and noise

$$\mathrm{SNR} = \frac{\left| \bar{g}\left(x_p, y_p; z_p\right)^2 \right|}{\left| Noise\left(x_p, y_p; z_p\right) \right|^2}, \tag{36}$$

where the $Noise(x_p, y_p; z_p)$ volume is the same size as the signal $\bar{g}(x_p, y_p; z_p)$, but contains circularly symmetric Gaussian random noise. While shot noise follows Poisson statistics, the central limit theorem, applicable for the large number of photon detections in this type of system, allows for the noise to be modeled with a Gaussian distribution. For a given SNR, a noise data volume is generated by building a normally distributed volume and multiplying by the standard deviation, σ_{SNR}, following

$$\sigma_{SNR} = \sqrt{\frac{\bar{g}\left(x_p, y_p; z_p\right)}{2SNR}}. \tag{37}$$

The factor of 2 in the denominator is due to the application of σ_{SNR} both to the real and imaginary signal channels. Since the targets of interest have spatially dependent structure, defining a meaningful, target independent SNR is challenging. In this case the SNR is defined as the mean value over the volume. For sparsely distributed targets in normally distributed noise, the SNR for some cross range pixels (or voxels), may be significantly higher than the average value. Good registration performance may be achieved at average SNR levels below 0 dB since some signals in the data volume may have orders of magnitude greater intensity than the noise. Some pixels will see bright, plate-like scatterers for a complex target, while others will have the signal distributed between many range-bins, drastically reducing that pixel's SNR. Some pixels will have no target at all and only contribute noise to the measured signal volume.

2.8 Image Plane Detection

Image plane detection adds two more steps in the process of recovering a low resolution complex volume at the aperture. As with aperture plane detection, a 3D crop is applied to the volume at the aperture space which decreases field bandwidth. Then the field is focused, either digitally or with a lens, onto the image plane where the pixel integration takes place.

2.9 Propagation from Aperture Plane to Image Plane

Image plane detection is similar overall and incorporates a lens placed at the aperture which applies a phase curvature to field propagating through the aperture which focusses it on the image plane as shown in Figure 9

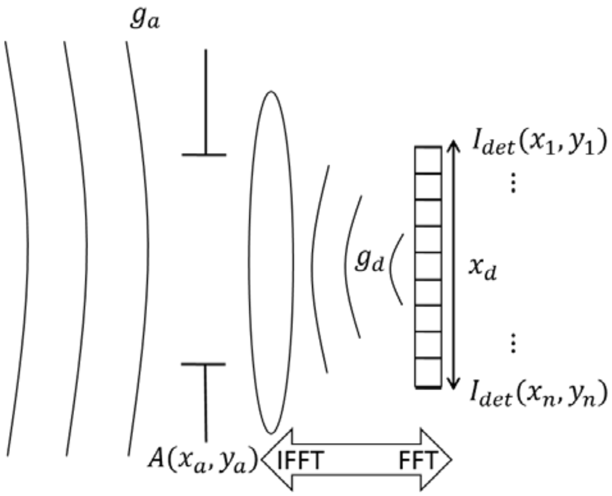

Figure 9: Image plane detection. The propagating field from the target immediately before the aperture is g_a, the Aperture function $A(x_a,y_a)$ samples this and the resulting lower bandwidth field is g_d. A lens focusses onto the detector and pixels sample the field and output a current detected power or photocurrent $I_{det}(x_n,y_n)$ at each pixel location.

From the figure, the aperture and image fields form a Fourier transform pair, and in this way the aperture fields from each range bin needed for synthesis may be obtained through a 2D inverse Fourier transform operation. The process of image plane detection from the raw field to the lower bandwidth final product is shown in Figure 10

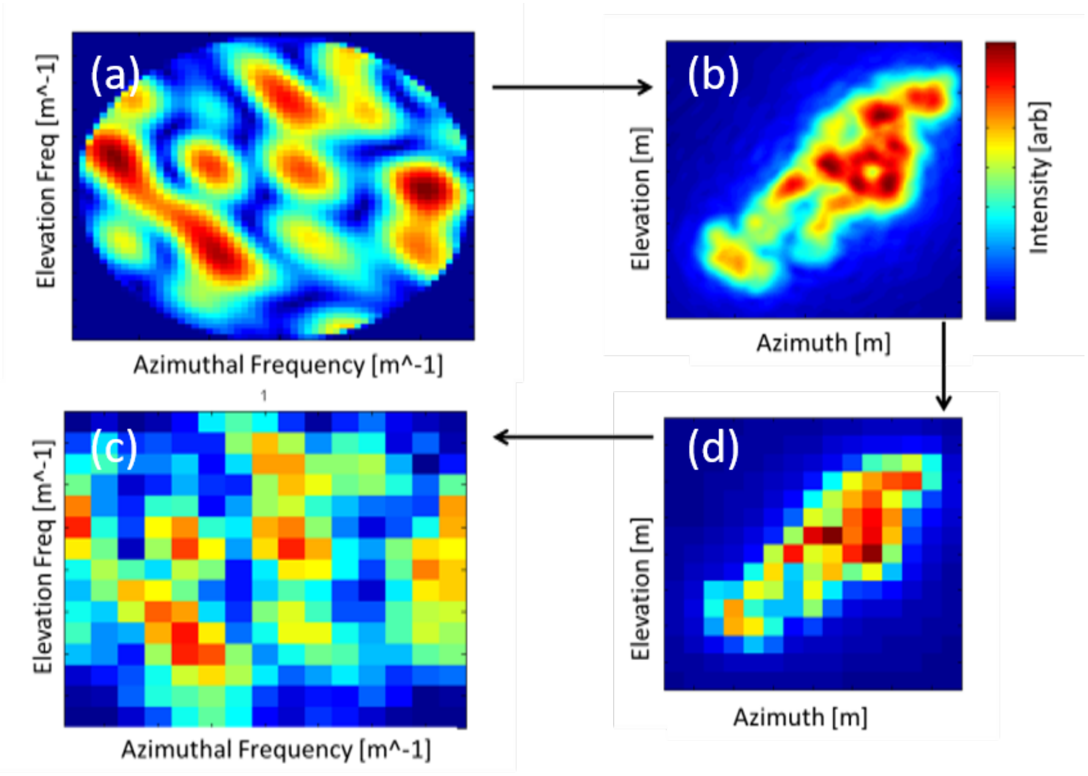

Figure 10: Process from the raw field at the aperture plane to a more realistic detected field. For image plane detection, the raw field at the aperture (a) is focused onto the detection plane as in (b). The pixels in the detector integrate this field, resulting in (c) which, once inverse Fourier transformed, recovers a lower resolution depiction (d) of the raw aperture field.

The field at the aperture is focused following

$$
\begin{aligned}
g\left(x_{\det}, y_{\det}; z_p\right) = \frac{\exp\left[-jk(z_p+z_0)\right]}{j\lambda(z_p+z_0)} \iint_{-\infty}^{\infty} & g\left(x_a, y_a; z_p\right) A\left(x_a, y_a, z_a\right) \\
& \times \exp\left[-jk(z_p+z_0) + \frac{jk}{2(z_p+z_0)}\left(x_a{}^2 + y_a{}^2\right)\right] \\
& \times \exp\left\{\frac{-jk}{2(z_p+z_0)}\left[\left(x_{\det}-x_a\right)^2 + \left(y_{\det}-y_a\right)^2\right]\right\} dx_a dy_a .
\end{aligned} \tag{38}
$$

where the field at detector coordinates (x_{det} , y_{det}) is follows an “inverse” Fresnel propagation of the field at the aperture plane which has been sampled with the aperture function $A(x_a , y_a , z_a)$.

2.10 Range Compression and the Matched Filter through Stretch Processing

The complex data volumes have been considered in the general case so far. The previous section showed how to map reflected fields at particular spatial coordinates at the target plane to their corresponding spatial coordinates at the aperture and detector planes. This section will show how the range and phase information from a scatterer reflection is encoded in the return signal and will show how to generate these data volumes from a real target using a temporal homodyne LFM stretch processed imaging system. This subsection may be thought of as a single-pixel signal analysis of such a system, where the final data volume from Eq. (34) is recovered from integrating the temporally sampled signals shown below in a multi-pixel array, and applying an inverse Fourier transform on the resultant image plane data to recover the aperture data volume.

The return signal from a group of reflective scatterers takes the form

$$s(t) = \int \sigma(z_t)\, p\left(t - \frac{2z_t}{c}\right) dz_t \qquad (39)$$
$$= \sigma\left(\frac{ct}{2}\right) \otimes p(t),$$

Where $\sigma(z_t)$ is the reflectivity function, $p(t)$ is the time dependent transmit signal seen by scatterers and $\otimes$ denotes convolution [1]. The integral takes into account the signal contributions throughout the whole range space. The time delay of $\frac{2z_t}{c}$ results from the signal delay to and from the target. Taking the Fourier transform of Eq. (39) with respect to time yields the signal spectrum

$$S(\omega) = P(\omega) \int \sigma(z_t)\, exp\left(-j\omega \frac{2z_t}{c}\right) dz_t . \qquad (40)$$

where ω is the angular frequency. Infinite bandwidth allows full recovery of the continuous target reflectivity as a function of signal time.

$$F^{-1}\left\{\frac{S(\omega)}{P(\omega)}\right\} = \int \sigma(z_t)\, \delta\left(t - \frac{2z_t}{c}\right) dz_t = \sigma\left(\frac{\mathrm{ct}}{2}\right), \qquad (41)$$

where F^{-1} denotes the inverse Fourier transform. The ability to describe the reflectivity as a continuous function would allow a perfect reconstruction of the target. Noise in the return signal is always important in remote sensing. Filtering of the noise is one way to improve the usable signal, however, any filter applied to the return signal will remove the desired signal as well. If the outbound signal is known, the noise filter that will maximize the SNR will be a filter with the shape of the original signal. This is a matched filter, and can be applied with hardware or software by convolving the return signal with a time reversed complex conjugate of the known transmit signal [12]. The matched filter signal $s_{mf}(t)$ is obtained through operation

$$\begin{aligned} s_{mf}(t) &= F^{-1}\left[S(\omega)P^{*}(\omega)\right] \\ &= F^{-1}\left[\int \sigma(z_t)\left|P(\omega)\right|^2 \exp\left(-j\omega\frac{2z_t}{c}\right)dz_t\right] \\ &= \int \sigma(z_t)psf\left(t-\frac{2z_t}{c}\right)dz_t, \end{aligned} \tag{42}$$

where $psf(t)$ is the point spread function of the signal denoted as

$$psf\left(t\right) = F^{-1}\left[\left|P\left(\omega\right)\right|^2\right]. \tag{43}$$

From the convolution theorem of Fourier transforms the matched filter is also expressed as

$$\begin{aligned} s_{mf}\left(t\right) &= s(t)\otimes p(-t) \\ &= \sigma\left(\frac{ct}{2}\right)\otimes psf(t), \end{aligned} \tag{44}$$

which is to say, the matched filter is the target reflectivity function, broadened by convolution of the transmit point spread function. Consider a constant frequency transmit pulse of length T, represented by

$$p\left(t\right) = rect\left(\frac{t}{T}\right)\cdot A\exp\left(j\omega t\right), \tag{45}$$

where A is amplitude and $rect$ is a rectangle function of pulse width T .

The return signal, shown in Figure 11, will be a time shifted version of this signal, and is commonly corrupted by white noise.

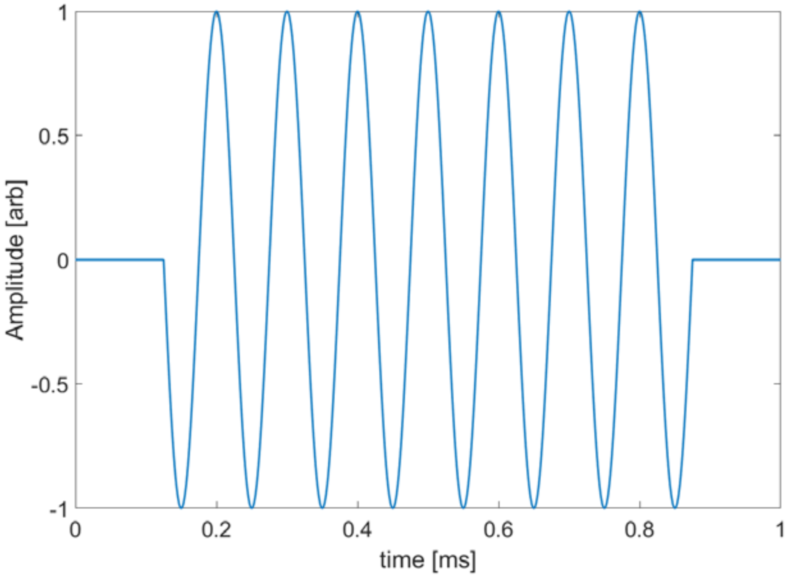

Figure 11: Consider a square windowed single frequency pulse at 10kHz, with a duration of 1 ms. Such a pulse will have an ideal point response (IPR) and a matched filter transfer function whose widths depend on the width of the single frequency pulse.

The matched filter is obtained by substituting Eq. (45) into Eq. (44), yielding.

$$s_{mf}(t) = p(t) \otimes p^*(-t) = rect\left(\frac{t}{T}\right) \cdot A\exp(j\omega t) \otimes rect\left(\frac{-t}{T}\right) A\exp(j\omega t), \tag{46}$$
$$= A^2 T\mathrm{sinc(t)exp(j}\omega\mathrm{t)}.$$

The width of the convolution is equal to the waveforms overlapping time interval. This can limit the ability to resolve close targets. As a mono-frequency pulse is bounded by a rectangle window function, generating the IPR by autocorrelation will result in a triangle function of twice the width of the pulse as shown in Figure 12,

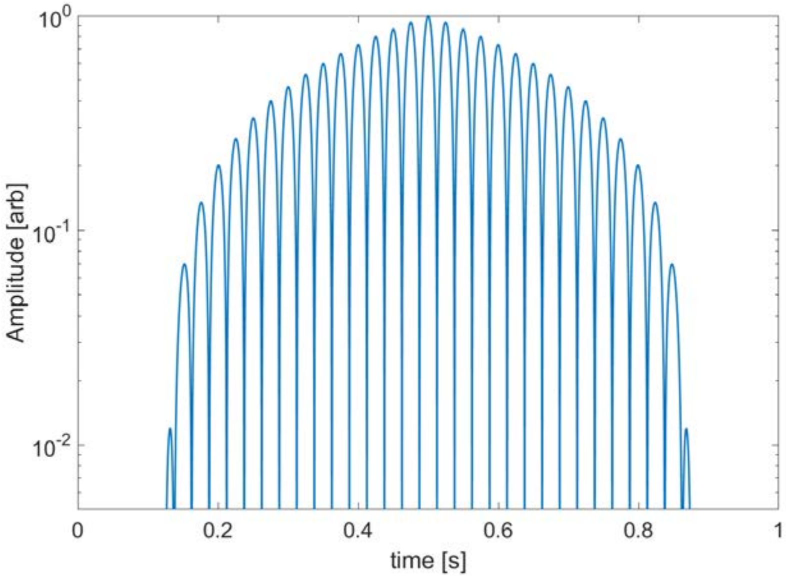

Figure 12: Log scale single frequency IPR where bandwidth is limited by the pulse width

Clearly, shorter pulses are necessary for good range resolution. As pulses get shorter, the available power to illuminate the target typically goes down as well. An LFM waveform circumvents this by having both a long pulse width and large bandwidth. The LFM waveform time dependent transmit field, $p(t)$, is given as

$$p(t) = rect\left(\frac{t}{T}\right)a(t)\exp[j\omega_0 t + j\xi t^2], \tag{47}$$

where $a(t)$ is the amplitude, ω_0 is the initial frequency and ξ is the chirp rate. An example of this waveform is shown in Figure 13, which has the same starting frequency and pulse width as the mono-frequency pulse from before.

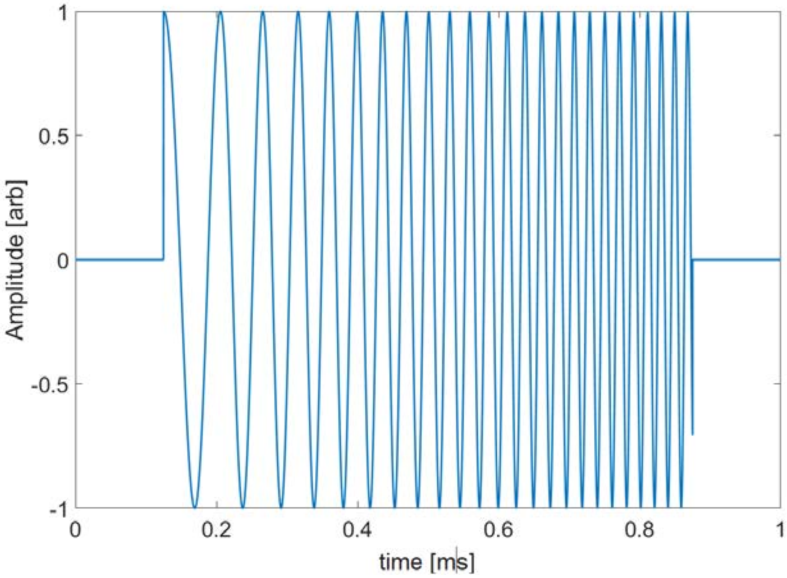

Figure 13: Chirp Pulse with same duration and starting frequency as the single frequency pulse from figure 12.

Similar analysis with an LFM waveform yields higher resolution, higher power results. It can be shown that the result of applying a matched filter to an LFM waveform yields

$$s_{mf}(t) = \sqrt{T \cdot BW}\,\mathrm{sinc}(BW \cdot t), \tag{48}$$

where the term $T \cdot BW$ is the time bandwidth product [1].

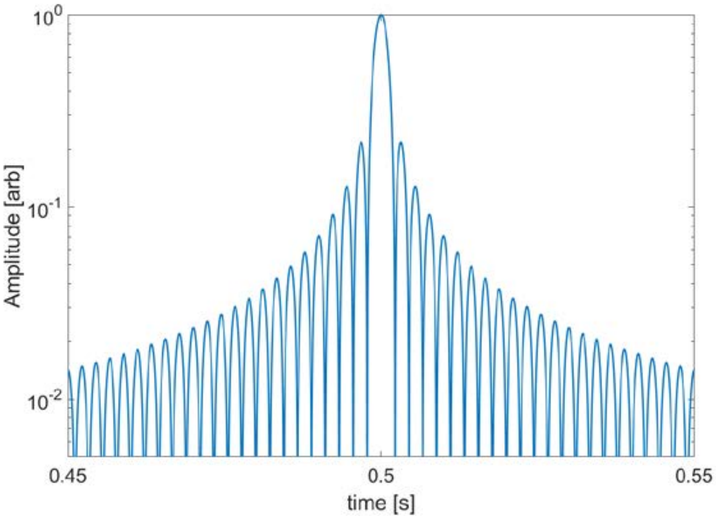

Figure 14: Log scale LFM pulse IPR. Pulse is same duration, T, as in Figure 2, but with 500 times the bandwidth.

Figure 14 shows the IPR obtained from a chirped pulse of the same length as the single frequency in Figure 12 but it has a much wider bandwidth which allows for a narrower IPR and increased range resolution. With a longer waveform, the total power is larger, and after matched filtering the resolution is still sufficient for high-resolution range imaging. For more precise tracking of targets, analysis must utilize the waveform phase. Accomplishing this with optical wavelengths presents a challenge, as the wave's phase resets after only microns (or nanometers) of travel corresponding to only picoseconds of time displacement, which can be impractical for a modern analog to digital converter (ADC).

Stretch processing is a coherent detection method for simultaneously obtaining a signal matched filter and recovering the scatterer phase. In many optical heterodyne detection schemes, the system retains copy of the initial waveform as a local oscillator and its frequency is adjusted from the master oscillator (MO) with an acousto-optic modulator (AOM). If the MO and LO are mixed, the frequency of the resulting signal will be at the offset frequency of the AOM and is detected with standard detectors and ADC's. Stretch processing is an approach where the LFM LO offset is controlled primarily through signal delay with the simplest case (considered here) having no offset frequency and the beat frequency going to DC when the LO and Transmit are perfectly path matched. The beat frequency due to signal delay is shown in in Figure 15.

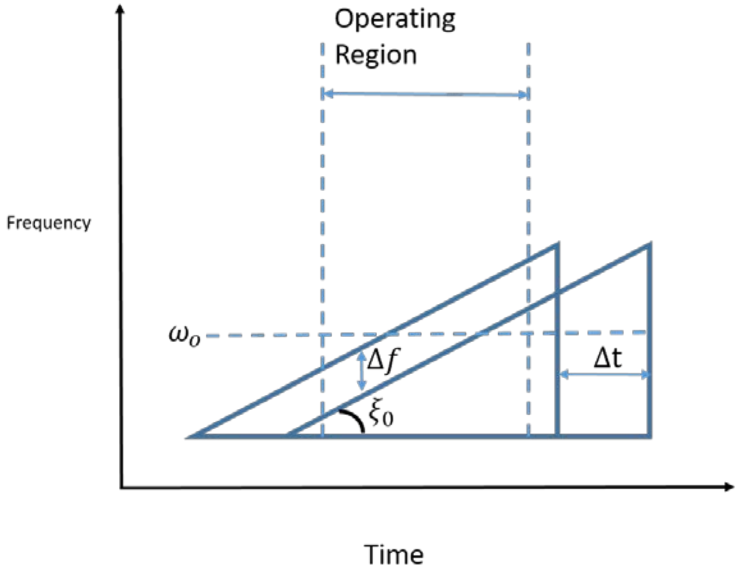

Figure 15: Mixing of Chirp signals for stretch processing. Center frequency is ω_o, frequency difference is Δf. The chirp rate is the tangent of ξ_0 and the delay between chirps is Δt. Within their region of temporal overlap a constant beat frequency occurs which is proportional to the delay of one chirp with respect to the reference.

The differences in scatterer positions in the target will lead to small differences in the expected delay of the return waveform. When the return waveform mixes with the local oscillator, the detected beat frequency will be a function of scatterer range separation from scene center and therefore Fourier processing of the signal will lead to a range profile. The coherent nature of stretch processing also allows recovery of the phase of the beat signal. This technique has the twofold capability of generating a high range-resolution image, with sensitivity to changes in phase. What follows is a brief description of coherent mixing of an LFM waveform on a detector which will show how the range and phase information may be tracked.

Real signals are measurements of intensity on a photosensitive detector such as a singular pixel on a focal plane array camera. The detected power comes from a photocurrent generated on the detector, which is proportional to the modulus squared of the sum of the local oscillator and the return signal fields.

$$I_{det} \propto \left| E_{sig} + E_{LO} \right|^2 = \left(E_{sig} + E_{LO} \right) * \left(E_{sig}^* + E_{LO}^* \right), \tag{49}$$

where E_{sig} and E_{LO} are the electric fields of the return signal and local oscillator respectively. The local oscillator field in a finite rectangle bounded chirped pulse of length T is

$$E_{LO} = A_{LO} \mathrm{rect}\left(\frac{\mathrm{t}}{T} \right) \exp\left\{ j\left[\left(\theta_0 - IF \right) t + \xi t^2 + \psi_0 \right] \right\}, \tag{50}$$

where A_{LO} is the wave amplitude, the intermediate frequency, IF, is the AOM offset frequency, ξ is the chirp rate and ψ_0 as a constant phase offset, which is a consequence of delaying the LO leg and will be unknown. In temporal homodyne detection, the return signal is simply a time-delayed echo of this signal without a center frequency offset:

$$E_{sig} = A_{sig}\mathrm{rect}\left(\frac{\mathrm{t}-\mathrm{t}_s}{\mathrm{T}}\right)\exp\ \left\{ j\left[\theta_0\left(t-t_s\right)+\xi(t-t_s)^2\right]\right\}, \tag{51}$$

where t_s represents the time delay of a scatterer. For brevity, Eq.(51) considers only a single scatterer with time delay t_s. In the case of multiple scatterers, t_s is replaced by the sum of all scatterers interrogated by the detector. The detected single scatterer signal is a photocurrent

$$I_{det} = E_{sig}E_{sig}^* + E_{LO}E_{LO}^* + E_{sig}E_{LO}^* + E_{LO}E_{sig}^*\ . \tag{52}$$

Inserting Eq. (50) and (51) into (52), will make for a fairly large equation. For clarity, each substituted term of Eq. (52) is expressed separately as

$$E_{sig}E_{sig}^* = \ rect\left(\frac{t}{T}\right)rect\left(\frac{t-t_s}{T}\right)\{A_{Sig}^*A_{sig}\exp\{j[\ (\theta_0(t-t_s)+\xi(t-t_s)^2)]]\} \\ \cdot\exp\{-j[(\theta_0(t-t_s)+\xi(t-t_s)^2]]\} \tag{52.2}$$

$$E_{LO}E_{LO}^* = \ rect\left(\frac{t}{T}\right)rect\left(\frac{t-t_s}{T}\right)A_{LO}^*A_{LO}\exp\{\mathrm{j}[(\theta_0-IF)t+\xi t^2+\psi_0]\} \\ \cdot\ \exp\{-j[(\theta_0-IF)t+\xi t^2+\psi_0]\} \tag{52.3}$$

$$E_{sig}E_{LO}^* = \ rect\left(\frac{t}{T}\right)rect\left(\frac{t-t_s}{T}\right)A_{LO}^*A_{sig}\exp\ \{-\mathrm{j}\ [(\theta_0-IF)+\xi t^2 \\ +\psi_0]\}\ \cdot\exp\{j[\theta_0(t-t_s)+\xi(t-t_s)^2]\} \tag{52.4}$$

$$E_{LO}E_{sig}^* = rect\left(\frac{t}{T}\right)rect\left(\frac{t-t_s}{T}\right)A_{LO}A_{sig}^*\exp\{\mathrm{j}\ [(\theta_0-IF)t+\xi t^2+\psi_0]\} \\ \cdot\ \exp\{-j[\theta_0(t-t_s)+\xi(t-t_s)^2]\}\} \tag{52.5}$$

After combining like terms and rearranging, the phase terms in the two DC components, $A_{Sig}^{*}A_{sig}$ and $A_{LO}^{*}A_{LO}$ cancel and only the cross terms remain as components with multiplicative phase as

$$\begin{aligned} I_{det}(t) = rect\left(\frac{t}{T}\right) rect\left(\frac{t-t_s}{T}\right) \Big\{ & A_{sig}A_{sig}^{*} + A_{LO}A_{LO}^{*} \\ & + A_{sig}A_{LO}^{*} exp\left[j\left(IFt - \theta_0 t + \xi t_s^2 - 2\xi t_s t - \psi_o \right)\right] \\ & + A_{LO}A_{sig}^{*} exp\left[j\left(\theta_0 t_s - IFt - \xi t_s^2 + 2\xi t_s t + \psi_o \right)\right] \Big\}. \end{aligned} \tag{53}$$

Examining Eq.(53), the first two terms are simply DC and can be filtered out of the signal. The phase in the third and fourth terms above shows six individual terms. Of the first three terms of the phase, $\theta_0 t_s$ and ξt_s^2 are constants, and *IFt* is only applicable to heterodyne systems. The signal of interest for a homodyne detection system contains the fourth phase term, $2\xi t_s t$ and is

$$I_{mix}(t) = rect\left(\frac{t}{T}\right) rect\left(\frac{t-t_s}{T}\right) \left\{ A_{LO}A_{sig}^{*} exp\left[j\left(2\xi t_s t + \psi_o\right)\right] + A_{sig}A_{LO}^{*} exp\left[-j\left(2\xi t_s t + \psi_o\right)\right]\right\} . \tag{54}$$

The frequency of this signal depends on the chirp rate and the temporal delay between the reflected and reference waveforms. For many scatterers, the composite signal is simply the superposition of the mixed signal due to the delay from each scatterer following

$$I_{\Sigma}(t) = \sum_{t_s} rect\left(\frac{t}{T}\right) rect\left(\frac{t-t_s}{T}\right) \left\{ A_{LO}A_{sig}^{*} exp\left[j\left(2\xi t_s t + \psi_o\right)\right] + A_{sig}A_{LO}^{*} exp\left[-j\left(2\xi t_s t + \psi_o\right)\right]\right\}. \tag{55}$$

The analytic form of this signal is given as

$$I_A(t) = I_\Sigma(t) + jH\left[I_\Sigma(t)\right]. \tag{56}$$

where $H[I_\Sigma(t)]$ is the composite signal Hilbert transform. Taking the Fourier transform of Eq. (55) will yield peaks in frequency space corresponding to the time delays t_s which are the scatterer ranges from center. Figure 16 shows signals from three separate scatterers, their combined detected signal, and the corresponding range profile obtained by taking the Fourier transform of its analytic signal.

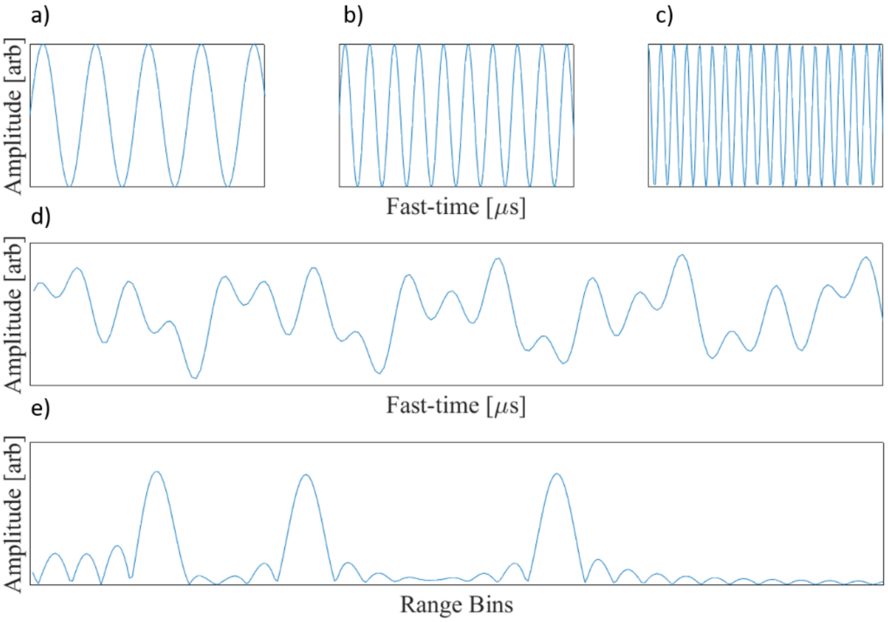

Figure 16: The recovered range returns from three separate scatterers. The matched filter detected beat frequencies associated with time delays t_1-t_3 are (a)-(c) respectively. The analytic signal detected from all three is d). The analytic signal Fourier transform is e), with bandwidth dependent resolution and sample number dependent total range bins.

For discretely sampled signals, the Shannon-Nyquist Criterion requires that twice as many samples must be taken for the supported number of resolvable frequencies. [1] Following this, the range window is

$$R_w = \frac{\Delta z_p \cdot N_{FT}}{2} = \frac{c \cdot N_{FT}}{4BW}. \tag{57}$$

where Δz_p is the range resolution of Eq. (5),and N_{FT} is the number of fast-time samples. From Eq. (54), the chirp rate ξ and pulse duration T will determine the usable bandwidth. The range window is important when designing an imaging system, and determines the maximum depth of a scene. All targets must be within this window, otherwise the resulting mixing between the LO and the range returns will be too high frequency for the detectors resolution and range returns outside the window will not be detected. The Stop-and-Hop model for ISAL requires a trade-off between desired range resolution, range window, and slow-time sample number. Details surrounding this are left for Chapter 8. The next section elaborates further in how the return signal of Eq. (54) relates to the Stop-and-Hop model.

2.11 Slow-time signal processing

The range profiles generated through Eq. (54) represent the fast-time return from a single LFM pulse. For ISAL applications, each fast-time signal record ref from subsequent pulses form the slow-time record in the 2 dimensional phase history. These slow-time samples may be treated as a separate temporal coordinate in the signal. Therefore, the signal collected over the entire CPI may be represented as a concatenation of several fast-time only signals attributed to their corresponding pulses, or

$$I_{PHD}(nT_{FT}, mT_{ST}) = I_{mix}(t)\big|_{t=nT_{FT}+mT_{ST}} = I_{mix}(nT_{FT}+mT_{ST}) \quad \in \begin{cases} n = 1 : N_{FT} \\ m = 1 : N_{ST} \end{cases}, \tag{58}$$

where N_p is the number of chirps in the CPI, τ is the slow-time temporal coordinate, t_τ is the fast-time coordinate for its corresponding pulse, T_{FT} is the fast-time sample duration and T_{ST} is the slow-time sample duration, which is equivalent to the chirp pulse duration *T*. In this way, $I_{PHD}(t)$ can be represented in these two temporal dimensions, such that the final detected signal over many pulses is obtained by substituting Eq. (54) into Eq. (58),

$$s_{PHD}\left(nT_{FT}, mT_{ST}\right) = rect\left(\frac{nT_{FT}+mT_{ST}}{T}\right) rect\left(\frac{(nT_{FT}+mT_{ST})-t_s}{T}\right) \times \left\{A_{LO}A_{sig}^{*} exp\left\{j\left[2\xi t_s(nT_{FT}+mT_{ST})+\psi_o\right]\right\}\right\} \in \begin{cases} n=1:N_{FT} \\ m=1:N_{ST} \end{cases}. \tag{59}$$

Physically, this means that between subsequent LFM pulses, as scatterers move due to target rotation, the phase in the detected signal will migrate over slow-time. Strictly speaking, the scatterers will also migrate during over fast-time, but this motion is so slight that its contributions are negligible in the signal. The range profile per slow-time sample, as per Figure 16 is recovered from taking the Fourier transform of the analytic signal recovered from the fast-time contributions of Eq. (59) and the phase of a scatterer is recovered across slow-time by taking the angle of a peak of the analytic signal Fourier transform following

$$\angle\Psi = \tan^{-1}\left[\frac{\Im\left\{F[s_{PHD}+jH[s_{PHD}])]\right\}}{\Re\left\{F[s_{PHD}+jH(s_{PHD})]\right\}}\right], \tag{60}$$

where $\Im$ and $\Re$ are the real and imaginary parts respectively, F is the one-dimensional Fourier transform with respect to time and H is the Hilbert transform.

2.12 Summary and Direction

All that remains is properly registering the noise corrupted 4D dataset into a larger 3D dataset for improved image formation. The remainder of this dissertation tackles the problem of complex volume registration for noisy, low support data sets of varying sub-aperture separation. It is important first to understand the limitations of the necessary algorithms before any possible improvements can be made to them for better imaging performance. To that end, the next step is to evaluate the performance of two registration algorithms and introduce a new improvement to the cross-correlation algorithm before synthesizing the aperture fields and reconstructing images.

CHAPTER 3

MUTUAL INFORMATION REGISTRATION ALGORITHMS FOR ISAL

The ISAL signal of interest from Chapters 2 is a complex valued data volume composed of a range compressed propagated speckle field separated in to slow-time components. Aperture synthesis requires re-assembly along slow-time of this data volume following Figure 9 and to accomplish this, specialized registration algorithms are required. One viable algorithm derived from information theory is the maximization of mutual information (MI) [13] between data sets. This approach has rich history in registering medical images such as MRI or CT data volumes [14] [15]. More recently, it has been used in LiDAR mapping and point cloud registration [16] and is known for its robustness to noise [17] and applicability to many data and image transformation functions. This chapter introduces the relevant theory for applying mutual information to complex multi-dimensional channels such as those in multi-pixel ISAL. The transformation function for maximizing mutual information is defined with respect to the ISAL target motion introduced before. The effects of noise in the mutual information registration algorithm (MIRA) enumerated function space are shown. Viable MI optimization algorithms for cross-range and phase registration are introduced along with appropriate convergence metrics for these algorithms in the case of ISAL image reconstruction.

3.1 Mutual Information Background

One of the foundations of information theory was the discovery that information content of a data set could be expressed identically to the thermodynamic entropy of a system, or

$$H\left(g_1\right) = -\sum_{\zeta_i} p\left(\zeta_i\right) \log p\left(\zeta_i\right), \tag{61}$$

where $\boldsymbol{g_1}$ is some discrete dataset, such as a 3D volume from Eq. (52), and $p(\zeta_i)$ is the probability mass function (PMF) of a system state ζ_i. Entropy is usually measured in bits and highly complex systems with more overall information content, will have more total entropy. Mutual information between two related datasets is defined as

$$I\left(g_1, g_2\right) = H\left(g_1\right) + H\left(g_2\right) - H\left(g_1, g_2\right), \tag{62}$$

where $H(g_1,g_2)$ is the joint entropy between data sets defined as

$$H\left(g_1, g_2\right) = -\sum_{\zeta_i, \eta_i} p\left(\zeta_i, \eta_i\right) \log p\left(\zeta_i, \eta_i\right), \tag{63}$$

where $\boldsymbol{p(\zeta_i, \eta_i)}$ is the joint PMF between the data sets. For two related data sets, this may be visualized following Figure 17

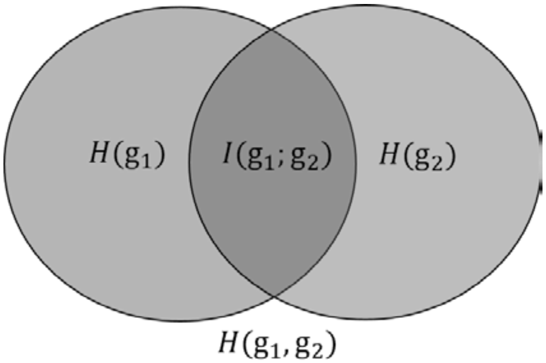

Figure 17: Entropy Venn Diagram.

The relationship between entropy, joint entropy and mutual information of two datasets, or images g_1 and g_2

The PMFs may be modeled as a histogram where the bin number is a free parameter. The joint PMF may be thought of as a 2D histogram, whose first row and first column are the respective 1D PMF histograms. The 2D joint PMF itself may be thought of as a co-occurance histogram, where the sorted values of related datasets are counted for every index where they co-occur. In this way, unrelated images will have a joint PMF distribution matching the distribution shape of either random variable, highly related images will have a joint PMF that looks closer to a diagonal line for their data value co-occurrence, and identical datasets will manifest as a straight line in the joint PMF such as in Figure 18

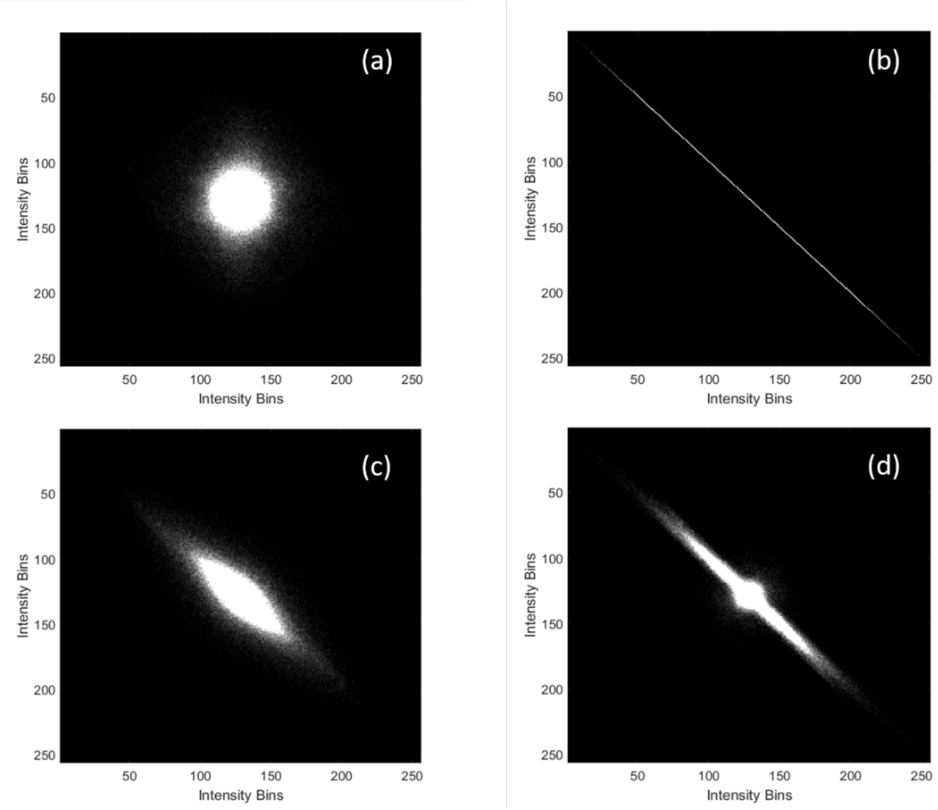

Figure 18: Joint Probability Histograms for different image pairs. Two unrelated images have the joint PMF in a), while two identical images have the PMF in b). Two separate images with overlapping content which are nearly registered have a PMF shown in c), with d) showing full registration.

From Figure 18, images with common information content, once registered, will maximize the count of content co-occurrence and the joint PMF will more closely (but not perfectly) resemble a straight line. Mutual information is typically measured in bits, but a normalized variant, robust to noise [14] is

$$\tilde{I}\left(g_1, g_2\right) = \frac{H\left(g_1\right) + H\left(g_2\right)}{H\left(g_1, g_2\right)}, \tag{64}$$

which is the version this research focusses on.

3.2 Application to Registering Complex Volumes with Noise

MIRA is more typically used in intensity imaging and registration [14] but may be applied to complex data volumes as well. The total information available in the complex data volume is simply the sum of the information in the volume real and imaginary channels [18]and therefore the MI between complex datasets is

$$I\left(g_1, g_2\right) = I\left(g_{1r}, g_{2r}\right) + I(g_{1i}, \mathrm{g}_{2i}), \tag{65}$$

where g_{1r} and g_{1i} are the real and imaginary parts, and the MI for each channel is calculated using Eq. (64). For a real and imaginary channel signal, the total MI may then be visualized following Figure 19

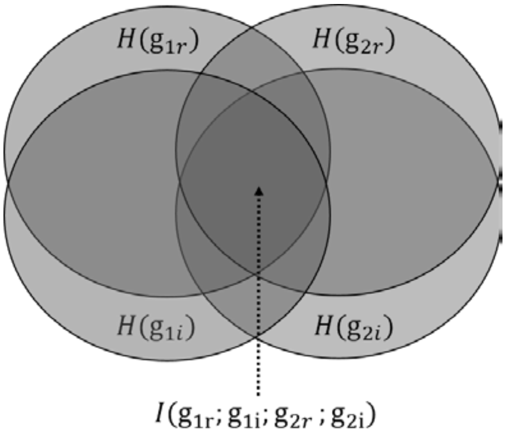

Figure 19: Entropy Venn Diagram.

In this case the entropy is for real and imaginary components of slow-time adjacent image g_{1r} and g_{1i} .

The information content of a dataset will also affect MI registration. A target of interest may have a combination of sparsity and non-sparsity in range and cross-range sampling. An example of such a target is a backhoe viewed from different angles, such as in Figure 20.

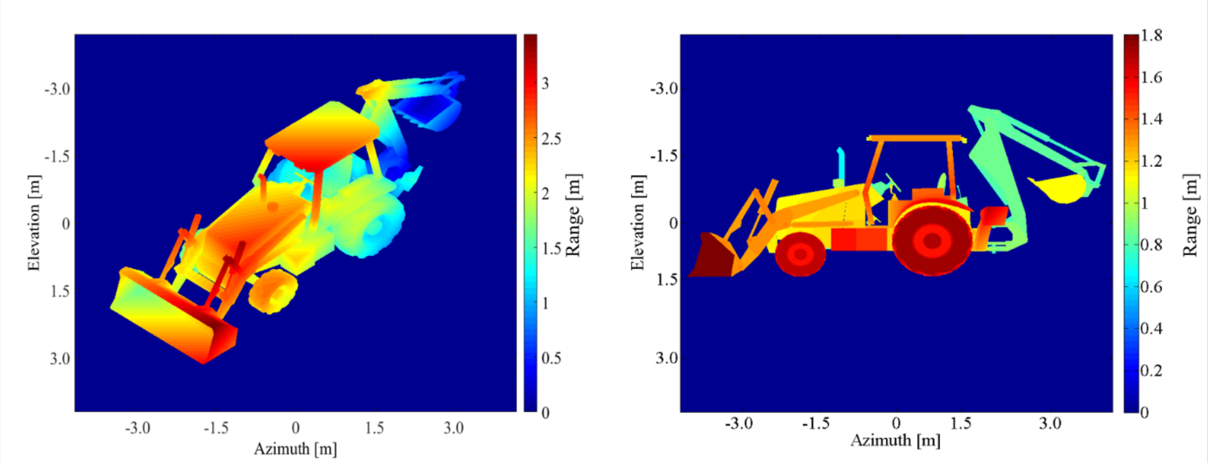

Figure 20: Entropy Comparison between view angles: The range depth and profile of a backhoe target viewed at an odd angle is significantly different than the same target viewed broadside. The entropy in a) is 1.045 bits and 0.9207 bits in b)

Viewed "broadside", this target has more sparsity in range and cross-range. To a detector it looks more like a collection of flat plates. Viewed at an arbitrary angle it has a more complicated structure, which is reflected in calculating the entropy of its reflected field at an interrogating aperture. Later chapters will demonstrate that the information content of a target will affect registration of its reflected field. The data volumes to be registered will be generated from the detected fields from a rotating target. Consider two such fields at the aperture, the reference field $g_1\ (x_a, y_a; z_a)$ and the test field $g_2\ (x_a, y_a; z_a)$ that are measured at adjacent slow-time samples. Both fields must propagate from the target to the aperture in the same way, so the only difference between them will be in the terms related to rotation. Following the field mapping from the target to the aperture plane for an arbitrary rotation from Eq. (34)The relationship between two different fields reflected from a rotating target is shown in Eq (66),

$$g_1(x_a, y_a; z_p) = g_2\left(x_a - 2\alpha(z_p + z_0), y_a - 2\beta(z_p + z_0); z_p\right)\exp[-jk(-2z_p(\beta - \alpha)], \qquad (66)$$

Where the target has undergone azimuth and elevation rotation of α and β respectively. The first term shows the shift between the subsequent aperture field in cross range, and the exponential shows the piston phase difference between the aperture fields. As a two dimensional example, these fields will be speckle patterns at the aperture such those shown in Figure 21

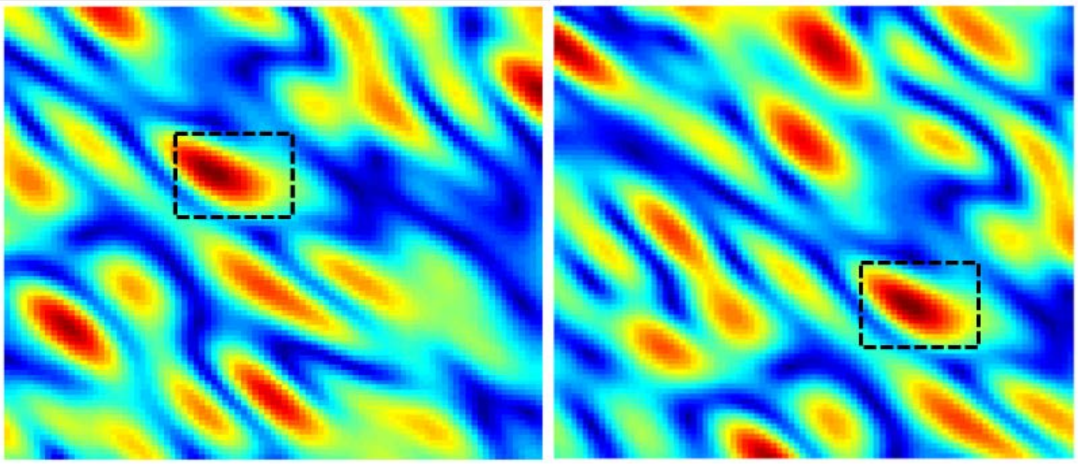

Figure 21: two separate samples of a shifting aperture field. A dashed box is added to emphasize a similar feature. By searching many possible re-translations, the image is registered back into place when MI is at a maximum. This may be applied to translations or rotations in amplitude or phase space or both.

To maximize MI, a transformation function is found that satisfies

$$T = \arg\max_{T} \tilde{I}\left[g_1\left(x_a, y_a, z_p\right), g_2\left(T\left(x_a, y_a, z_p\right)\right)\right]. \qquad (67)$$

For the case of fields emanating from a rotating target, this function will takes the form of a cross-range shift and piston phase exponential, such that the field is transformed following

$$\mathrm{g}_2\left(T\left(x_a, y_a; z_p\right)\right) = F^{-1}\left\{G_2(x_a, y_a; z_p)\right\}\exp\left\{jk\left[z_p + z_0\right](x_a a - y_a b)\right\}\exp\left[2jkz_p(a + b)\right] \tag{68}$$

where $G_2(x_a, y_a; z_p)$ is the Fourier transform of the aperture field $\mathrm{g}_2(x_a, y_a; z_p)$. The first term utilizes the Fourier shift theorem to shift the aperture field in cross-range by applying phase tilts and the second exponential is the piston phase for different range bins induced by target rotation with α and β as free parameters. This can be considered a 3D transformation between apertures where the shifts in cross-range take on two spatial dimensions and the third dimension is the piston phase between subsequent slow-time samples.

Registration through maximization of MI will not directly output the registration parameters of the slow-time pupils. The MI function space must be thoroughly searched for the working transformation function and the accuracy of this search is affected by noise in the signal which corrupts the MI function space. The simplest search method is a brute force enumeration of the function space. In this way, the test field is transformed over a large space and the calculated MI is collected and will show a peak at the corresponding function space coordinates that registers it to the reference image. An example with additive noise, showing a transition between registerable and non-registerable pupil fields is shown in Figure 22

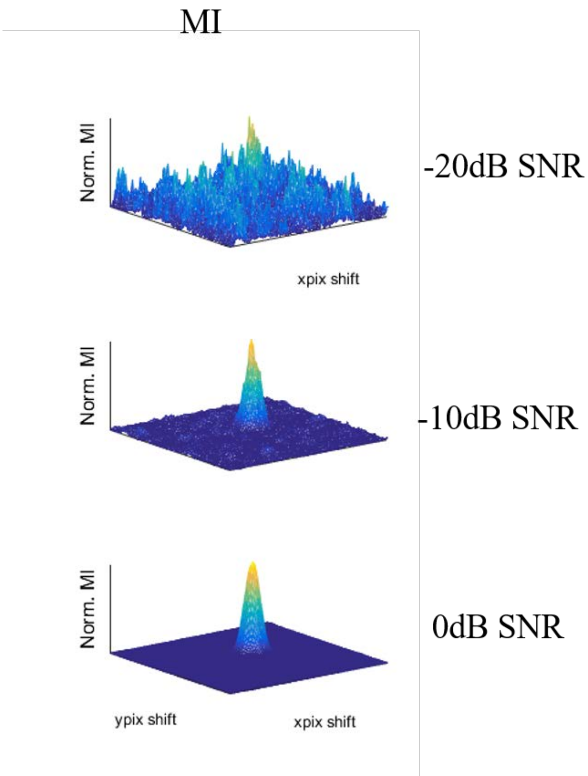

Figure 22: MI peak embedded in varying noise. Following the SNR convention of Eq. (36), the MI function space was enumerated to show a precise peak location at 0dB, an imprecise, but resolvable peak at -10dB and a peak barely above the noise floor, not consistently unrecoverable at -20dB.

As an example from the figure, when the total volumetric SNR of a volume is at -20dB, there is no discernable peak and registration will not function. At -10dB the peak is visible but its location may not be consistent, leading to higher variance in the registration function. At 0dB, the peak is clearly visible and sharp, which allows for consistent registration. An enumeration of the whole function space can be computationally exhaustive, especially in the case of high precision where convergence is desired to a small fraction of a pixel. There are many possible search functions for converging on minima and maxima. The nature of the complex PHD will help in determining the best possible algorithm. Some search functions used in tandem with MIRA are the Nelder-Mead or Downhill Simplex method, the method of Gradient Descent and the Simulated Annealing method. Stochastic Gradient Descent has been used in different MIRA contexts [13], but calculating the derivative is complicated and can be problematic in the case of noise. The cross-range MI is mostly smooth within the realm of the peak, with some but not many local maxima. Conversely, MI calculated in the piston phase space has many local maxima. The Nelder-Mead (NM) method is a quick and easily implemented optimizer with strong support in MATLAB that only requires continuous evaluation of the MI and has no need of calculating derivatives. For these reasons, the NM method was chosen as a viable approach for cross-range registration. The simulated annealing method also does not require knowledge of the derivative, and is an adaptation from Metropolis-Hastings Monte Carlo method, which would works well in the case of noise and is not as vulnerable to local maxima. It is slower than NM, but this is somewhat mitigated when searching over only a 1D function space, and this is why it was chosen to optimize the piston phase of subsequent aperture fields. In general, the optimization approach follows a process outlined in Figure 23

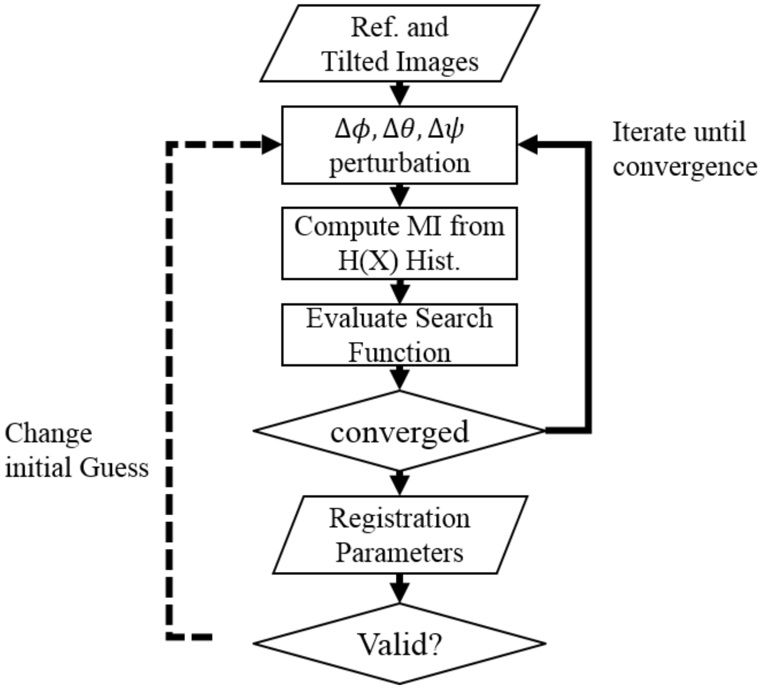

Figure 23: Transformation Search Algorithm. The perturbations shown in this case take the form of phase tilt $\Delta\phi$, tip $\Delta\theta$ and piston $\Delta\psi$. The conditions of convergence can be changed as well depending on time and consistency desired for algorithm convergence.

The search algorithm from the figure begins with the reference and test complex 3D volumes as inputs. An initial guess is made of the cross-range and piston phase transformation of the test volume and the resulting MI between the transformed test and original reference volumes is made, this process is repeated under the NM method for cross-range and the Simulated Annealing method, with the NM converging first. After convergence the registration parameters are output and if considered valid according to expected output constraints, the registration parameters are kept, otherwise the initial guess is changed.

3.3 Numerical Methods for 3D volume MI calculation

Mutual information is calculated through histograms of the real and imaginary channeled amplitude values of the measured field. The entropy is always calculated from a one dimensional histogram of sorted amplitudes, and the joint entropy is always calculated from a two dimensional histogram of co-occurrence of the sorted amplitudes. As such, it does not matter what dimensionality the data structures take, they could be a single series of values or a multi-dimensional array. Similarly it does not matter how the histograms are generated, so long as they are from sorted amplitudes and their co-occurrences. A fast and powerful approach to calculating MI between 3D data volumes is by utilizing the “accumarray” function in MATLAB or a similar approach in other data analysis suites. This function, quickly accumulates all values of a multidimensional array and bins them according to free-parameter inputs. Effectively this is the same as generating a histogram, and allows for the quick MI calculation of related data volumes necessary for a noise and rotation rate sensitivity analysis of interest in this dissertation.

CHAPTER 4

BASELINE CROSS-CORRELATION AND CONVERGENCE METRICS

This chapter introduces the algorithm used as a basis of comparison between MIRA or other cross-correlation enhancements. Image registration through cross-correlation (CC), has become a standard in the aperture synthesis community [10]. These algorithms are an accurate and efficient means of subpixel complex image registration [19]. Effectively applying a registration technique intended for complex 2D arrays to complex 3D volumes requires a minor change that is applicable for long range ISAL imaging. The chapter concludes with the convergence metrics used for direct comparison of MIRA with baseline CC registration, and a brief note on natural advantages and disadvantages of either algorithm, regardless of their sensitivities.

4.1 Volumetric Cross-Correlation Registration for ISAL

For ISAL, the recovered aperture volumes will shift voxels in cross-range bins between collections, but are not expected to shift in range bins. The goal of volumetric registration in this case is to measure the 2D cross-range shift, and piston phase differential between successive data volumes. This is done on range-bin by range-bin basis through finding the location and phase angle of the peak of the CC function, $\Gamma_{xy}(x_0, y_0; z_p)$, generated through a fast Fourier transform technique following

$$\begin{aligned}\Gamma_{xy}\left(x_0,y_0;z_p\right) &= \sum_{x_a,y_a} g_1\left(x_a,y_a;z_p\right) g_2^*\left(x_a-x_0,y_a-y_0;z_p\right) \\ &= \sum_{k_x,k_y} G_1\left(k_x,k_y;z_p\right) G_2^*\left(k_x,k_y;z_p\right) \exp\left[-j2\pi\left(\frac{k_x x_0}{M}+\frac{k_y y_0}{N}\right)\right],\end{aligned} \tag{69}$$

where the first line of Eq. (69) is the CC of the fields $g_1(\boldsymbol{x},\boldsymbol{y})$ and $g_2(\boldsymbol{x},\boldsymbol{y})$. The second line is the frequency domain implementation of the convolution which is the inverse discrete Fourier transform of the product of the discrete Fourier transforms $\boldsymbol{G_1}(\boldsymbol{k_x},\boldsymbol{k_y})$ and $\boldsymbol{G_2^*}(\boldsymbol{k_x},\boldsymbol{k_y})$. M and N are the cross-range dimensions of the volume. This can be done independently for each range binned aperture field, but the motion assumptions consistent with ISAL at range allow for a more powerful technique to simultaneously characterize a whole data volume with the added benefit of noise averaging.

4.2 Noise Mitigation Via Range Bin Averaging

For a target at range, the aperture field will experience the same shifts for each range bin, z_p, and the 2D CCs of Eq. (69) for the 3D pupil volume will have signal peaks at the same cross-range locations. The noise correlations are uncorrelated with random peak locations. This suggests averaging as an initial noise mitigation approach. By coherently summing the 2D CC functions along the range dimension the average autocorrelation is

$$\bar{\Gamma}_{xy}\left(l_x,l_y\right)=\sum_{z_p}\Gamma_{xy}\left(l_x,l_y;z_p\right). \tag{70}$$

Since the target is typically sparsely distributed, only range bins containing significant energy will contribute to the average. When comparing the CC from a single range bin, or the whole data volume, this approach has the effect of increasing the effective CC SNR proportional to the difference in data volume signal to the single range bin signal.

4.3 Methods for Evaluating Algorithm Performance

Long range LiDAR data has several unique factors that will impact the registration algorithm performance. The data volumes will typically have low signal-to-noise ratios and very low cross range support. In addition, the data will be sparse and have various levels of complexity. Metrics are defined for each of these factors. The main metrics used to characterize algorithm performance are accuracy and precision of the shifts in x, y and z. For example, the accuracy may be defined as either the mean error $\mu(\Delta x_s)$ of a single registration parameter or as the root mean squared error (RMSE) of multiple registration parameters.

$$\begin{gathered}\mu(\Delta x_s) = \frac{1}{\mathrm{N}}\sum_{i=1}^{N}\left|\Delta\hat{x}_i - \Delta x_s\right| \\ RMSE(\Delta x_s, \Delta y_s) = \sqrt{\frac{1}{\mathrm{N}}\sum_{i=1}^{N}\left\{\left|\Delta\hat{x}_i - \Delta x_s\right|^2 + \left|\Delta\hat{y}_i - \Delta y_s\right|^2\right\}}\end{gathered} \tag{71}$$

where $\Delta\hat{x}_i$ is the i$^{\text{th}}$ measurement of the measured x-shift and Δx_s is the true shift. An identical accuracy metric can be imposed on the piston phase, but it ought to be treated separately from the cross-range registration parameters, following

$$RMSE(\Delta\psi) = \sqrt{\frac{1}{\mathrm{N}}\sum_{i=1}^{N}\left|\Delta\hat{\psi}_i - \Delta\psi_s\right|^2}. \tag{72}$$

The precision is defined separately with respect each of the registration parameters and is the variance, $\sigma_{\Delta x}{}^2$, of the measured shifts.

$$\begin{aligned}
\sigma_{\Delta x}{}^2 &= \frac{1}{\mathrm{N}}\sum_{i=1}^{N}\left|\Delta\hat{x}_i - \mu_{\mathrm{x}}\right|^2 \\
\sigma_{\Delta y}{}^2 &= \frac{1}{\mathrm{N}}\sum_{i=1}^{N}\left|\Delta\hat{y}_i - \mu_y\right|^2 , \\
\sigma_{\Delta \psi}{}^2 &= \frac{1}{\mathrm{N}}\sum_{i=1}^{N}\left|\Delta\hat{\psi}_i - \mu_\psi\right|^2 ,
\end{aligned} \tag{73}$$

where $\mu_{x,y,\psi}$ is the average value of the collection of registration parameters. The points where these statistical values begin to deviate from their ideal values indicates registration accuracy or precision failures respectively.

4.4 Effects of Noise and Sub-Aperture Overlap

Since both MIRA and the baseline CC registration algorithm use a version of peak finding to calculate the registration parameters, an initial qualitative examination of the search spaces was conducted. The results for the baseline CC and MIRA approaches were calculated to provide an upper bound in registration performance. As an example, the 2D registrations for 15x15 detector support of fields propagated from a the target shown in Figure 8 are compared for three SNR levels in Figure 24

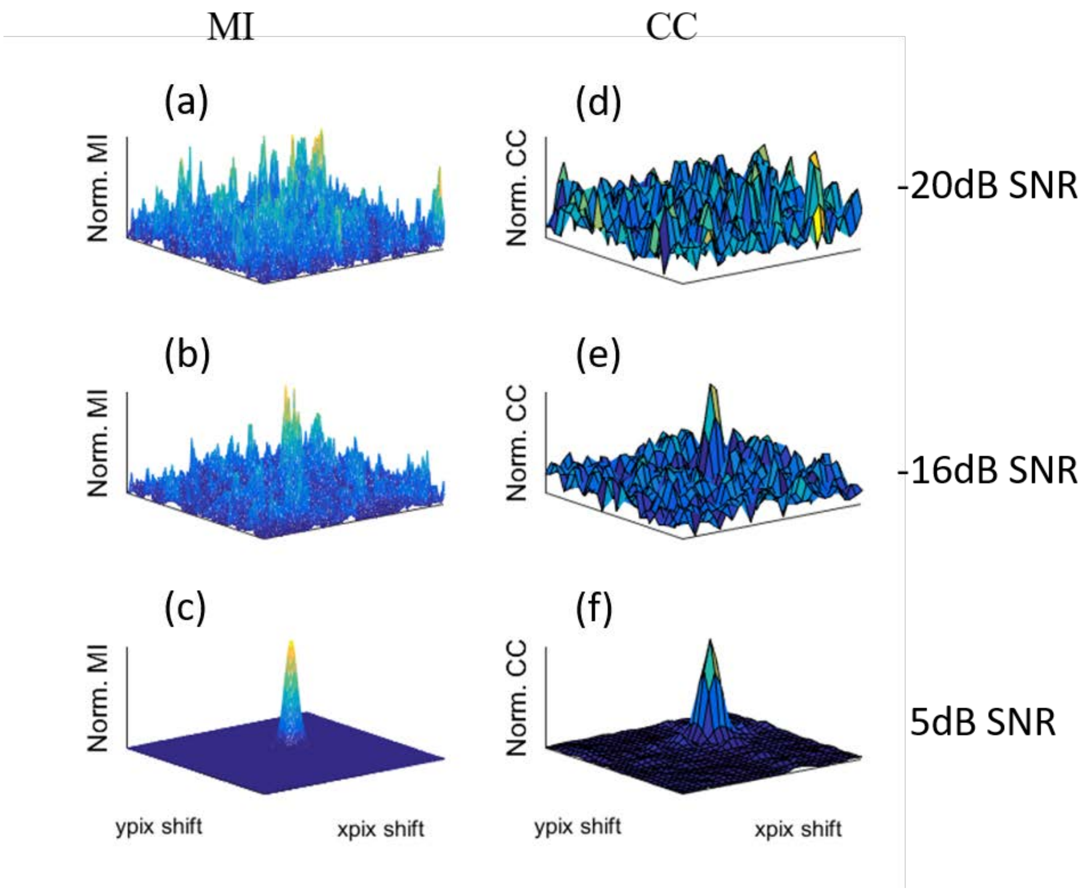

Figure 24: Registration functions for the MI algorithm (a, b, c) and baseline algorithm (d, e, f) for 15x15 detection support at SNRs of -20dB (a, d), -16dB SNR (b, e) and +5dB SNR (c, f).

The baseline CC function space has a detectable peak beginning at an SNR of -16dB (Fig. 24 (e)), while the mutual information function space still is too noisy for reliable registration at that noise level, (Figure 24(b)). Both the MI peaks and baseline CC become reliably detectable at somewhere below 5dB, (Figure 24(f)). The amplitude of the correlation peak will be proportional to the amount of information the two registered volumes have in common, which is affected by overlap of the sub-apertures as well as SNR. In some cases, which will be enumerated in Chapter 7, high SNR volumes may have low capability of registration if their correlation amplitude is sufficiently low due to large shifts between sub-apertures.

4.5 Advantages and Disadvantages

There are different imaging scenarios where either MIRA, single plane CC, or data volume baseline CC ought to be implemented. MIRA has been shown to be effective and noise robust when comparing multi-modal images [17]. It is very slow to converge when compared with an efficient CC algorithm, even when implemented with efficient histogram techniques, so may not be appropriate for certain applications. The baseline CC algorithm analyzed here has the advantage of averaging noise contributions from many range bins of a data volume. It is very noise robust compared to a single range bin CC approach, but operates under the assumption that all range bins are moving equivalently, such that the CC function from each range bin may be coherently summed. In remote ISAL this is an appropriate assumption, but it may not be valid for all image registration scenarios.

CHAPTER 5

MIRA AND BASELINE CROSS-CORRELATION SENSITIVITY ANALYSIS

This chapter details an aperture plane detection complex target ISAL registration sensitivity analysis comparison between MIRA and baseline CC mentioned in chapters 3. The original motivation for such an analysis was an imaging viability comparison between mutual information registration and a more commonly used cross-correlation approach. If MIRA were to outperform the baseline with respect to SNR sensitivity, it would be a viable alternative for some applications. As will be shown, volumetric MIRA and the baseline CC algorithm have comparable registration capability with respect to SNR sensitivity which was a large motivator for pursuing algorithm enhancements to the baseline.

The first section of this chapter details the generation of simulated ISAL PHD from a highly complex and realistic target of interest. The remaining sections show the method of comparison in the form of a sensitivity analysis which iterates over different SNR, rotation rate and imaging support scenarios. The algorithms are compared against standard registration metrics, such as registration variance and error overviewed in the previous chapter. When the algorithms no longer operate over these sensitivity variables, a judgment is made for which registration approach is most appropriate.

5.1 Motivating Imaging Scenario and Sensitivity Considerations

Available CC and Mutual Information registration algorithms motivates a utility comparison for the imaging scenarios discussed previously (long range, low support, varying SNR ISAL). Previous work claims Mutual Information is highly robust to noise, and of high utility in multi-modal imaging [14], and some comparisons between either registration approach for different imaging scenarios has previously been explored [11]. It was expected that one of these algorithms would win out in noise, shift, and support, so an appropriate simulation for assessing the better algorithm for this case was developed.

5.2 Target of Interest

The target of interest has a combination of sparsity in range and cross-range and is highly complex. A commercially available faceted target model for a backhoe was chosen as the target because it includes all these considerations. The target, when viewed from an askew angle, is highly complex and includes superposition of flat plate, angled plates, points and empty spaces, and as a result has relatively high entropy and information content. To vary information content, this target may be viewed from two angles, either the askew angle, with high entropy, or viewed broadsided with comparatively lower overall entropy as shown in Figure 20,

5.3 Simulated Aperture field generation

Once the faceted target was generated in the desired orientation, the next step was to generate simulated phase history data from the target as if it were interrogated by a 1.55 micron ISAL imaging system at range. Such a system is modeled following Eq. (34) with range bin width dependent on signal bandwidth and with range bin phase modulo 2π, which generates a signal following Eq. (59). This signal is then range compressed to create a volumetric PHD representing the target. In applying registration algorithms to ISAL system generated data volumes, it may already by assumed that the data is range-compressed, so that the PHD to be generated comes from propagating a target plane range volume to the aperture plane via Fresnel propagation. From the faceted model shown in Figure 20, the points were treated as delta functions and shifted to appropriated points within an evenly distributed 3D matrix in MATLAB with appropriated wrapped phase following Eq. (18) Uniformly distributed random phase was assigned to each scatterer in the volume to simulated surface roughness and the volumetric field is propagated to the aperture plane following Eq. (26)in the case of a stationary target and Eq. (34) for the rotating target. The result is a finely sampled 3D speckle pattern which retains the full information content of the complex target.

5.4 Support variation and field detection

Once the reflected field on the target has been propagated to the aperture plane, the field must then be sampled by a detector, which is limited by the aperture size and pixel support. For registration algorithm testing and sensitivity analysis purposes, this process was kept relatively simple and a square aperture was used for aperture plane detection instead of image plane detection where the field would first be focused at each pixel.

5.5 Noise inclusion

Noise occurs at detection and is a combination of shot noise and thermal noise, with shot noise considered the limiting source for a well-designed system. Although shot noise is Poisson distributed, the central limit theorem applies for these cases of relatively high photon flux and a Gaussian distribution may be used instead to model the shot noise of the system and account for any additional Gaussian distributed thermal noise. For this simulation the SNR was calculated volumetrically, following Eq. (36) and Eq. (37).

5.6 Simulation Variables

The process mentioned for obtaining aperture space PHD was incorporated into a sensitivity analysis script which varied over the detection parameters of interest (SNR, shift and support) following Figure 25

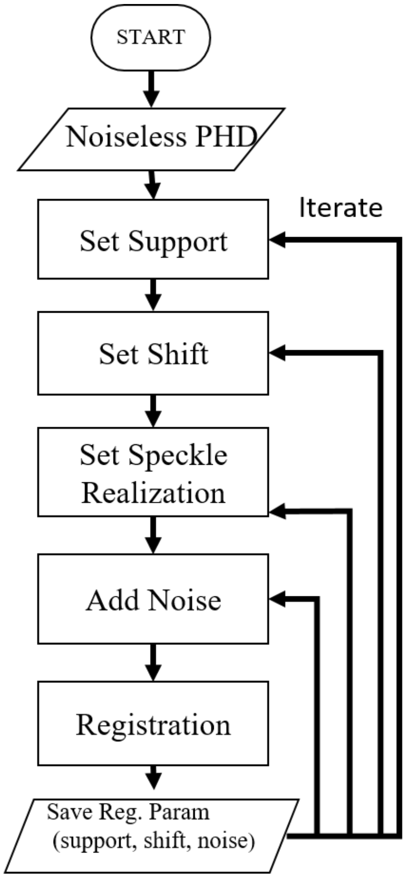

Figure 25: Sensitivity Analysis Flowchart. The script is embedded loops of registrations over difference SNR, sub-aperture shift and support levels for the data volumes.

The sensitivity analysis script was designed to organize the resulting registration parameters obtained from both the MIRA and baseline registration approaches into separate output arrays, where the parameters according their respective shift, SNR and support could be accessed.

5.7 Shift and Phase Sensitivity Results

Following the flowchart, a shift of 1-4 pixels between subsequent aperture planes was iterated over, with differential volumetric SNR ranging from -20dB to +5dB. The baseline algorithm sensitivity plot is shown below in Figure 26

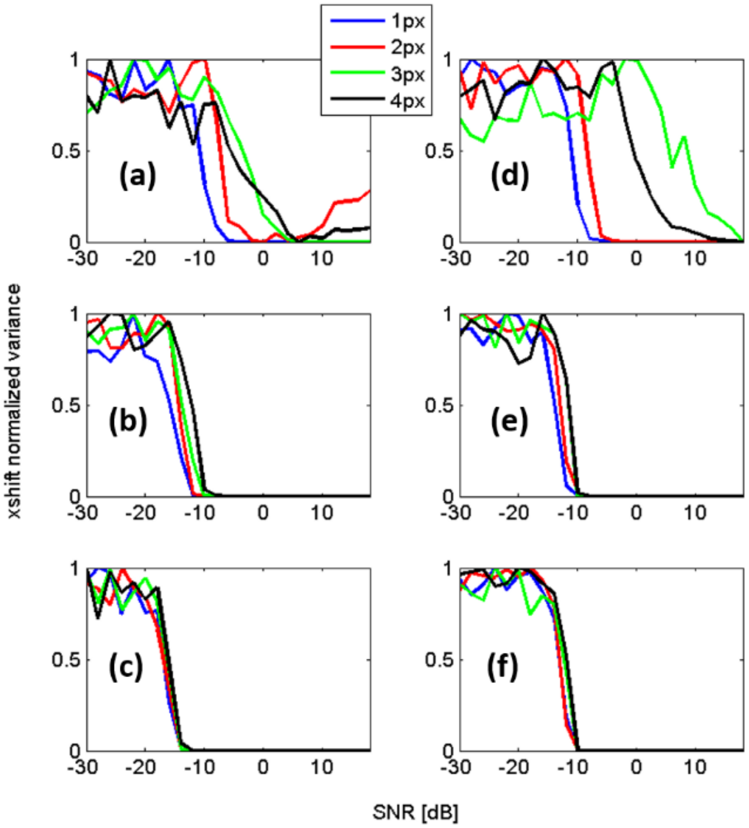

Figure 26: Cross-correlation registration convergence curves for two separate targets. The high entropy askew backhoe target data is shown in (a,b,c) with the lower entropy as (d,e,c). the first row (a,d) is the 5x5 support at the aperture with the next row the 11x11 support and the last row the 15x15 support. Pixel shift within each support level is shown in separate colors, blue red green and black or 1-4 pixels of sub-aperture shift respectively.

Following the subplots in the left column are from the angled backhoe target, and the rightmost subplots are the broadside target. The variance of the registration parameters are plotted against volumetric SNR, with the different colors indicating the number pixel shifts between sub-apertures and the subplot rows indicating the support side-length of the apertures. The figure shows that at a critical SNR, roughly -14dB for the 15x15 support and -10dB for the 11x11 support, the registration breaks down. At lowest support the SNR where the algorithm breaks is more closely dependent on the number of pixels shifted because each pixel shifted represents a larger overall percentage change in aperture overlap than in the higher support cases.

The MIRA approach was given an initial guess 0.25 pixels away from correct location of the registration peak and allowed to search the area for maximum MI. After convergence, the algorithm output the registration parameters that yielded the maximum MI and these values were saved to an array. This whole process was repeated for the same backhoe target interrogated from the broadside angle and algorithm convergence was first measured with respect to registration parameter variance over 100 separate speckle realizations following Eq. (73).

The MIRA corollary to Figure 26 is Figure 27 and shows similar trends but have a different shape following the different overall nature of the registration convergence (search function vs. area registration)

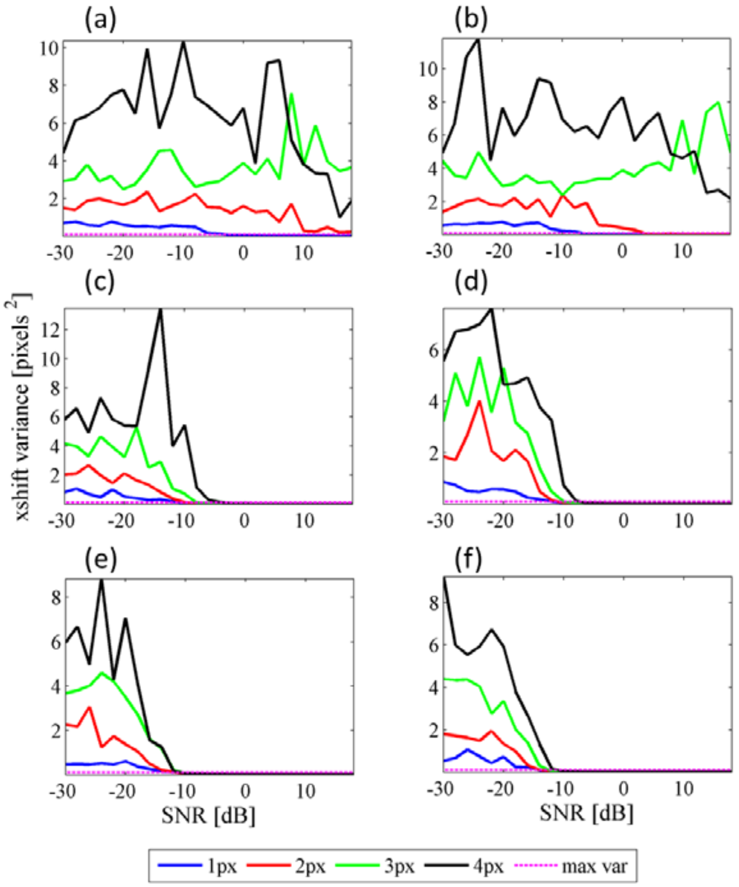

Figure 27: MIRA convergence curves for two separate targets. The high entropy askew backhoe target data is shown in (a,b,c) with the lower entropy as (d,e,c). the first row (a,d) is the 5x5 support at the aperture with the next row the 11x11 support and the last row the 15x15 support. Pixel shift within each support level is shown in separate colors, blue red green and black or 1-4 pixels of sub-aperture shift respectively.

Again the 15x15 support case shows registration convergence for SNR above approximately -12dB. 11x11 support is more varied with convergence with respect to pixel shift and the lowest support of 5x5 shows convergence only for 1 or 2 pixels of shift and at relatively high SNRs.

Registration variance is not the whole story however. It is possible that for large shifts with respect to the size of an aperture induce a bias in the baseline CC registration results, such that the algorithm can consistently converge to the wrong parameter. To properly account for this, registration error in addition to variance was adopted as a convergence metric. An example of this phenomenon is shown in Figure 28

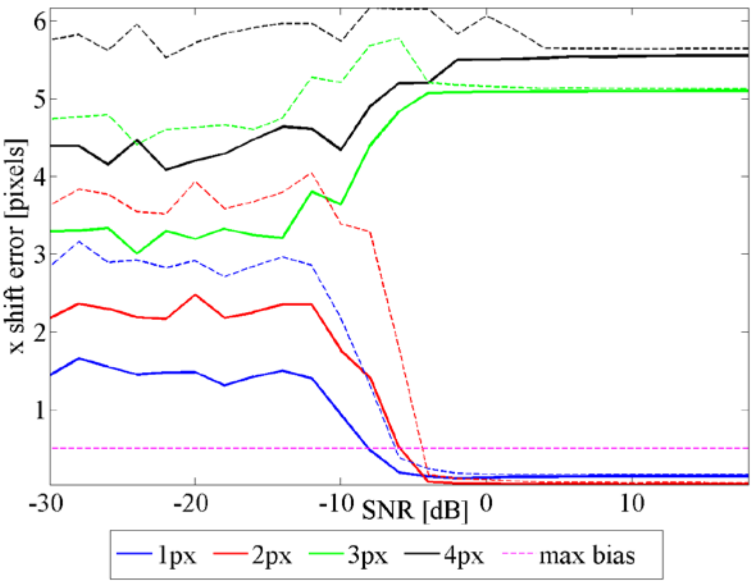

Figure 28: baseline algorithm xshift error for 5x5 aperture support. Solid colors are mean registration error and dashed lines are standard deviation.

As shown in the figure, the dashed lines showing standard deviation converge at high SNR, but to a biased value in for the case of 3pixels and 4 pixels of shift. This would show up as low overall variance. An added dashed line indicating the maximum allowable error in the registration parameters is included in Figure 28 where more than a .5 pixel off the expected registration parameter indicates a failure of correct convergence.

The registration algorithms are designed to simultaneously register in phase along with x-shift and y-shift. A combined case of shift and phase error metrics is shown in Figure 29 with a 1/10 pixel error line indicating the threshold of viable convergence following an aperture synthesis convention of phase errors being less than 10% in error, or 1/10 of a pixel and 1/10 of a wave of phase.

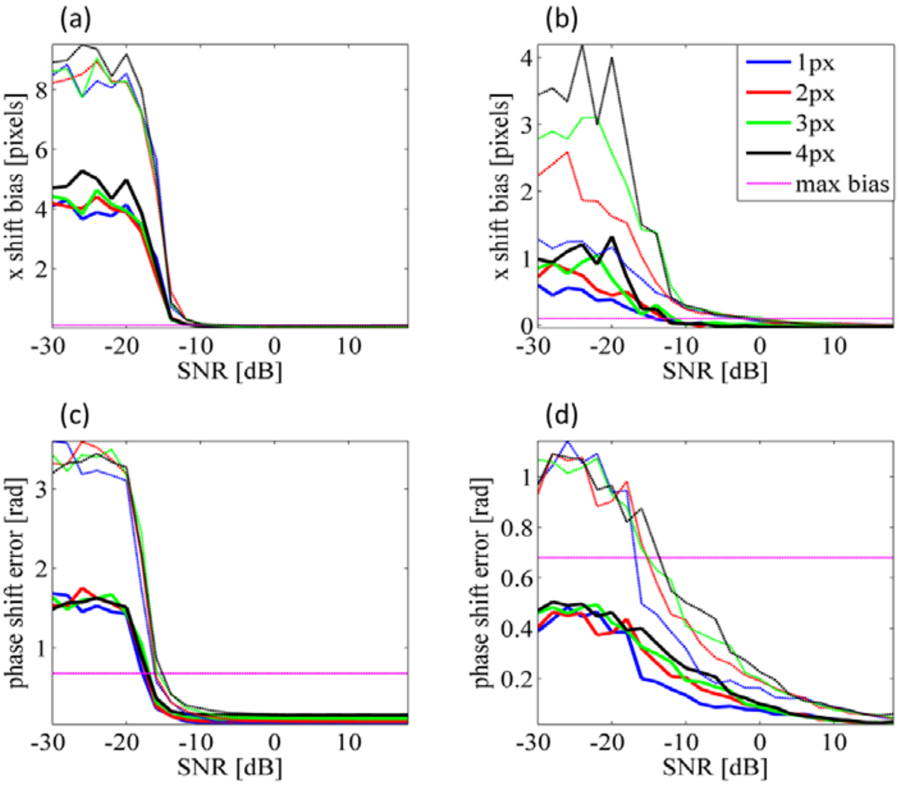

Figure 29: Cross-correlation registration convergence curves for two separate targets.

From above, the shift bias for baseline CC in the high support case crosses 1/10th of a pixel at -12dB, with similar crossing via MIRA registration. For the phase, the baseline CC algorithm crosses viable registration at roughly -15dB SNR, but the MIRA case more ambiguous. Because MIRA was given a guess that was not too far off the correct phase value, and the window of allowable phase registration is relatively large (.68 rad), the mean value of the phase shift error does not exceed the threshold. This does not mean the algorithm has adequately converged. Instead, setting the standard deviation from the mean a convergence metric, it is shown that MIRA converges in phase, for this specific scenario at -13 to -16 dB SNR depending on the amount of pixel shift.

5.8 Discussion

Going into the sensitivity analysis, it was expected that lower support would have a significant, adverse effect on registration convergence, both for the MIRA and baseline approaches. It was expected that a critical SNR, in either algorithm, would yield de-convergence of the registration and that this SNR would be different depending on the algorithm. Similarly, the percentage of overlap between apertures of different levels of support would affect the value of this critical SNR. Zooming in on figure 25 this behavior is shown to occur with baseline CC.

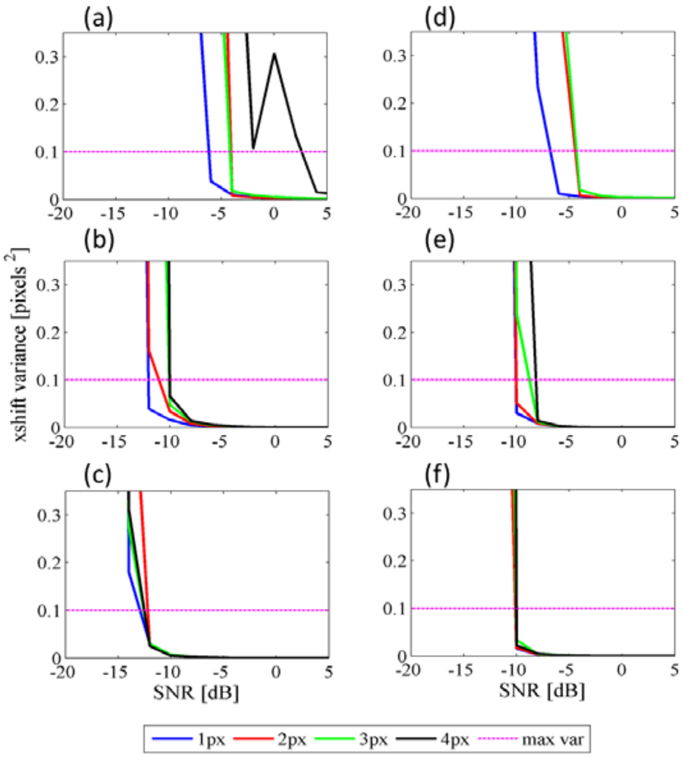

Figure 30: Zoomed in baseline CC registration convergence curves for two separate targets.

The behavior shown in Figure 30 verify these expectations and answer some specifics on the limitations of either algorithm. The figure shows how aperture shift decreases the total correlation amplitude between the sub-apertures and makes registration more sensitivity to noise. This effect is more pronounced for greater percentages of aperture shift. Interestingly, if the percent difference in shift between two separate pixel separations is small, say 1 or 2 pixels of shift in a 15x15 support aperture, the sensitivity with respect to SNR is essentially unaffected. Another important difference seen upon inspection of Figure 30 is how immediate the transition from occurs between registration convergence and de-convergence. Recall from Figure 24 where the function space for MI and baseline CC between two separated apertures was enumerated in different SNR conditions. Because MIRA employs a search function to more efficiently find local maxima in the function space, it is typically chosen with a guess in mind, and the search function is free to converge so somewhere near that guess. This means that the total error of a MIRA registration trial that is not converging may be lower than a baseline CC error. Furthermore, because baseline CC is so quick compared to MIRA, it can sample a larger overall function space and just find the global maximum. In low SNR, the location of that global maximum has essentially become uniformly distributed about the whole function space and when the algorithm breaks, it breaks suddenly and dramatically. Following the mean error metrics for convergence for MIRA and baseline CC, and choosing the 1/10th pixel error tolerance in cross-range and the 1/10th of a wave piston phase tolerance, the performance of either algorithm with respect to SNR, shift and support, for both the complex and simpler targets is summarized in Table 1.

Table 1: Summary of Volume Registration Error Inflection Points for Complex and Simple Targets

Complex Target

	Cross-Correlation			**MIRA**		
Pixel Shift	15x15 Shift/Piston	11x11 Shift/Piston	5x5 Shift/Piston	15x15 Shift/Piston	11x11 Shift/Piston	5x5 Shift/Piston
1px	-13dB/-15dB	-14dB/-14dB	-7dB/-10dB	-12dB/-16dB	-10dB/-13dB	-4dB/2dB
2px	-12dB/-15dB	-13dB/-13dB	-4dB/-8dB	-12dB/-14dB	-9dB/-12dB	20dB/20dB
3px	-12dB/-15dB	-13dB/-12dB	20dB/-7dB	-11dB/-12dB	-8dB/-8dB	20dB/20dB
4px	-12dB/-15dB	-12dB/-12dB	20dB/-4dB	-11dB/-13dB	-4dB/-3dB	20dB/20dB

Simple Target

	Cross-Correlation			**MIRA**		
Pixel Shift	15x15 Shift/Piston	11x11 Shift/Piston	5x5 Shift/Piston	15x15 Shift/Piston	11x11 Shift/Piston	5x5 Shift/Piston
1px	-10dB/-16dB	-10dB/-13dB	-7dB /-10dB	-14dB/-16dB	-12dB /-13dB	-6dB/-6dB
2px	-10dB/-15dB	-10dB/-13dB	-5dB/-9dB	-13dB/-15dB	-11dB/-12dB	4dB/1dB
3px	-10dB/-14dB	-9dB/-12dB	20dB/-5dB	-13dB/-13dB	-10dB/-10dB	20dB/20dB
4px	-10dB/-14dB	-8dB/-12dB	20dB/1dB	-11dB/-13dB	-7dB/-8dB	20dB/20dB

Highlighting in the table shows areas of roughly equal percent shift between sub-apertures, for instance 1 pixel of shift in the 5x5 case is roughly the same percent shift between apertures as 3 pixels in the 15x15 case. It is expected that in such equal cases, the SNR of algorithm convergence should be the same. It is by brief inspection of Table 1 that this is shown not to be the case. Aperture support, by itself, does play a role in total registration convergence for MIRA and baseline CC approaches. Another important point to take from the table is that target complexity has some role as well. A complete and exhaustive study of target complexity was not undertaken as part of this dissertation, but only a simpler study between two similar cases. The only conclusion shown here is that target geometry and/or orientation has some bearing on algorithm robustness, at least for overall low support imaging scenarios. This should be taken into account when calculating minimum SNR required for volumetric registration of an unknown sparse target of low overall support.

The most important piece of info gleaned from this study is the fact that the baseline CC approach proved more accurate and precise over varying noise levels than the mutual information approach in each simulation variant. These results were expected based on Figure 24 where the MI enumerated peaks became visible 4-5 dB above the baseline CC results. The additional deviation in MIRA performance is most probably due to the limitations of the search algorithms used. Implementing a search algorithm for finding the mutual information peak is a much slower and less reliable process than simply computing an upsampled CC function over the entire space and finding the location of the function maximum. While there was still work to be done in optimizing the search algorithm and in computing mutual information, the registration algorithm itself performed about 100 times slower than the comparatively precise baseline CC algorithm.

The similar robustness with respect to SNR, shift and support between baseline CC and MIRA, the complexity introduced to registration through a search algorithm, and computational time differences make MIRA a less desirable registration approach for this imaging scenario. Importantly, baseline CC is only competitive with MIRA when the correlation function is able to be coherently summed across all the range bins, which is a powerful technique, but requires small, rigid body motions typical of hard targets moving at range. The search over the transformation space between reference and test images utilized in MIRA is agnostic to the type of deformation images to be registered. The fact that MIRA works with low support complex valued data means that it may be more viable for different imaging scenarios, but this was not in the scope of this research.

With MIRA appearing less viable than the baseline for this application, the next goal was to explore improvements to CC registration with respect to larger shift and SNR. As demonstrated in Figure 28, biases in the baseline CC registration can occur when the sub-aperture shift is large when compared with total support, and the techniques outlined in Chapter 4 are utilized to perform a sensitivity analysis for this new situation.

CHAPTER 6

ENHANCED 3D CROSS-CORRELATION ALGORITHMS FOR MULTI-PIXEL ISAL

This chapter overviews an ISAL specific baseline CC registration algorithm designed to be robust to noise. It is shown that this algorithm improves registration performance with respect to noise and sub-aperture overlap. This is accomplished through modeling of the noise contributions in the CC function space and accounting for the effects of a circular aperture autocorrelation present in gated data volume CC. The advantages and disadvantages of this approach compared to MIRA are briefly discussed.

6.1 Adaptation for Data Volumes from Slowly Rotating Targets

In this section, the noise component in the CC function will be estimated and removed, and an inverse aperture autocorrelation function will be applied to the new CC estimate to mitigate shift errors. To simplify the notation, the rotation induced shifts x_s and y_s are defined as

$$\begin{aligned} x_s &= 2\alpha(z_p + z_0) \\ y_s &= 2\beta(z_p + z_0), \end{aligned} \tag{74}$$

And substituted into Eq.(34). The un-shifted reference volume $r(x_a, y_a; z_p)$ and shifted $s(x_a, y_a; z_p)$, are

$$\begin{aligned} r\left(x_a, y_a; z_p\right) &= \left(g\left(x_a, y_a; z_p\right) + N_1\left(x_a, y_a; z_p\right)\right) A\left(x_a, y_a; z_p\right) \\ s\left(x_a, y_a; z_p\right) &= \left(g\left(x_a - x_s, y_a - y_s; z_p\right) + N_2\left(x_a, y; z_p\right)\right) A\left(x_a, y_a; z_p\right), \end{aligned} \tag{75}$$

where $g(x_a - x_s, y_a - y_s; z_p)$ is the raw field at the aperture plane which has been shifted by x_s and y_s, $N_1(x_a, y_a; z_p)$ and $N_2(x_a, y_a; z_p)$ are circular random Gaussian noise volumes The CC function of these pupil fields is

$$\Gamma_{rs}\left(l_x,l_y;z_p\right)=\int\int_{-\infty}^{\infty} r\left(x_a,y_a;z_p\right)s^*\left(x_a-l_x,y_a-l_y;z_p\right)dx_a dy_a\,, \tag{76}$$

where l_x and l_y are the shift coordinates in the 2D correlation. Substituting Eq. (75) into (76) and rearranging terms, the CC is

$$\begin{aligned}\Gamma_{rs}\left(l_x,l_y;z_p\right)=&\int_{-\infty}^{-\infty}\int_{-\infty}^{\infty} g\left(x_a,y_a;z_p\right)A\left(x_a,y_a;z_p\right)\\&\times g^*\left(x_a-x_s-l_x,y_a-y_s-l_y;z_p\right)A\left(x_a-l_x,y_a-l_y;z_p\right)dx_a\,dy_a\\&+\int_{-\infty}^{-\infty}\int_{-\infty}^{\infty} N_1\left(x_a,y_a;z_p\right)A\left(x_a,y_a;z_p\right)\\&\times {N_2}^*\left(x_a-l_x,y_a-l_y;z_p\right)A\left(x_a-l_x,y_a-l_y;z_p\right)dx_a\,dy_a\end{aligned} \tag{77}$$

where the first integral term is the CC of the noiseless, aperture limited reference and shifted fields. The second integral term contains the CC of the two aperture limited realizations of the additive noise.

The autocorrelations of Eq. (77) can be written

$$\Gamma_{rs}\left(l_x,l_y;z_p\right)=\Gamma_{r_0s_0}\left(l_x,l_y;z_p\right)+\Gamma_{AN_1AN_2}\left(l_x,l_y;z_p\right), \tag{78}$$

where $\Gamma_{r0s0}(l_x,l_y,z_p)$ is the noiseless autocorrelation and $\Gamma_{AN1,AN2}(l_x,l_y,z_p)$ is the autocorrelation of the aperture limited noise. As shown from Eq.(70), these fields can be coherently summed along the range dimension and the average CC is

$$\begin{aligned}\overline{\Gamma}_{rs}\left(l_x,l_y\right)&=\sum_{z_p}\Gamma_{rs}\left(l_x,l_y;z_p\right)\\&=\sum_{z_p}\Gamma_{r_0s_0}\left(l_x,l_y;z_p\right)+\sum_{z_p}\Gamma_{AN_1AN_2}\left(l_x,l_y;z_p\right).\\&=\overline{\Gamma}\left(l_x,l_y\right)+\overline{\Gamma}_{AN_1AN_2}\left(l_x,l_y\right)\end{aligned} \tag{79}$$

The first summation in the last line of Eq. (79) is the average of the noiseless signal. Since the target is typically sparsely distributed, only range bins containing significant energy will contribute to the average. The second summation is the average of the autocorrelation of the noise which is stationary over all the range bins.

6.2 Noise Autocorrelation Estimation and Subtraction

The peak location of the CC or its modulus will supply the cross-range registration parameter with the piston parameter acquired from the angle of the CC at the location of this peak. It is desired to subtract a real and positive noise estimate from the CC, so these operations are done with respect to CC moduli. The aperture gated signal-only cross correlation modulus follows

$$\left|\overline{\Gamma}_{r_0 s_0}\left(l_x,l_y\right)\right| \le \left|\overline{\Gamma}_{rs}\left(l_x,l_y\right)\right| - \left|\overline{\Gamma}_{AN_1AN_2}\left(l_x,l_y\right)\right|. \tag{80}$$

The noise realization is unknown so the last term above must be estimated. For ergodic noise realizations, CC follows the property:$|\Gamma_{uv}(\tau)| \le [\Gamma_u(0)\Gamma_v(0)]^{1/2}$ where $\Gamma_u(0)$ and $\Gamma_v(0)$ are the zero-lag autocorrelations of the two random variables, which are equivalent to their second moments for ergodic random variables. This follows from application of the Cauchy-Schwarz inequality to complex valued functions that are at least wide sense stationary [20]. Because the additive noise is zero mean, its second moment is its variance, so the modulus of the second term of Eq. (80), may be estimated as

$$\left|\overline{\Gamma}_{AN_1AN_2}(l_x,l_y)\right| \le \sqrt{\sigma_{N_1}{}^2\sigma_{N_2}{}^2\cdot\Gamma_A\left(l_x,l_y\right)}, \tag{81}$$

where Γ_A is the circular aperture function auto-correlation, and $\sigma_{N_1}^2\ \sigma_{N_2}^2$ is the product of the variances of the noise added to either aperture. Equation (80) is then estimated as

$$\left|\overline{\Gamma}_{r_0 s_0}\left(l_x,l_y\right)\right| \leq \left|\overline{\Gamma}_{rs}\left(l_x,l_y\right)\right| - \sigma_{N_1}\sigma_{N_2}\sqrt{\Gamma_A\left(l_x,l_y\right)}\ , \qquad (82)$$

which shows that the effects of aperture noise may be mitigated by subtracting a pedestal shaped by the aperture and weighted by a statistical estimate of the noise within the measurements.

6.3 Correlation Overlap Compensation

This section addresses the center bias due to the reduced aperture autocorrelation peak heights for larger shifts. The CCs and noise estimates have been done with respect to measured fields $r(\mathrm{x_a},\mathrm{y_a};z_p)$ and $s(\mathrm{x_a},\mathrm{y_a};z_p)$ and which have a dependence on an aperture $A(x_a,y_a;z_p)$ An estimate of an aperture independent noiseless CC modulus follows

$$\left|\overline{\Gamma}_{g_r g_s}\left(l_x,l_y\right)\right| = \frac{\left|\overline{\Gamma}_{r_0 s_0}\left(l_x,l_y\right)\right|}{\overline{\Gamma}_A\left(l_x,l_y\right)}. \qquad (83)$$

where an inverse aperture autocorrelation term is applied to the noiseless estimate. The final compensated CC function to be obtained from the complex volumes and aperture function after substituting (82) into (83) is

$$\left|\hat{\overline{\Gamma}}_{g_r g_s}\left(l_x,l_y\right)\right| = \frac{1}{\Gamma_A\left(l_x,l_y\right)}\left(\left|\overline{\Gamma}_{rs}\left(l_x,l_y\right)\right| - \sigma_{N_1}\sigma_{N_2}\sqrt{\Gamma_A\left(l_x,l_y\right)}\right), \qquad (84)$$

The expression above is the estimate of the CC of uncorrupted fields at the aperture plane using the measured cross-correlation $\Gamma_{\mathrm{rs}}(l_x\ ,\ l_y\ )$, the noise statistics, and the known shape of the aperture; referring back to Fig. 3(d), the enhanced CC function with a peak in the correct location is obtained through this approach.

The expression above is the estimate of the CC of raw fields at the aperture plane using the measured cross-correlation $\Gamma_{rs}\left(l_x, l_y; z_p\right)$, the noise statistics, and the known shape of the aperture. For the case of large shifts across slow-time corrupted by Gaussian detector noise, Eq. (84) will statistically favor enhanced CC peaks located further from zero.

This technique has the capability of overcoming the shift biases in baseline CC registration for this imaging application. The mechanism is demonstrated in Figure 31.

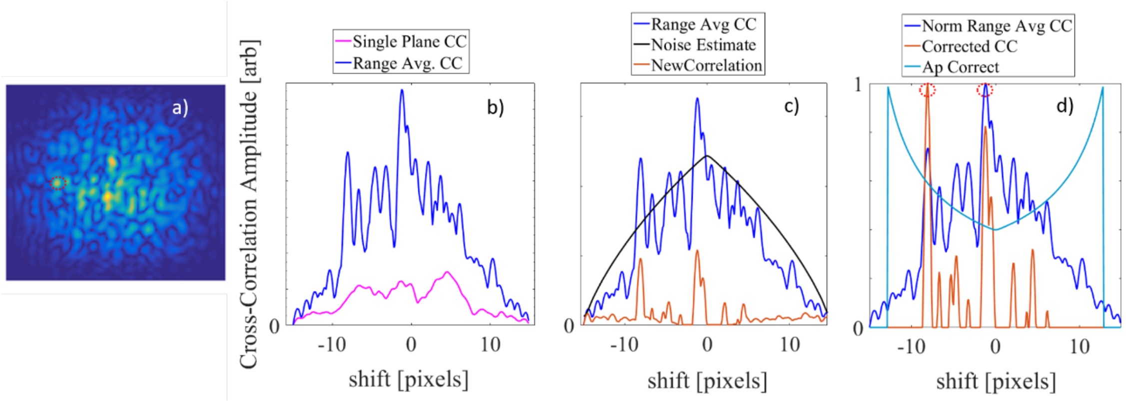

Figure 31 a) Baseline CC function of 3x padded pupil volume, 15 pixels wide, which has undergone an 8.0 pixel shift. Correlation space noise estimation and subtraction in (b). Inverse Aperture function applied to the CC function in (c) to enhance correlation peaks that may reside at the wings. This inverse aperture function is truncated at the edges to prevent false peaks beyond the edges of the aperture due to ringing

In Figure 31 the true 8.0 pixel shift is recovered from the enhanced CC function, while the baseline registration technique, with this level of noise and aperture shift, yields a registration parameter near 0 pixels of shift. The enhanced CC algorithm operates almost identically to the baseline CC, except for some extra noise removal techniques and better performance for sub-apertures that are have significant separations. This is due to the aperture autocorrelation bias compensation approach in the algorithm, and as such, this algorithm is likely to perform better than the baseline only for larger over-all shifts. It is a little slower and is not expected to have any advantage for apertures that have a lot of overlap.

6.4 Summary

From the performance comparison between MIRA and baseline CC in chapter 4 an enhanced CC algorithm that overcame shift and noise biases, and expanded the region of applicable registration is desired. What has been detailed here is a technique that takes known quantities of the optical system and SNR as inputs and uses them to estimate the shape that noise and zero-lag correlation bias has in the CC function space. If these are carefully measured and directly subtracted from the function space, the remaining enhanced CC function is shown to select the correct peak in situations where the baseline CC utilized in the chapter 4 sensitivity analysis would fail. This effectively expands the viable region of operation of the baseline CC registration function, and is most effective at relatively low SNR and large shifts between data volumes. The next chapter characterizes this effect with another sensitivity analysis when applied to a simulated laboratory target.

CHAPTER 7

ENHANCED 3D CROSS-CORRELATION ALGORITHM SENSITIVITY

As was just shown previously, baseline CC generally outperforms MIRA for this type of data set. The next goal was to employ a sensitivity analysis between the baseline CC algorithm of Chapter 5 to the theoretical enhanced CC algorithm overviewed in Chapter 4. The sensitivity analysis process is much the same, with simulated PHD generated from a complex target and passed through SNR, shift and support iterations identically processed as in Figure 25. There were two key differences between this sensitivity analysis and the one used for comparing MIRA the baseline CC algorithm. Firstly, the target was changed to be one more easily reproducible for a laboratory experiment to benchmark these algorithms. Secondly, following the desired laboratory approach, the PHD is generated through image plane detection with a circular aperture following the process in Figure 9 instead of square aperture pupil plane detection as in the previous chapter.

7.1 Simulation and Experimental Imaging and Registration Analysis

The target model of interest is 3D with combinations of sparsity and non-sparsity in range and cross-range. It would also have several slanted surfaces that distribute the signal return energy between range bins. The model shown in Figure 32(a,b) was designed with this in mind, and with easy reproducibility for experiment validation.

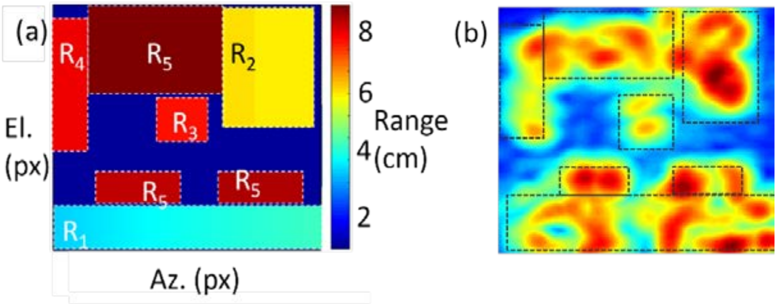

Figure 32: a) The simulated and experimental target model has several bright plates composed of retro-reflective tape which are separated into five range groupings R1-R5 in order of total range to detector and 225 cross-range bins (pixels). The flat plates starting at R1 and R2 are slanted which distributes the range return between range bins (b). The reconstructed experiment image (c), summed over all the range bins to show the target shape. The range cross-range-cross-range images from simulated data (d) and experiment reconstruction (e). The corresponding regions the target and the reconstructed images are highlighted in with dashed lines.

The range – cross-range –cross-range image shown in Figure 32(a) can also be represented with a composite range profile of the target reminiscent of the recovered single pixel range profile of Figure 16(e), but in this case, each pixel's range profile contributes to the total range contributions of the entire target, as shown in Figure 33

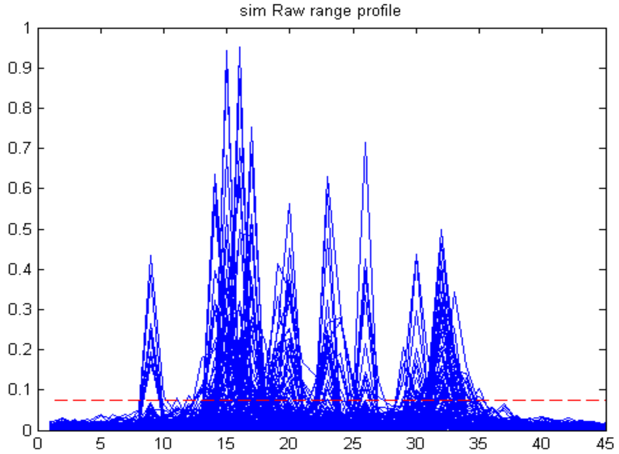

Figure 33: Normalized Composite Range Profile for a 15x15 support image. The estimated noise bed is highlighted in the dashed line, with the high SNR peaks indicating range

returns. The relative height of the peaks is indicative of reflection intensity from the pixel.

Comparing Figure 33, there are several sparse range locations between the 8th and 34th range bin. The cluster of returns between bin 14 and 17 are the slanted ramp, indicated as R1 in Figure 32(a). Combining interpretations of these two describes a target that has areas of sparsity and continuity in range and cross-range, similar to the backhoe target which was simulated in Chapter 5.

The simulated aperture data volumes are generated by propagating the reflected field from a phase tilted target to the aperture plane. The raw field at the aperture consists of a finely sampled speckle pattern. By integrating the focused field at the image plane according to available pixel support and taking the inverse Fourier transform to the aperture plane, low-support apertures are generated following Figure 34. The aperture support was adjusted by cropping the low resolution 15x15 aperture to the desired support.

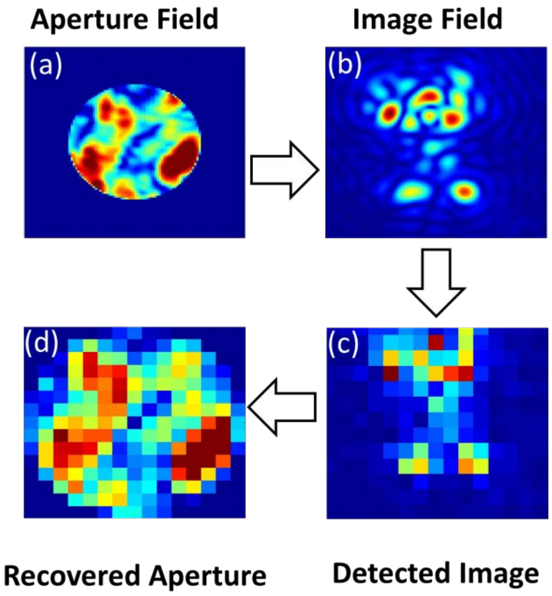

Figure 34: The simulated aperture field generation process. Support is varied by cropping the propagated field with a smaller circular aperture. The image is refocused and the speckle sizes are matched to 1.5-2 pixels in diameter and integrated in the detector. A low support aperture is recovered by taking an inverse Fourier transform.

To simulate noise, the aperture signal volume is scaled to a power factor relative to the Gaussian distributed noise volume following Eq. (36) for each SNR and speckle realization, registration is done between the first slow-time sample and every other subsequent slow-time sample to assess accuracy for different amounts of pixel shift. This whole process is repeated for different support apertures, and the outputs of the simulation are percent-in-error pixel shift and piston phase variance for each support and shift scenario.

7.2 New metrics for algorithm convergence

When comparing competing CC registration algorithms, the common metrics of RMSE and Variance from Eqs. (71)-(73) are not as informative as when applied to a MIRA sensitivity comparison. This is due to the CC process producing multimodal parameter values which can skew the RMSE. Figure 31(d) shows the enhanced algorithm is most effective as the pixel shift increases compensating for false peaks near the center. The RMSE is appropriate for characterizing small deviations about a truth value; however, just a few registration parameters from a spurious peak are enough to significantly skew an RMSE or variance measurement. Therefore, a “percent error” metric was adopted, where the number of registration parameters in a dataset that fall within acceptable tolerance are compared with the number that are out of tolerance. The basis of the metrics are logical functions for the azimuth X_n and elevation, Y_n, registration parameters out of tolerance are given as

$$X_n = \begin{cases} 1 & \text{if } |x_s - x_n| > tol_{XY} \\ 0 & otherwise \end{cases} \qquad Y_n = \begin{cases} 1 & \text{if } |y_s - y_n| > tol_{XY} \\ 0 & otherwise \end{cases}, \tag{85}$$

where tol_{XY} is a given tolerance, x_1 ,y_1 are the known azimuth and elevation shifts between the slow-time sampled apertures, and x_n , y_n are the n^th^ measurements of these shifts. For cross-range, percent in error is defined a

$$P_{ErrXY} = 100\left\{\frac{\sum_{n=1}^{M}[X_n \vee Y_n]}{M}\right\}, \tag{86}$$

where $\vee$ is the logical OR operator such that the total number of coupled registration parameters out of tolerance are counted over M total measurements. Similarly, the percent phase error is

$$P_{Err\Phi} = 100\left\{\frac{\sum_{n=1}^{M}\Phi_n}{M}\right\} \qquad \Phi_n = \begin{cases} 1 & \text{if } |\phi_s - \phi_n| > tol_\Phi \\ 0 & otherwise \end{cases}, \tag{87}$$

where ϕ_s and ϕ_n are the true and n^th^ observed shift, respectively. To remain diffraction limited, the cross-range and phase registration tolerances are $tol_{XY} \leq 1/7$ pixels (0.14 pixels) and $tol_\Phi \leq \lambda/14$ waves based on the Maréchal criterion [21].

7.3 Simulation Results and Discussion

Good registration will be indicative of viable aperture gain. Following the Marachel criterion, a shift error of 1/7 pixel in either cross-range direction was chosen as the acceptable tolerance. Similarly, a piston phase variance of 1/14 waves was chosen as a metric for precise phase measurements. Figure 35 and Figure 36 show the cross-range aperture shift and phase sensitivity curves over many different levels of SNR, support and aperture separation. The CPIs were processed with the baseline CC function from Eq. (70), and the enhanced function following Eq. (84)

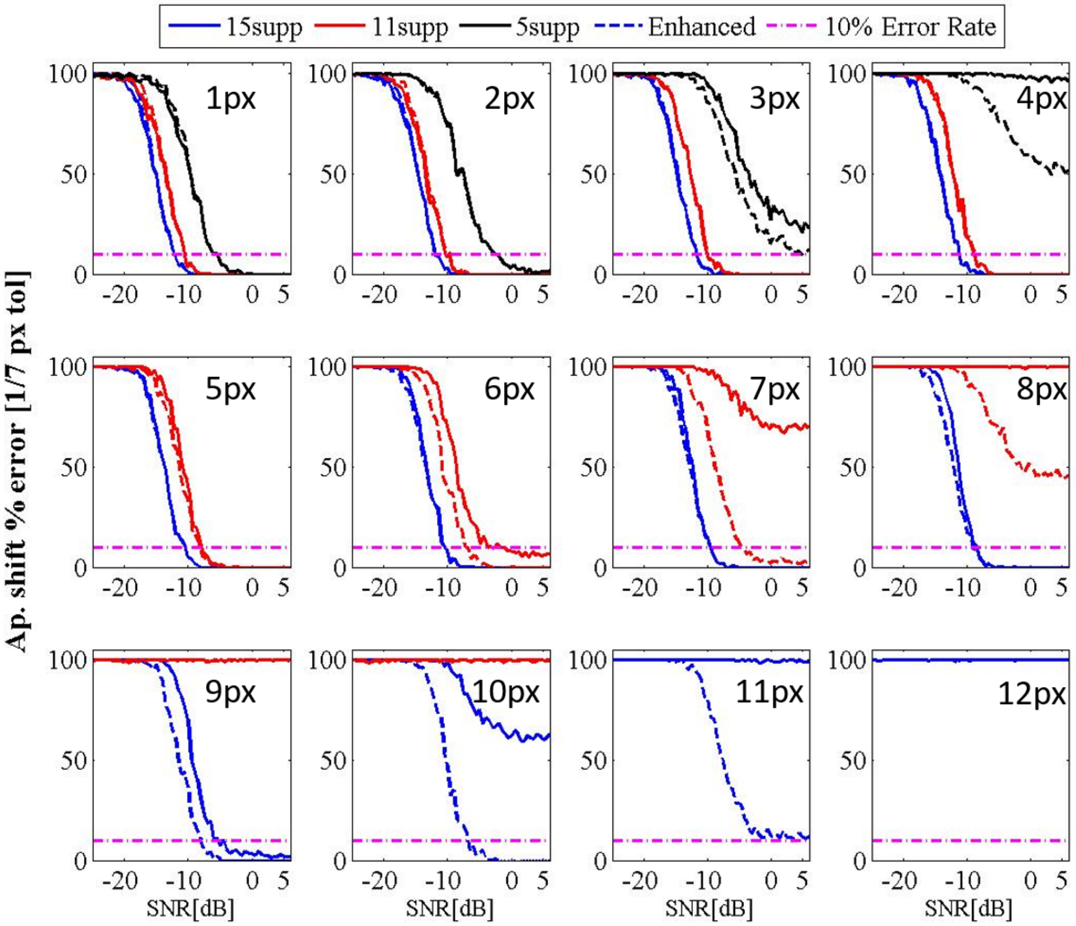

Figure 35: Simulated Registration shift convergence for 1-9 pixels of shift and 5, 11, 15 pixel diameter apertures with .1pixel error tolerance. Solid and dashed lines are the baseline and enhanced algorithms respectively applied to simulated volumes. Each panel corresponds to an azimuth shift in pixels between registered volumes of given support.

It was expected that as the shift between volumes was increased and the location of the correlation peak moved further from center, that increasing registration biases would occur exacerbated by additive noise. The enhanced algorithm was expected to increase registration within tolerances at greater shifts and provide several dB of noise sensitivity improvement.

Comparing the shift errors as a function of aperture separation and SNR shown in, Figure 35 the algorithm performance can be divided into 4 regions as shown in Table 2

Table 2: Enhanced Cross-Correlation Pixel Shift Registration Utility Regions

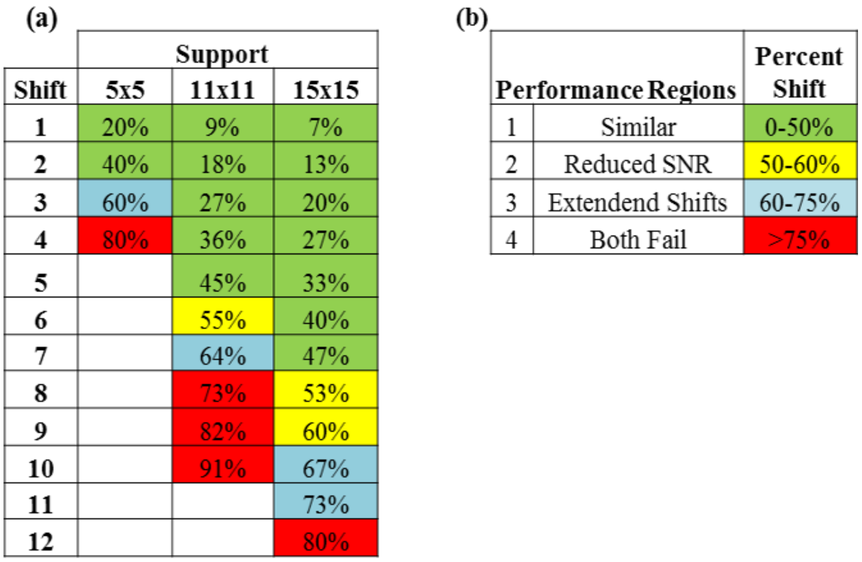

(a)

	Support		
Shift	**5x5**	**11x11**	**15x15**
1	20%	9%	7%
2	40%	18%	13%
3	60%	27%	20%
4	80%	36%	27%
5		45%	33%
6		55%	40%
7		64%	47%
8		73%	53%
9		82%	60%
10		91%	67%
11			73%
12			80%

(b)

Performance Regions		**Percent Shift**
1	Similar	0-50%
2	Reduced SNR	50-60%
3	Extendend Shifts	60-75%
4	Both Fail	>75%

Table 2(a) shows pixel shift error performance over the percent shifts for each support and pixel of shift color coded by Region of Performance where green indicates similar performance, yellow indicates regions where the enhanced algorithm registers at lower SNR, cyan indicates where the enhanced algorithm registers but the baseline algorithm fails and red where both algorithms fail. Table 2(b) gives a generalized performance summary with respect to shift. In detail, the the regions are:

REGION 1: At low shifts (0-50%), the baseline and enhanced algorithms perform similarly. This was expected since near zero shift, the shift peak is near the center of the autocorrelation where the noise has less impact and the amount of correlated area between sample is maximized.

REGION 2: At moderate shifts (50-60%), the enhanced algorithm provides registration within tolerance at SNRs up to 5dB lower than the baseline algorithm. It this region, both algorithms converge; however, the enhanced algorithm's suppression of the noise cross correlation pedestal and correlation peak height compensation for large shifts provides registration at significantly lower SNR.

REGION 3: For larger shifts (60-75%), the enhanced algorithm provides accurate registration at shifts significantly beyond where the baseline algorithm fails. In Region 3 the compensation algorithms provides the maximum compensation with the largest relative reduction of the noise pedestal and highest gain in the correlated signal peak height resulting in enhanced performance.

REGION 4: For the largest shifts (>75%), both algorithms fail. At this point, the amount of correlated signal is reduced to a point where neither algorithm can detect the correct autocorrelation peak.

Comparing the shift error over aperture separation and SNR draws a number of conclusions. It was expected that as the location of the correlation peak moves further from center, registration biases will occur with additive noise. and that the enhanced algorithm would show several dB of noise sensitivity improvement. Figure 35 shows the percent of registration iterations for a given shift and SNR that were in error in either cross-range dimension according to the 1/7 pixel tolerance. The general trend in Figure 35, shows that once subsequent appertures overlap less than 70%, (2 pixels in the low support case, 4 pixels in the medium support case and 5 pixels in the large support case), the enhanced algorithm outperforms the baseline algorithm. In the lower support case, and 3 pixel of shift, the enhanced algorithm still converges to less than 10 percent error. The trend continues at medium support and 5 and 6 pixels of shift, the enhanced algorithm also has a 2dB and 4dB improvement respectively. At 7 pixels of shift for this support level, the enhancements still allow the registration to converge. For the highest considered support, at 7 pixels of shift the SNR of convergence has 1dB of improvement with the enhanced algorithm. The sensitivity showed large SNR improvements, of >5dB at 9 and continued convergence at 10 and 11 shift. These enhancements are most pronounced near a critical overlap between sup-apertures. In the 3 pixel shift case, where neither the medium or large support apertures have such little overlap between subsequent samples, the baseline and enhancements show near identical results. Similarly, in the 1 pixel of shift case, all considered analyses show similar results. It is inferred that higher support is not as important as aperture overlap, as registration was still possible with only a 5 pixel diameter aperture at 60% overlap. There is still a difference between support levels, with the overall number of correct registrations being higher with lower support, and with noise sensitivity being worse, as shown for instance in the 1 pixel shift case for all support levels. Phase convergence shows similar trends as percent in error with respect to pixel shift Figure 36 shows the percent error in the piston phase differences between registered volumes.

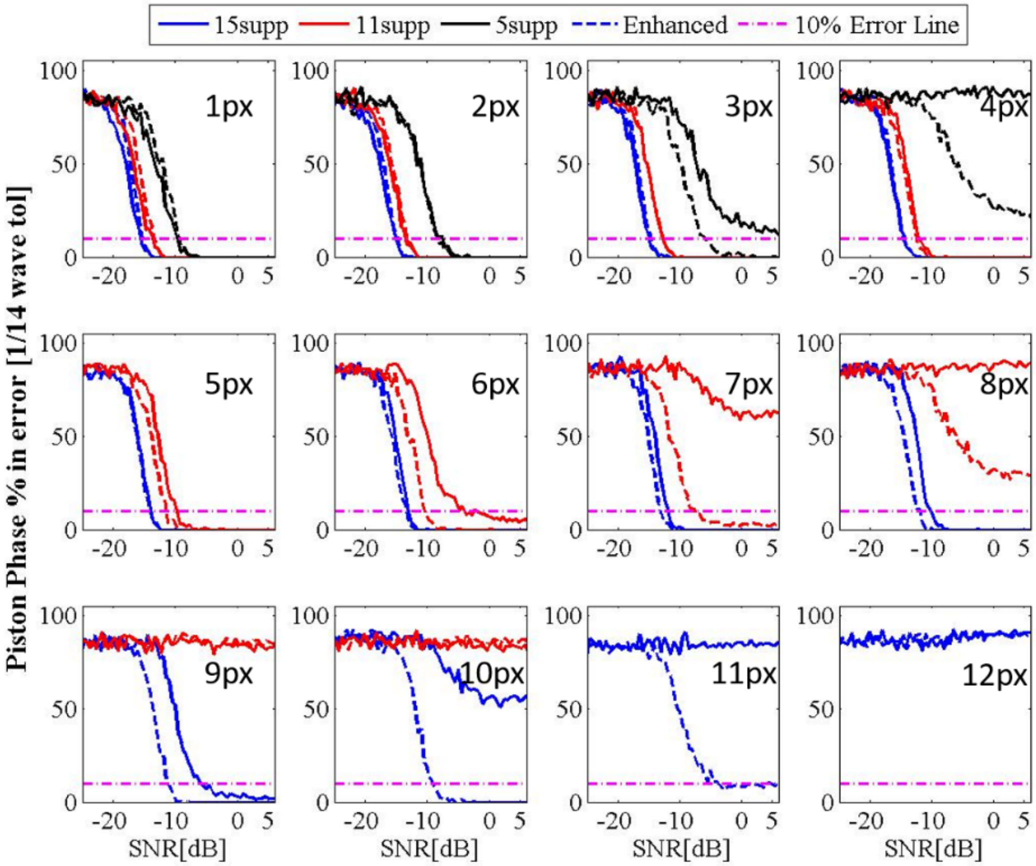

Figure 36: Simulated phase percent in error over azimuth shift and SNR. Tolerance is set to .14 radians of piston phase error, with a 10% error set as the margin for poor overall performance.

From above, Error rates greater than 10 percent are shown as the magenta dashed line and indicative of non-convergence of the phase registration. The lowest support case shows an improvement of ~4dB for crossing the tenth of a wave convergence line between the enhanced and baseline algorithms at 2 pixels of shift. Similarly, the medium support case at 5 pixels of shift show ~6dB over the same criterion. For the highest support at 8 pixels of shift (47%

overlap) the tenth of a wave criterion between either algorithm is reached at a difference of 2dB. At 9 pixels of shift (30% overlap), this trend continues but with an SNR difference of 5dB in the 10th of a wave criterion and 10dB in the 20th of a wave criterion. For 10-11 pixels of shift the baseline algorithm never converges to the desired phase variance. These results are summarized in Table 3

Table 3: Enhanced Cross-Correlation Piston Phase Registration Utility Regions

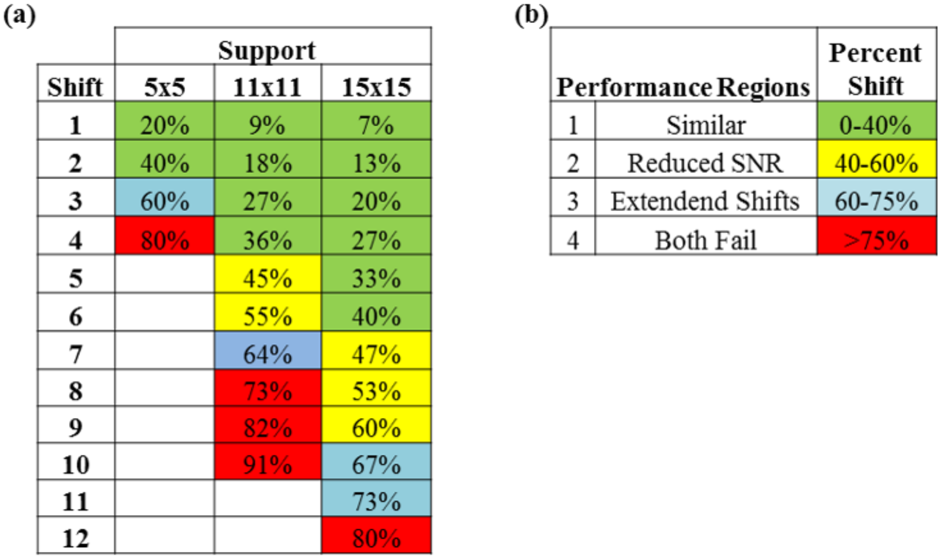

(a)

	Support		
Shift	**5x5**	**11x11**	**15x15**
1	20%	9%	7%
2	40%	18%	13%
3	60%	27%	20%
4	80%	36%	27%
5		45%	33%
6		55%	40%
7		64%	47%
8		73%	53%
9		82%	60%
10		91%	67%
11			73%
12			80%

(b)

Performance Regions		**Percent Shift**
1	Similar	0-40%
2	Reduced SNR	40-60%
3	Extendend Shifts	60-75%
4	Both Fail	>75%

Table 3(a) follows same scheme as Table 2(a), showing the percent shifts for each support and pixel of shift color coded by Region of Performance where green indicates similar performance, yellow indicates regions where the enhanced algorithm registers at lower SNR, cyan indicates where the enhanced algorithm registers but the baseline algorithm fails and red where both algorithms fail. Table 3(b) gives an approximate performance summary over all supports.

While it may seem odd that the piston phase convergence is less sensitive than the shift, this is due to the difference in tolerances required for the percent error metrics treated separately in pixel shift (Eq. (86)) and piston phase (Eq. (87)). Piston phase is calculated by taking the angle of the correlation peak in cross-range. With a relatively wide error criterion in piston and a narrow criterion in pixel shift, the algorithm will often register out of tolerance in pixel shift, but the location to which it registers will have a measured angle that is within tolerance, hence the apparent reduced sensitivity in piston phase from the chosen convergence metric.

7.4 Enhanced Cross-Correlation Summary

A new approach for improving the cross correlation registration algorithm for ISAL in the presence of small sampling support additive noise and small sub-aperture overlap was demonstrated for simulated, complex volume targets. For rotating targets at significant range, the field propagation was mapped between target and aperture spaces and an appropriate 3D data volume registration algorithm was successfully applied and tested for this multi-pixel ISAL imaging scenario. Four performance regions were defined based on the aperture plane shifts as percentage of the detector support. The regions were similar for both shift and phase accuracy. In Region 1 (0-40% shift), both algorithms had similar performance. In Region 2 (40-50% shift), the enhanced algorithm achieves an error rate of less than 10% is achieved with 1-5dB of SNR performance gain over the baseline algorithm. In Region 3 (60-75% shift), the baseline algorithm does not converge at all; however, the enhanced algorithm provides registrations within tolerance over this extended range. In Region 4 (>75% shift), both algorithms fail. Many ISAL imaging scenarios operate at greater than 50% shift between aperture collections where aperture gain may be more important than side-lobe suppression. These enhanced algorithm proffers new options for data collection budgets where more quickly rotating targets can still be successfully interrogated, without the need for a higher pulse repetition rate, which also improves power requirements for interrogation. The improved algorithm robustness with respect to aperture shift also allows for a synthesized aperture to be reconstructed with fewer pulses, which improves system flexibility.

CHAPTER 8

PARRALLEL-PIXEL ISAL SYSTEM FOR ALGORITHM BENCHMARKING

The main motivation for this experiment approach was to test the volumetric registration algorithms on a low support target with sparsity and continuity in range and cross-range. If similar volumetric PHD could be generated at varying SNRs a volumetric registration sensitivity analysis benchmark of the algorithms could be undertaken. Another motivation for this project was a feasibility study for a 1.55 micron focal plane array approach for multi-pixel temporal homodyne coherent imaging. Such a system interrogates several regions of the target and forms a full 3D complex valued data volume image of the target with the option for aperture synthesis for improved cross-range resolution. This system is possible through the latest commercially available high speed telecom wavelength focal plane arrays. The FPA detector is fast enough that when paired with a stretch-processed high bandwidth interrogating source, the resulting signal from Eq. (54) may be properly sampled for range compression and phase tracking which allows for aperture synthesis.

8.1 System Limitations

As will be shown in this chapter, the imaging system was incapable of a complete real-world benchmarking of the algorithm sensitivity analysis applied in simulation in Chapter 6. For diffraction limited aperture synthesis, the phase needs to be adequately tracked and compensated between all slow-time samples, and between all imaging pixels. A number of real-world noise sources will cause phase errors that alter the image and therefore decrease correlation amplitude between frames. This is critical, because the purpose of a sensitivity analysis is to measure the volumetric SNR where registration algorithms at a particular shift and support level break. If some other source of noise is effectively decreasing the correlation function SNR (or the level of the correlation peak with respect to the noise floor), then the sensitivity results will be different. Due to unforeseen issues with the camera, the rotation stage and the timing system intended to synchronize frequency between LFM pulses, the field was shown to evolve slightly between samples. This evolution decreases the correlation SNR, and skews the resulting sensitivity results from those seen in simulation and therefore an unambiguous sensitivity benchmarking of the algorithms unable to be performed.

The results of the experimental sensitivity analysis were still useful and noteworthy. The registration algorithms still showed utility when applied to experiment data volumes. The enhanced algorithm showed no signs of being worse a performer than the baseline algorithm, and the both were able to consistently converge for given SNR, support and shift. The experiment system was capable of fast 3D imaging, with phase tracking facility. This approach of Flash-LiDAR ISAL utilizing fast focal plane array is sound, but requires careful system design for keeping track of the phase between aperture samples.

8.2 LFM Processing Techniques

For a stretch processing system the detected signal follows Eq.(54) and the analytic signal is Eq. (55). There are additional pre-processing techniques for real system that are needed to obtain this signal. As an initial test of range resolution the raw signal taken from the LFM was mixed in fiber with a delay line and recorded on an oscilloscope. The resulting beat signal and corresponding IPR, with matching theory is shown in Figure 37

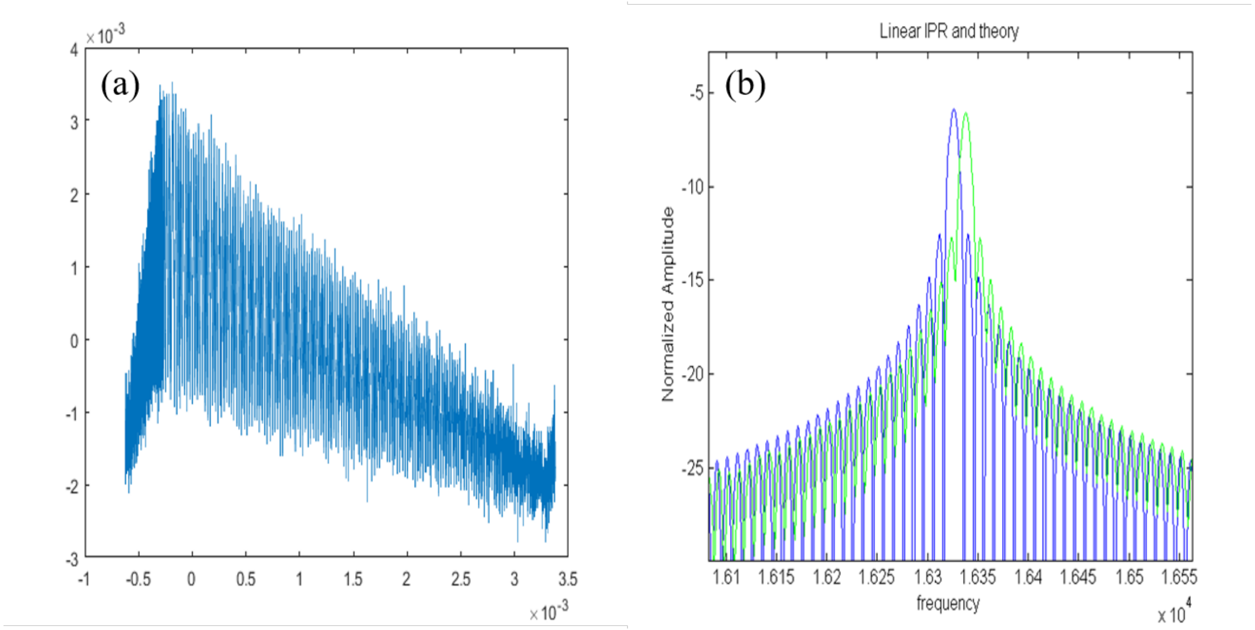

Figure 37: Measured LFM beat frequency with a 1m delay on oscilloscope (a) and Fourier transform in green (b) showing the range resolution of the IPR when compared to theory in blue. The green and blue curves have been shifted to improve visibility.

As seen in the figure, the LFM signal directly from the laser source had a frequency dependent amplitude bias, where the beginning of the frequency sweep had twice the amplitude recorded at the detector. As this amplitude resets with each LFM pulse, it can be used to discriminate between slow-time pulses and separate each pulse to fast time and slow-time components before additional processing. The first step of data collection was to take “dark frames” of only the LO spot on the detector by covering the transmit aperture, average their intensity per slow-time and subtract from the mixed signal. This effectively “de-ramps” the signal and then standard Fourier processing can recover the range profiles, phase and aperture fields from the data following Figure 38

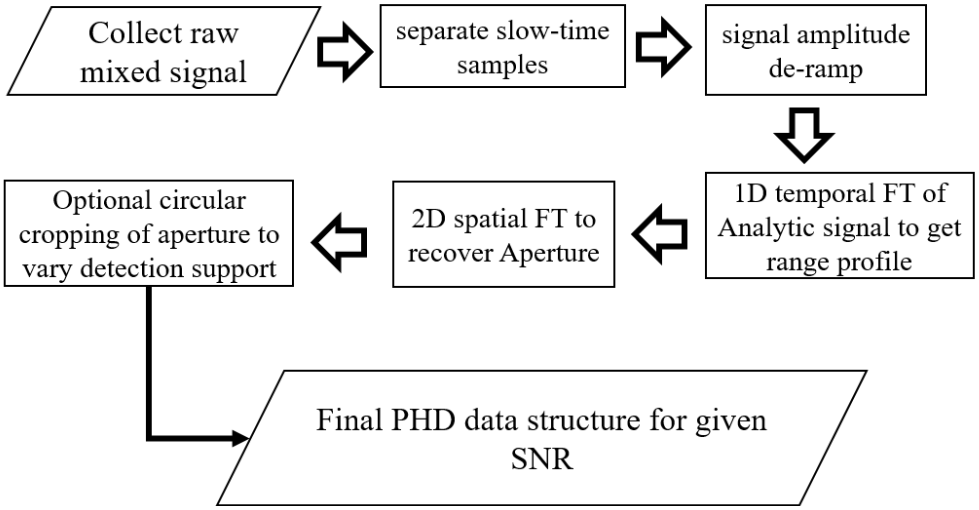

Figure 38: Processing raw LFM signal to 4D complex data volume. The final result has three dimensions of space, azimuth and elevation separated by individual pixel histories, range recovered from fast-time temporal record, and slow-time pulses separated out from the original fast-time only record. This is saved in a structure organized to different SNRs.

This process creates multi-dimensional PHD which is viable for aperture synthesis alone slow-time of 3D complex data volumes. It is a near identical process as shown in Figure 34, just with additional real-world processing to convert a raw LFM signal to a data volume.

8.3 Experiment Benchmarking Setup

The temporal homodyne "parallel-pixel" ISAL system uses a Bridger continuous wave 45GHz bandwidth LFM signal laser which achieves range compression through stretch processing, or path matching the return signal with a local oscillator. The detector is a Xenics Cheetah SWIR camera set to a 70 kHz framerate which is fast enough to treat each pixel as an independent detector such as those used in typical single pixel ISAL systems. The camera and laser were designed to sample a stable portion of each LFM ramp reset and generated data volumes consisted of 90 fast time samples per slow-time measurement, for a range window of ~15cm with ~3.5mm resolution.

Summarized system capabilities are as follows

Table 4: System Capabilities

3D Multi-pixel ISAL System	
Center frequency f_0	~1.549 μm
Chirp rate α	34.066 THz/sec
Stable Sweep time T_p	1330 μs
Total BW	45.31 GHz (used BW = 41GHz)
Repetition Rate	500 Hz
Range Resolution	3.6 mm
Camera Frame Rate	70kHz
Used Range Window	162mm

The target was composed of slated flat plates made and surfaces covered in retroreflective tape. The motivation for this was to have a high a dynamic range of SNR as possible for the sensitivity analysis. The high reflectivity and wide cross-section targets, combined with the focusing capability of the image plane detection scheme made this possible. A “detector view” and bird’s eye view of the target is shown in Figure 39, which can immediately be compared to the simulated

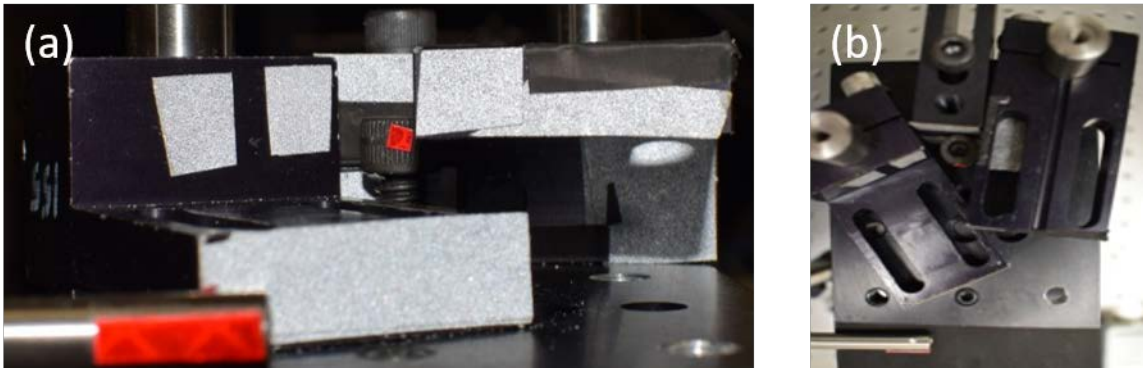

Figure 39: The rough angle the detector views the target is shown in (a). The center screw holding the platform to the rotating stage has a brighter reflectivity tape affixed to it which is a red color. This tape is also attached to a stationary reference target which is located closer to the first range bin of the window. The range separation and slanted profiles of the plates is more evident from a bird's eye view shown in (b).

The target in Figure 39 was mounted to a rotation stage, which supplied the shifts in the 3D aperture fields. An experimental setup block diagram is shown in Figure 40

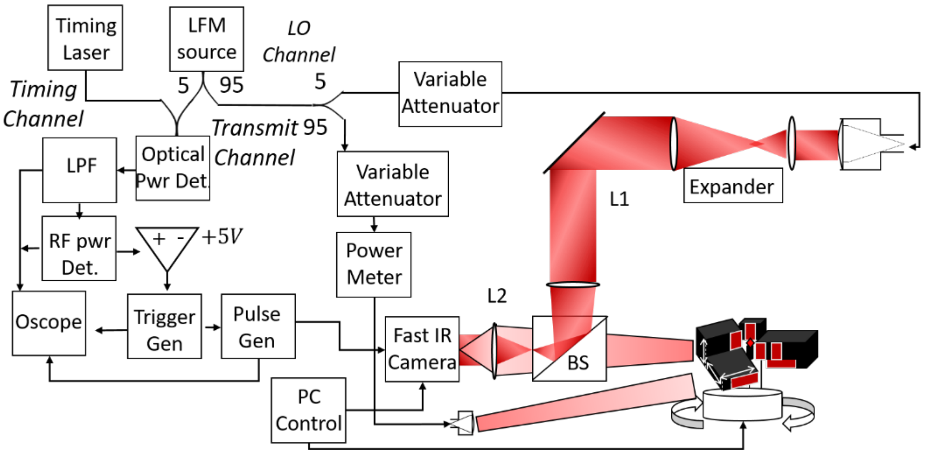

Figure 40: Experiment diagram: The LFM is split into three legs. The timing leg synchronizes times between LFM pulses, the LO leg is path matched to the target and allows for coherent detection and the signal leg sends a 10cm footprint to a rotating target which is collected on a fast IR camera.

From inspection of Figure 40 the system may be divided into several subsystems. First the LFM source is split between a Timing system and a Signal/LO system which illuminates the detector.

The camera is designed to take a snapshot after receiving a +5V trigger, and the laser automatically resets its frequency sweep at a 500Hz rate. Range compression was only possible if subsequent LFM pulses were properly synchronized, which required a timing system as shown in Figure 41This timing system consists of a narrow linewidth PS-TNL laser set to 193525.0GHz , mixed with the Bridger LFM laser in an optical power detector. The detector output is fed through a <500MHz low pass filter and into an RF power detector. This output power signal will be a voltage spike which occurs whenever the LFM is within 500MHz frequency of the seed laser, and this is passed into an operational amplifier circuit and to a digital delay generator, which sends a singular pulse to another triggered waveform generator each time it receives this voltage spike. The final waveform generator is programmed to send 90 +5V pulses at a 70kHz rate to the camera, which takes a frame every time it sees one of these pulses. The timing system total output, including the pulses sent to the camera are shown in Figure 41

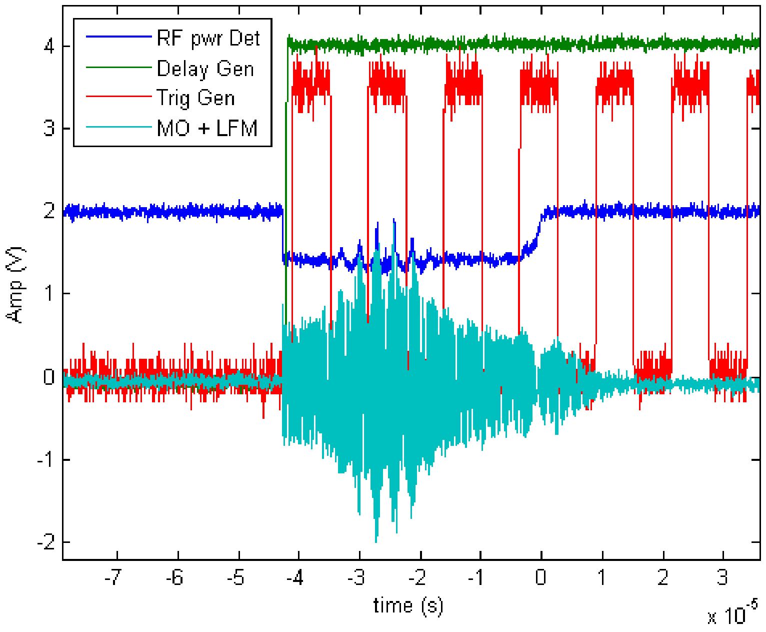

Figure 41: Timing System Output. The turquoise is the laser amplitude over time (and frequency), with the bump showing the mixing region of the LFM with the narrow line-width tunable laser. This output was picked up by the RF power detector in blue, which sent a signal to an Op-AMP and then the delay generator (green), The pulse train to the camera is in red.

The mixing of the LFM with the narrow linewidth laser is shown in turquoise. This signal, after passing through a LPF and RF power detector shows up as the signal in blue, which triggers a logical pulse on a pulse digital delay generator, shown in green. The final pulse train generator is programmed to send 90 4.0V pulses to the camera (red) every time it receives this logical pulse. A close-up of the timing system is shown in Figure 42

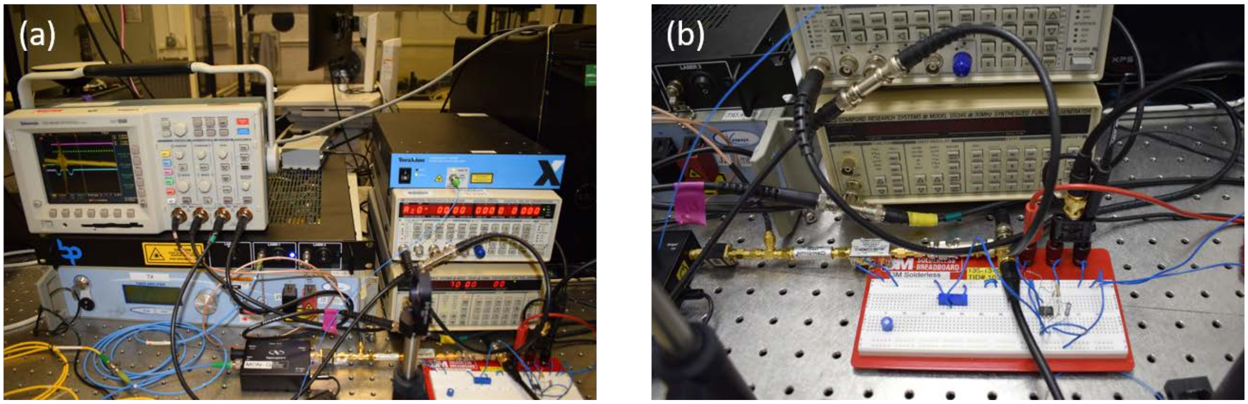

Figure 42: Timing system close-up. Just in frame in the bottom of corner (a) is the power detector and bandpass filter. The two pulse generators are on the right with the narrow linewidth laser on top. The timing signal is visible on the oscilloscope. The op-amp of the timing system is shown in (b) which is set to +5V

The local oscillator, helps amplify the signal which would otherwise be lost given the low integration time and gives the system its coherent detection capabilities. This leg of the LFM is attenuated to an appropriate level with a variable attenuator (such that the cameras power is filled to .25 fill and is not oversaturated), is collimated with a fiber collimator, propagated through air and expanded with a Newtonian beam expander, and sent through a simple optical system to keep it collimated on the FPA detector surface. The portion where mixing occurs is shown in Figure 43(a). The range to the target at the table edge is shown in (b)

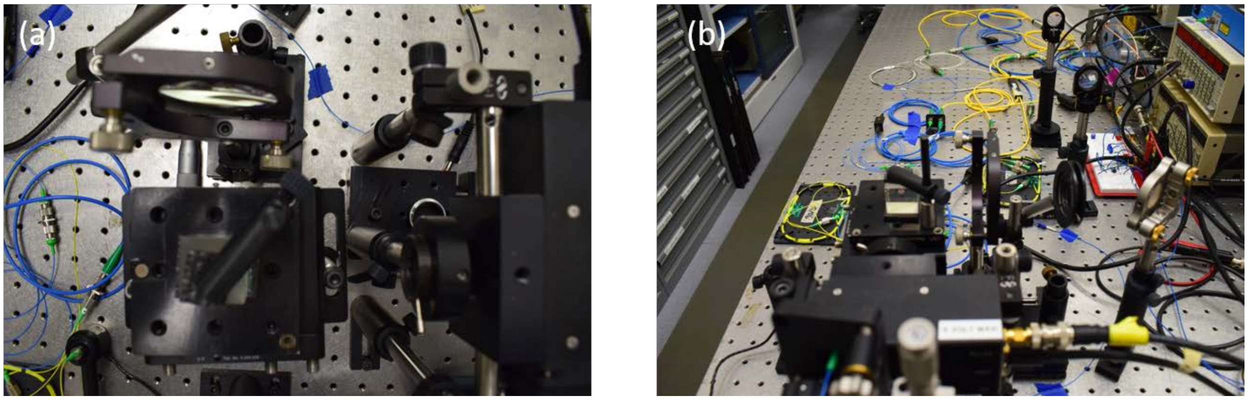

Figure 43: Focal plane mixing of LO and signal (a) with the large lens de-collimating the LO such that the imaging optic on the camera in the lower right of (a) re-collimates it. The beam cube is visible in the center of (b) with the transmit fiber near the lower left-hand corner of the photo and the range to target visible.

A photo of most of the fiber splits in the system, including the timing system and attenuators is shown in Figure 44

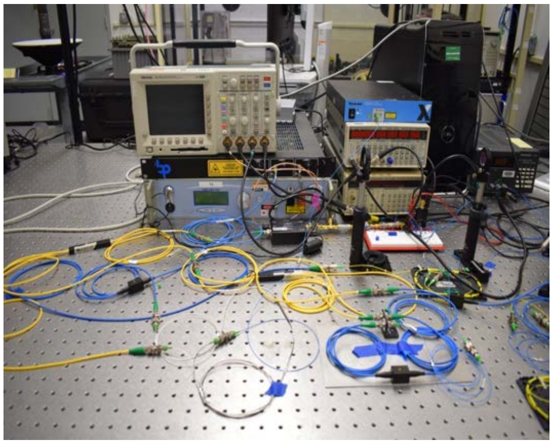

Figure 44: Experiment diagram: The LFM is split into three legs. The timing leg synchronizes

times between LFM pulses, the LO leg is path matched to the target and allows for coherent detection and the signal leg sends a 10cm footprint to a rotating target which is collected on a fast IR camera.

The camera software was programmed to take 3000 total frames per collection corresponding to roughly 34 slow-time pulses, with a 5 microsecond integration time per frame. One such data capture generates a full CPI, which is capable of being processed to a number of separate 3D complex-valued images equal to the number of slow-time samples. The camera requires a small field of interest for faster capture rates. Only a 16 row by 80 column field of interest is captured, of which only a 15x15 square field of view is considered. This is a bi-static system and the signal leg can be completely attenuated by simply covering the transmit aperture. The optical power of the transmit aperture was controlled with another variable attenuator with a power meter pick-off.

8.4 Imaging system limitations and suggested changes for Fielded System

This system had a number of limitations from the beginning that would not be appropriate for a fielded system and these diminished the overall imaging and phasing capabilities.

Some suggested changes for a fielded system intending a similar overall imaging approach:

- Decrease the laser bandwidth for lower resolution and wider range window
- Couple the camera outputs to a digitizer with more total memory for a longer total phase history (more fast-time and slow-time samples)

- Add a high bandwidth monitor pick-off for post-processing any phase issues in the signal attributed to system noise or instabilities

8.5 Experiment imaging capabilities

The system was capable of generating a full CPI in roughly a second of acquisition time which could be quickly processed to separate 3D images per slow-time sample. If the CPI was collected as the target was rotating, then registration between slow-time samples would yield the data necessary for aperture synthesis. As will be shown, system limitations led to an evolving aperture field over slow-time which could still be registered, but severely limited the viable length of a synthetic aperture. The piston phase of each individual pixel was also part of the complex date volume measurement over slow-time and instabilities here was likely the largest contributor to aperture field evolution.

8.5.1 3D Imaging and Phase Tracking

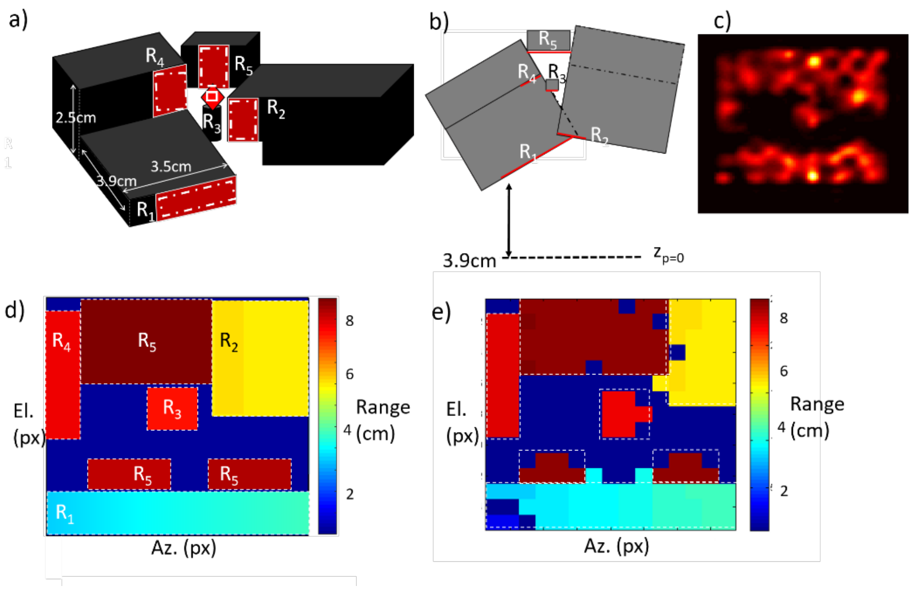

Figure 45: Comparison between target shape(a,b), recovered image field summed over all range bins to show the overall shape(c), theoretical, ideal cross-range-cross-range-range image (d) and the recovered image from real data (e) . The darkest color in the color maps is reserved for a thresholded zero-energy return, not a positive return from the first range bin.

From Figure 45(e) the recovered image is similar to what was expected theoretically. This image does not account for multiple range returns per pixel and was generated from the 3D data volume by outputting the range location of the highest reflectivity return for each pixel above a certain threshold. Notable differences include some dead or low-performance pixels which would appear as dark spots. The gradient color scheme due to the ramps in range shown in Figure 45(d) still shows up in (e), but is less of a gradient and more of a step wise function, which was due to limitations in range resolution. The reference target is visible in the bottom left hand corner, and is obscuring some of the ramp returns.

To complete the picture a composite range profile is shown in Figure 46.

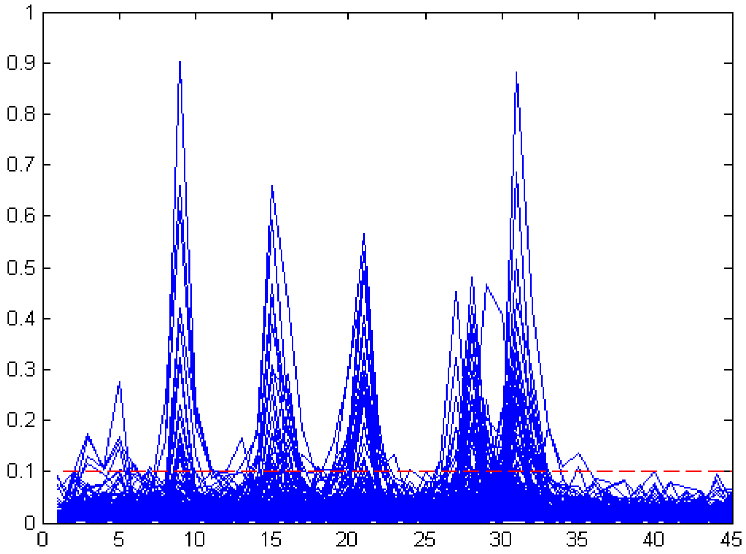

Figure 46: Composite Range Profile from experiment data volume. Dashed line is the estimated noise bed, showing a dynamic range between the noise and brightest scatterers as ~3dB.

The composite range profile can be immediately compared to the simulation of the same target in Figure 33, which even had a similar dynamic range. A full analysis of the recovered data volue is difficult to show clearly in a single figure, as it contains range, elevation, azimuth and grescale data, with many pixels located on target boundaries that have multiple range returns. A complete analysis requires inspecting each individual pixel and its singular range profile. The phase of each pixel is also measured over slow-time or between successive looks of a rotating target. An example of the piston phase tracking of two pixels on opposite sides of the center of rotation is shown in

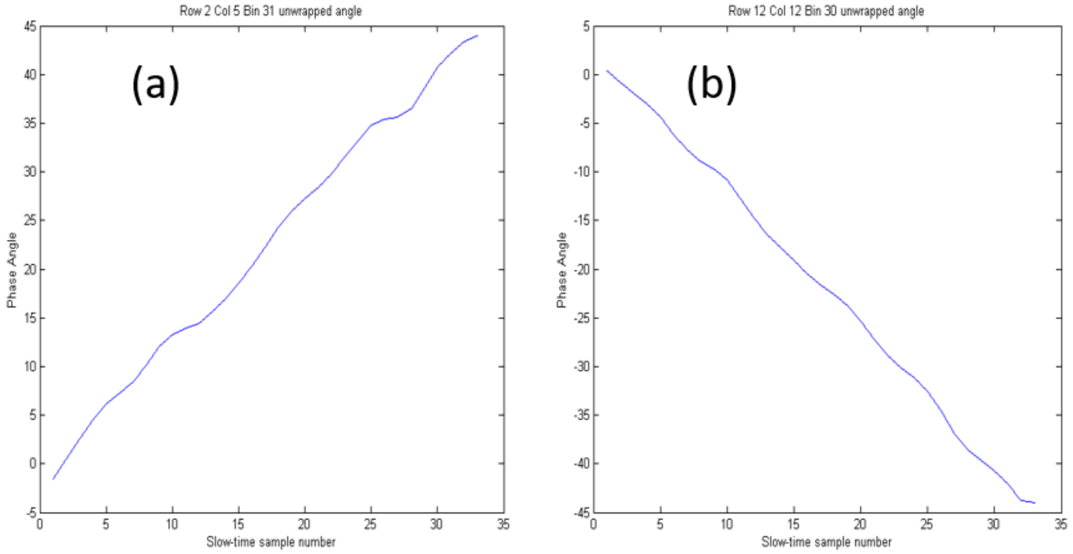

Figure 47: Phase tracking of a slowly rotating target with 15x15 pixels in the field of view. Rotation rate of 0.0026 degrees per slow-time sample, or 1.26 degrees per second. (a) is from a target located at row 2 , column 5 and range bin 31 and (b) is on the opposite side on row 12, column 12 and range bin 30. The phase is unwrapped and some noise is evident.

From the figure, there is clear noise in the unwrapped phase but it can still be tracked over slow-time and can be used for estimating the rotation rate and direction of the target.

8.5.2 Limited Aperture Synthesis

Figure 47 hints at imaging limitations related to phase retrieval, and this was ultimately shown to be the case when attempted a long synthesized aperture. System instabilities from a variety of possible factors including uncompensated table motion, timing system jitter, and phase curvature of the LO spot on the FPA led to what is best described as aperture field evolution over slow-time, which is demonstrated with recovered aperture fields from a single bright return range bin over several stage rotations in Figure 48.

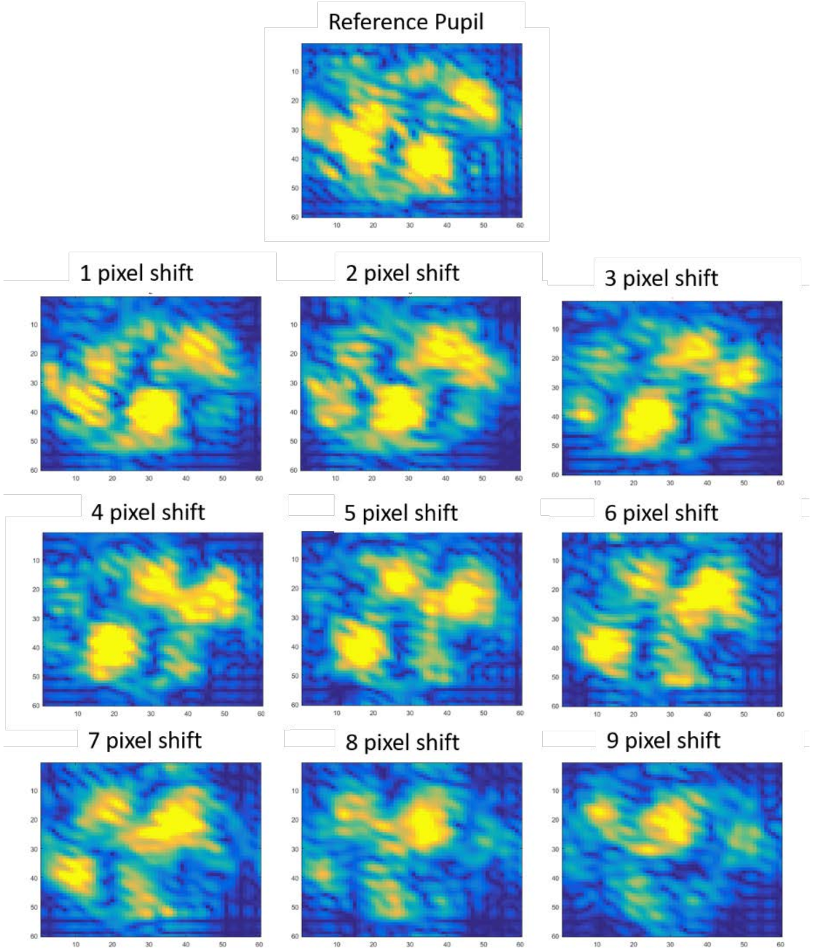

Figure 48: Recovered Apertures for different stage rotations. For visibility, the 15x15 pixel recovered apertures were upsampled by a factor of 4. The motion of the field is evident, but so is slight changes, or evolutions over the slow-time record due to phase instabilities.

The figure above shows the recovered aperture fields recovered from a stationary stage at different rotations corresponding to 1-9 measured pixels of shift between the reference and test images of the aperture field. Two important characteristics in this data are apparent, firstly fields are clearly shifting left between sub-apertures and are in fact registerable, and secondly the fields appear to be evolving during the shifts. The evolution is not large enough to completely de-correlate between “nearest neighbor” images, but is large enough such that the field at the end of a CPI is significantly different than at the beginning, and this greatly hinders the overall viability of aperture synthesis.

Nevertheless, some limited aperture synthesis was demonstrated but, in depth analysis was not conducted due to technical challenges in reducing the effects of aperture field evolution. Figure 49 shows a simple example result of registering 30 collected aperture samples 15x15 pixels in diameter which were shifted by 4 pixels each. 10 separate speckle realizations were taken for speckle averaging.

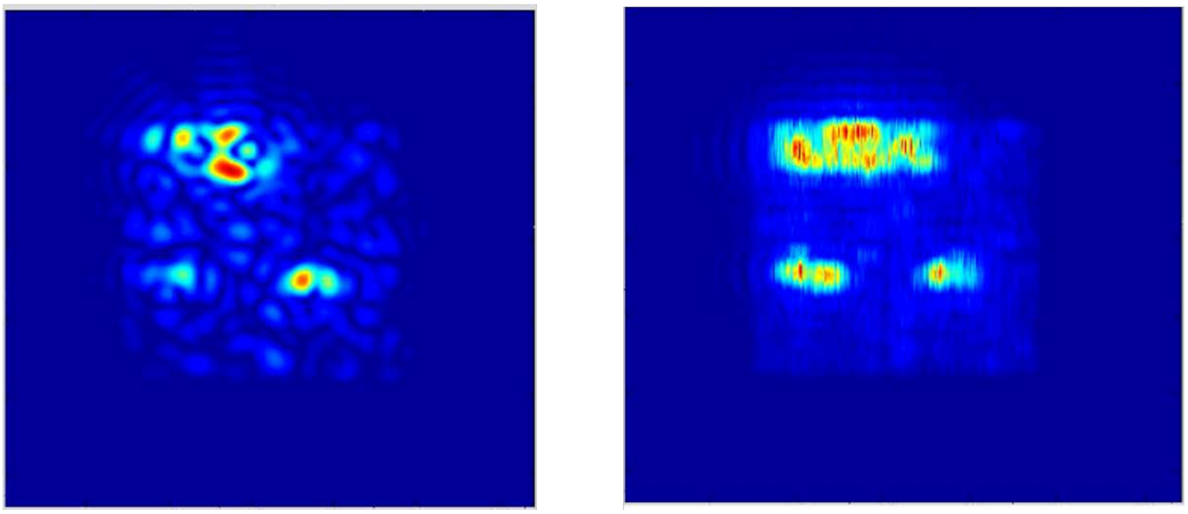

Figure 49: Simple Experiment Aperture Synthesis example. In-depth resolution gain analysis was not conducted, but simple inspection between the speckle averaged single aperture reconstructed image of a bright range bin, and a synthesized image show some gain in edge resolvability.

with a less noisy system with better phase tracking and less severe field evolution, collected images used to generated Figure 49 would be indicative of 8x resolution gain. The figure shows significantly less gain, but still showcases the registration capability of the system and some advantages of applying aperture synthesis to low support targets. Even with the modest resolution gain shown, edges are still made clearer and the target can be more readily identified.

8.6 Experiment Sensitivity Analysis and Processing

Rotating the stage in real time which would be similar to data collection of a real system, introduced significant phase noise in the signal which decreased registration performance. As a result, the processing method for algorithm benchmarking was changed for use with a stationary stage set at different positions. Instead of registering between nearest-neighbor slow-time pairs for a constantly rotating stage, registration was done by multiplexing slow-time sample combinations between different stationary stage positions for the CPI. In this way, Each SNR level had 200 separate registrations between shifted data volumes over 9 different stage positions, corresponding to 1-9 pixels of shift over a 15x15 pixel field of view. Support was varied, as in the simulation, by digitally cropping the recovered aperture post-process to 11x11 and 5x5 pixels. The optical power of the signal was attenuated in 1.0 dB increments over a transition region where SNR became too low for registration. The data was saved into a total structure organized by shift between sub-apertures, SNR, support and separate registration runs. This built the necessary statistics for a full sensitivity analysis such as the one done in Chapter 6.

8.7 Experiment Benchmark Results with Simulation Comparison

The results of the sensitivity analysis with respect to pixel shift are shown in in subplot format.

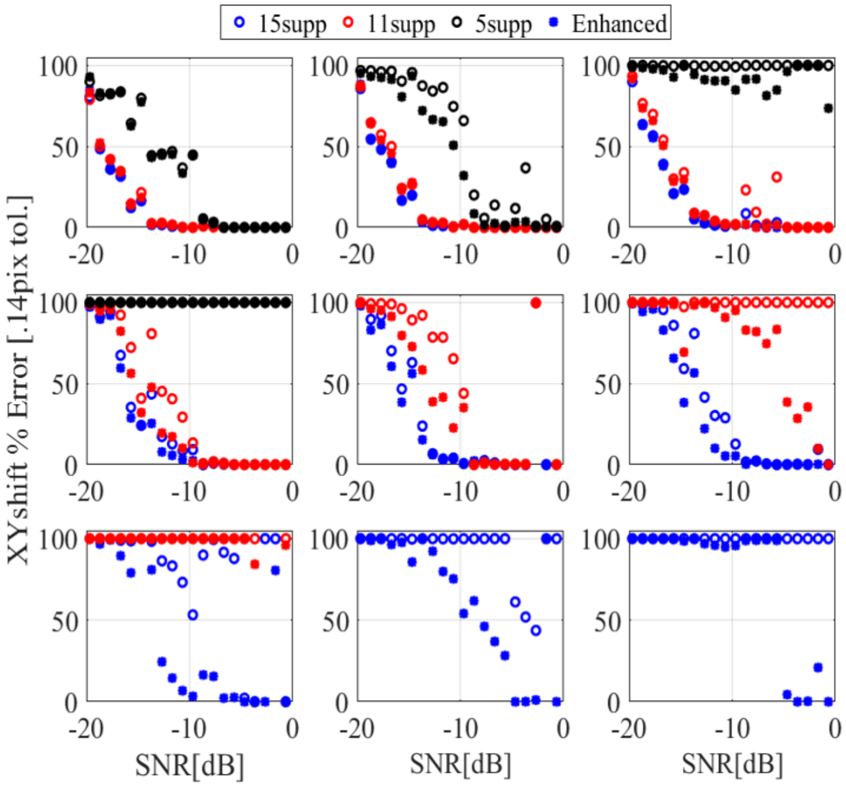

Figure 50: Experiment registration shift percent-in-error for 1-9 pixels of shift and 5, 11, 15 pixel diameter apertures with .25 pixel error tolerance. Solid circled lines are the baseline. Dashed asterisk lines are the enhanced algorithm. Each panel corresponds to an azimuth shift in pixels between registered volumes of given support.

The sensitivity analysis summarized in the figure above still shows enhanced algorithm utility when applied to experimental data. By inspecting the figure, the low support registrations converge for 1 and 2 pixels of shift, with some SNR gain through the enhanced algorithm at 2pixels of shift. There appear to be some positive effects of the enhanced algorithm at this support level for 3 pixels of shift, but it never converged in that case to below the 10% error rate.

For 11x11 pixels of shift, the registration converges until 5 pixels of shift, where some SNR gain is shown with the enhanced algorithm 6 pixels of shift in this case requires the enhanced algorithm to still converge. The trend continues with the highest available support of 15x15 pixels, whch converges until 7 pixels of shift with the baseline algoirthm which shows some enhanced algorithm SNR gain. The enhanced algorithm is required for convergence for 8 and 9 pixels of shift. These results are summarized in

Table 5

Table 5: Experiment Imaging Enhanced CC Performance Gains

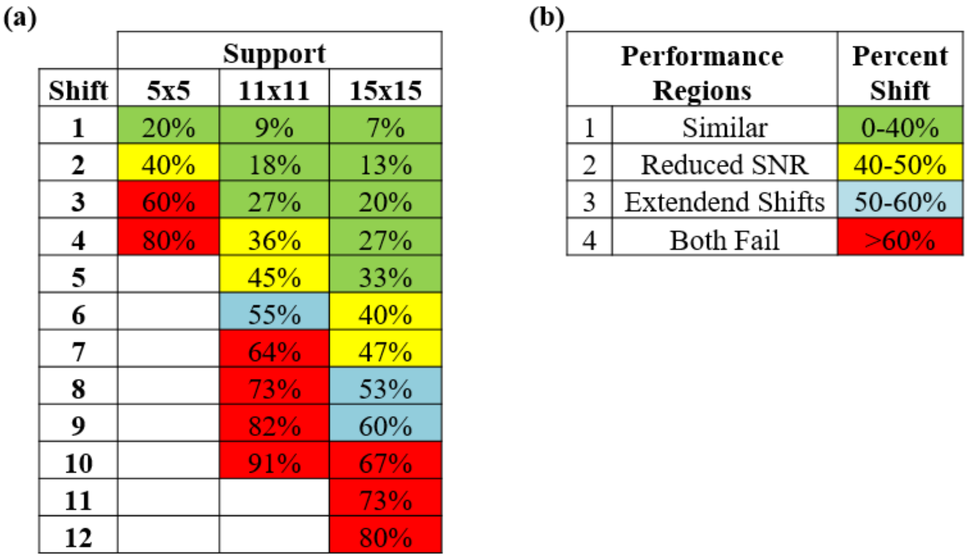

(a)

	Support		
Shift	**5x5**	**11x11**	**15x15**
1	20%	9%	7%
2	40%	18%	13%
3	60%	27%	20%
4	80%	36%	27%
5		45%	33%
6		55%	40%
7		64%	47%
8		73%	53%
9		82%	60%
10		91%	67%
11			73%
12			80%

(b)

Performance Regions		**Percent Shift**
1	Similar	0-40%
2	Reduced SNR	40-50%
3	Extendend Shifts	50-60%
4	Both Fail	>60%

Table 5(a) shows the same regional behavior of perfomance gain as in Table 4 and Table 3, only the regions have all been shifted to higher overall sub-aperture overlap. A direct comparison of the simulated sensitivity analysis and the experiment is shown in Figure 51

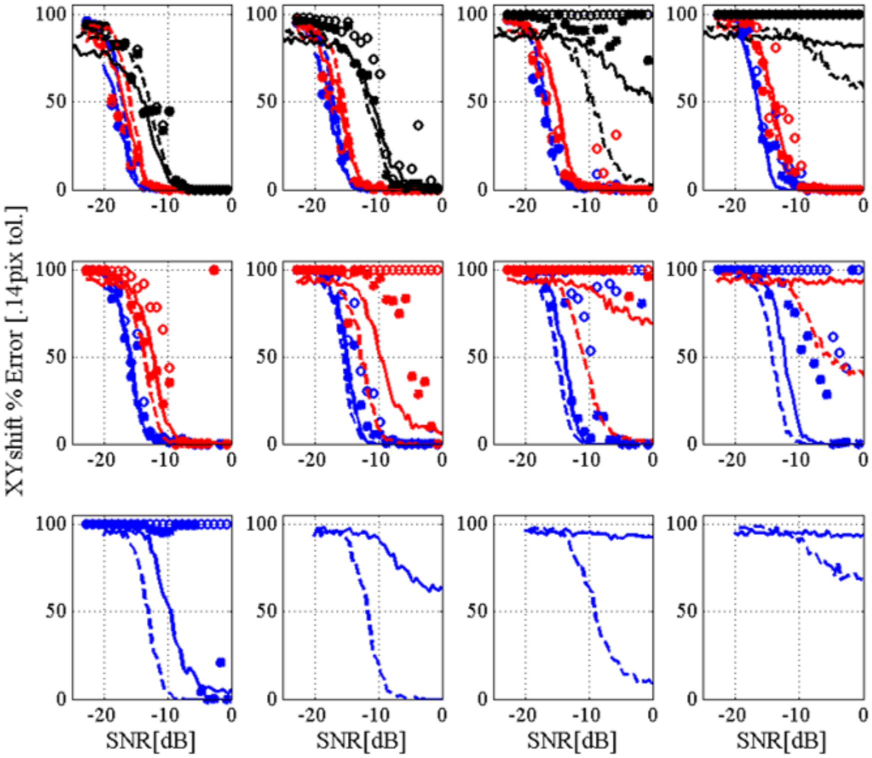

Figure 51: Direct Comparison of experiment benchmark with simulated sensitivity curves for baseline and enhanced CC registration. Data was only taken in experiment for 1-9 pixels of shift, but is shown here superimposed onto the full 12 pixels of shift in the simulation.

The sensitivity comparison above shows that the experiment and simulation are comparable out to only 2 pixels of shift. After that point, shown in the 3 pixel case for 5x5 support, the similarities diverge. For the 11x11 support, the simulation works out to 7 pixels of shift, but only 6 pixels of shift in the experiment, and at that shift, the experiment breaks at a much higher SNR. For 15x15 support, the same issue occurs with the experiment diverging in from the simulation lines with respect o SNR a the 7 pixel shift point, and completely breaking at only 9 pixels of shift.

The SNR differences are most likely due to a larger overall sparsity of the lab target. Due to the SNR being calculated volumetrically, sparser targets at equivalent SNR will have their signal dominated by singular targets, which are still registerable. The minimum error in the experiment is also significanly larger than in the simulation, the largest contributor to this effect was instability in the stage which caused a periodic variability in returned registration parameters about the mean value, and outside the overall tolerance used to calculate percent in error. Finally, the phase curvature of the collected fields was a likely cause of the experiment not registering to the full 9-12 pixels of shift in the high support case. The speckle evolution over large shift across the aperture which was not as pronounced in the simulation. Ideally, the apeture fields would not chanage at all between sub-apertures apart from the linear shift. This would mean the fields are very strongly correlated and would only cease to register once at extreme shifts. If the field is evolving, this has the effect of decreasing overal correlation amplitude between sub-apertures which has the same effect as one would get from shifting un-evolving fields further between sub-apertures. The effects of this with respect the sensitivity is an overall decrease of viable shift and SNR between registerable sub-apertures. The effects of field evolution can be simulated by applying a random and low power additional phase the simulated image volumes. This causes small field evolutions that remain largely correlated for small shifts, but not for larger ones, depending on the amplitude of random phase perturbations. A new sensitivity analysis through this simulation was done, and is directly compared with the expriment sentivity analyis by through a superimposed sub-plot shown in Figure 52

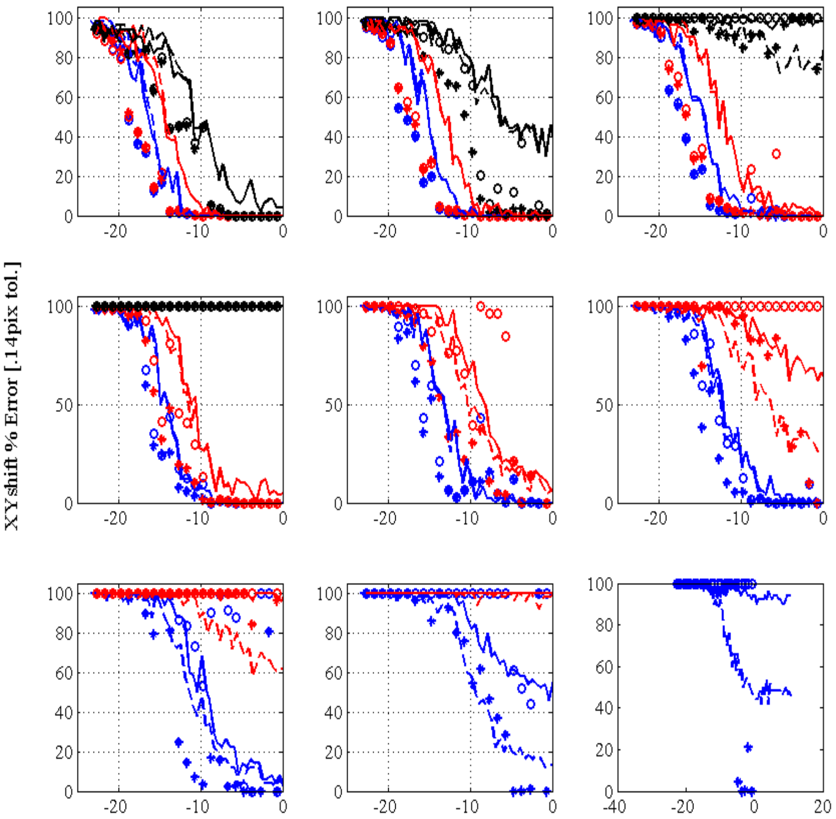

Figure 52: Comparison between phase perturbed simulated sensitivity and Experiment registration sensitivity:

By inducing small random phase variation between simulated sub-apertures, the regions of viable registration with respect to noise and shift are decreased and can closely emulate the results of experiment. From Figure 52, the 5x5 support is now only viable for 2 pixels of shift, the 11x11 support allows for 7 pixels of shift and the 15x15 only goes to 9 pixels of shift. This is a convincing case for the source of field evolution to be uncorrected phase errors at some point in the collection.

8.8 Experiment Conclusions and Future Work Suggestions

The experimental validation of the registration algorithm sensitivity analyses led to some interesting discoveries and solutions needed for a fielded system. To the best of the author's knowledge this is the first demonstration a 1.55 micron Flash-LiDAR coherent 3D imaging system utilizing temporal homodyne image plane detection. The detection format is novel and allows for the capture of a full 3D image, with phase information in under 1 second of acquisition time. Capturing the phase changes of the CPI allows for image registration of a slowly rotating target and this process was implemented in a sensitivity analysis utilizing a baseline CC 3D registration algorithm and an enhanced CC algorithm as outlined theoretically in Chapter 4 and implemented in simulation in Chapter 6. There were significant challenges in keeping the phase stable between LFM pulses and over the entirety of the CPI. Noise contributions from the stage, the table, and the timing system appeared to cause subtle evolutions of the aperture sampled field over the CPI which increased overall system sensitivity for the registration sensitivity analysis and decreased viable resolution gain from aperture synthesis. These effects were simulated and returned very similar results, concluding that subtle phase differences must be accounted for and compensated in a fielded system intended for 5-10 fold resolution gain.

Future work in this area would include addition of a monitor channel for post processing phase compensation. System improvements could be made to the laser and detector to better match a large range window target at a further overall range. Making the system monostatic would also have benefits (such as calibration through corner cubes), as would an extended analysis of support such as 30x30 pixels or larger. This would require a faster detector or lower pulse rate laser.

CHAPTER 9

SUMMARY AND CONCLUSIONS

Recent inclusions of aperture synthesis applications to optical wavelength LiDAR sensing modalities has motivated advances and studies in novel registration algorithms for 3D complex volumes collected from targets at range. The target and motion assumptions for this imaging scenario, allows for specialized algorithms to return the necessary cross-range and piston phase registration parameters for aperture synthesis, and two such algorithms were investigated and underwent a sensitivity analysis to characterize their utility.

As part of the analysis of 3D complex volume registration, the motion assumptions of the target of interest were expanded into a full theoretical mapping of target plane field to the aperture and image plane, following paraxial rotation transformation and phase mapping between the target and aperture. This analysis yielded a compact expression for field mapping that may be applied for simulated data volume generation either via aperture plane detection or image plane detection. These data volumes may be obtained experimentally through a coherent detection process utilizing a stretch-processed LFM waveform and processing the resulting detected sinusoidal signal to a complex valued data volume.

Once the complex data volume CPI is generated, the slow-time sampled volumes may be registered for use in aperture synthesis, and the means of accomplishing this through a mutual information approach or range-bin summed baseline cross-correlation approach was explored.

Mutual information is a common multi-dimensional registration technique with successful history in medical imaging and multi-modal remote sensing. By separating the complex volume to real and imaginary channels, MIRA can register complex volumes, is agnostic to data structure dimensionality and is naturally robust to noise. A sensitivity analysis comparison was done between 3D complex mutual information registration and a baseline CC algorithm which utilized coherent summation along the range bins for a complicated target. While this summation technique for CC is only viable for targets at range, it was found to be highly noise robust and it outperformed MIRA in every investigated imaging scenario with respect to SNR, shift and support. During this sensitivity analysis, some biases in the baseline CC registration process were found and an effort to correct for this was made. Despite the presence of these biases, the speed, robustness and ease of use of the baseline CC algorithm when compared with MIRA made it the preferred algorithm for long range low support 3D complex registration.

In the presence of a cross-correlation registration bias for low SNR and large inter-aperture shift, algorithm enhancements can expand the regions of viable CC registration. The enhanced algorithm requires a volumetric SNR measurement between the signal and an identical size noise volume, and the autocorrelation of the aperture used in the detection. By subtracting an estimate of the noise contribution to the correlation function, and compensating for autocorrelation effects on the signal, the algorithm can overcome biases at lower SNR and higher shift than the baseline algorithm.

Another sensitivity analysis comparing the baseline CC algorithm to the enhanced CC algorithm showed that the baseline CC could have its utility expanded with respect to total shift between apertures by 10-20% aperture shift, and by 1-5dB SNR dependent on total support and shift between sub-apertures. These effects are most pronounced at or beyond 50% shift between sub-apertures. This has the benefit of increasing the resolution gain of aperture synthesis for a fixed number of slow-time pulses, which has the potential for decreasing the power requirements of fielded SAL systems.

An experimental system was designed and tested for generating the complex 3D volumes used in a sensitivity analysis benchmark of the enhanced CC algorithm. The system was capable of consistent 3D range-azimuth-elevation and phase imaging, but system instabilities deviated the sensitivity analysis results from the simulation results. The enhanced algorithm still showed utility when applied to the experiment derived data but the deviations were too large to call it a true benchmarking.

9.1 List of original contributions

- Theoretical Field mappings for simulation use
    - Slowly rotating target at range mapped fields to apertures
    - Applied to aperture plane and image plane detection.
- Mutual Information Registration Study
    - Applied MIRA to complex 3D volumes and showed viable convergence
    - Directly compared 3D MIRA to 3D summed baseline CC in a sensitivity analysis
    - Developed efficient histogram technique for fast MATLAB mutual information calculation

- Improved Cross-Correlation Paper submitted to OSA Applied Optics

  - Showed baseline CC. algorithm improvements to SNR and aperture shift for synthesis registration.
  - Complete sensitivity analysis for parallel-pixel sparse target, low support imaging with respect to image registration.
  - Analytical basis for estimating and compensating registration biases overviewed

- Experiment System / validation
  - Successfully built a temporal homodyne parallel pixel ISAL system capable of 3D coherent imaging and field registration
  - Applied algorithms to experimental data, with theoretical comparison.
  - Assessed viability of experimental methods to real-world complex target long range ISAL systems.
  - To authors knowledge this is the first 1.55 μm Coherent Detection temporal homodyne Flash-LiDAR on an FPA

9.2 Suggested Future Work

Future work under consideration follows one of three categories: Thresholding studies applied to MIRA and CC algorithms to gauge their effects on registration performance and sensitivity, Experiment and processing improvements, and a study on registration algorithms for use in target pose estimation and velocity characterization.

The baseline CC algorithm averages out the noise contributions between range bins in a distributed target. Windowing out voxels that do not contribute to the CC signal will have a diminished effect when applied in tandem with this algorithm, but the full character of their effects has not been fully studied. It would be worth knowing an optimized combination of coherent range bin correlation summation, volumetric windowing and CC algorithm shift/SNR enhancements for a better overall algorithm. The effects of windowing could also be applied to a MIRA registration technique as part of a new sensitivity analysis.

The image plane detection temporal homodyne system could be improved in the hardware and in post-processing and then compared again with the theoretical sensitivity curves. Some improvements for this system would be an optimized LFM laser with a lower pulse repetition rate but the same bandwidth for a longer overall range window. This would improve the types of targets that could be tested. Similarly, more overall data available on the camera would increase the possible length of the CPI for longer synthetic apertures. From a processing perspective, some of the phase instabilities could be corrected through better use of the reference target to smooth the phase noise imparted by table vibrations. The noise in the timing system is more difficult to correct for but a modified 3D phase gradient autofocus technique is one such avenue.

Another possible goal to explore is the relationship between target state estimate and aperture synthesis. Registration algorithms in ISAL imaging can be used in tandem with a kalman filtering technique to estimate rotation rates of interrogated targets. These estimates may have some utility in low SNR aperture synthesis and better target imaging and identification

References

[1] M. Soumekh, Synthetic Aperture Radar Signal Processing, New York: Wiley-Interscience, 1999.

[2] G. Reynolds and D. Cronin, "Imaging with optical synthetic apertures," *JOSA,* vol. 60, no. 5, pp. 634-640, 1970.

[3] W. G. Carrara, R. S. Goodman and R. M. Majewski, Spotlight Synthetic Aperture Radar Signal Processing Algorithms, Norwood, MA: Artech House, 1995.

[4] D. N. e. a. M. U. Piracha, "Range resoleved lidar for logn distance ranging with sub-millimeter resolution," *Optics Express 18(7),* pp. 7184-7189, 2010.

[5] M. C. a. V. Koo, "FPGA-Based Chirp Generator for High Resolution UAV SAR," *PIER 99,* pp. 71-88, 2009.

[6] M. D. P. P. J. H. a. E. B. R.V. Chimenti, "Experimental verification of sparse frequency linearly frequency modulated ladar signlas modeling," *Optics Express 18,* pp. 15400-15407, 2010.

[7] J. Stafford, "Range Compression for Holographic Aperture Ladar," Dayton, OH, 2016.

[8] H. Palmeri, "Jointly Estimating 3D Target Shape and Motoin from Radar Data," Rensselaer Polytechnic Institute, Troy, NY, 2012.

[9] S. T. a. J. F. M. Guizar-Sicairoz, "Efficient subpixel image registartion algorithms," *Optics Letters,* no. 33, pp. 156-158, 2008.

[10] J. Stafford, "Range Compression for Holographic Aperture Ladar," Dayton, OH, 2016.

[11] B. F. J. Zitova, "Image Registration Methods: A Survey," *Journal of Image and Vision Computing,* vol. 21, no. 11, pp. 977-1000, 2003.

[12] M. A. Richards, Fundamentals of Radar Signal Processing, New York: McGraw-Hill, 2005.

[13] P. Viola and W. W. III, "Alignment by Maximization of Mutual Information," *International Journal of Computer Vision,* vol. 24, no. 2, pp. 137-154, 1997.

[14] F. M. e. al., "Comparative Evaluation of multiresolution optimization strategies for multimodality image registration by maximization of mutual information," *Medical Image Analysis,* vol. 3, no. 4, pp. 373-386, 1999.

[15] K. P. Wilkie, Mutual Information Based Methods to Localize Image Registration, Waterloo, Ontario: University of Waterloo, 2005.

[16] R. Wang and F. P. Ferrie, "Upsampling method for sparse light detection and ranging using coregistered panoramic images," *Journal of Applied Remote Sensing,* vol. 9, no. 095075, pp.

1-15, 2015.

[17] D. Fei, L. ShuiMing and S. Guozhong, "Mutual infomation based registration of LIDAR and optical imagfes," in *SPIE 6752 Geoinformatics 2007: Remotely Sensed Data and Information*, Nanjing, 2007.

[18] Q. Xie, Z. Wang and Z. Yang, "Polar Decomposition of Mutula Information Over Complex-Valued Channels," *IEEE Transaction on Information Theory,* vol. 60, no. 6, pp. 3163-3171, 2014.

[19] M. Guizar, *Efficient Subpixel Image Registration by Cross-correlation,* MathWorks Inc., 2013.

[20] J. W. Goodman, Statistical Optics, Hoboken, New Jersey: Wiley, 2015.

[21] A. Tippie, A. Kumar and J. Fienup, "High-resolution synthetic-aperture digital holography with digital phase and pupil correction," *Optics Express,* vol. 19, no. 13, pp. 12027-12038, 2011.

[22] J. W. Goodman, Introduction to Fourier Optics, Greenwood Village, CO: Roberts & Company, 2005.

[23] A. Kachelmyer, "Range-Doppler Imaging with a Laser Radar," *The Lincoln Laboratory Journal 3 (1),* pp. 87-118, 1990.

[24] e. a. W.J. Warren, "Simulating translation-induced laser speckle dynamics in photon Doppler velocimetry," *Applied Optics,* vol. 53, no. 21, pp. 4661-4668, 2014.

[25] J. C. a. B. Johnston, "Inverse Synthetic Apeture Radar Processing using Parametric Time-Freqnecy Estimators, Phase 1 Progress Report," 1997.

[26] R. Fenton, "A Ladar-Based Pose Estimation Algorithm for Determining Relative Motion of a Spacecraft for Autonomous Rendezvous and Dock," Logan, UT, 2008.

[27] C. Noviello, "Techniques for Inverse Synthetic Aperture Radar Imaging and Monitoring of Deformation with Differential Interferometric Synthetic Aperture Radar," Napoli, Italy, 2007.

[28] J. S. Q. L. a. Q. W. D. Lv, "3D pose estimation of ground rigid target based on ladar range image," *Applied Optics,* vol. 52, no. 33, pp. 8073-8081, 2013.

[29] J. S. Q. L. a. Q. W. D. Lv, "Model-based recognition of 3D articulated target using ladar range data," *Applied Optics,* vol. 54, no. 17, pp. 5382-5391, 2015.

[30] B. Horn, "Closed-form solution of absolute orientation using unit quaternions," *JOSA,* vol. 4, no. 4, pp. 629-642, 1986.

[31] J. MacMulland and G. Green, "Estimation of differential delay and differential Doppler when signal characteristics are unavailable," *SPIE,* vol. 1699, 1992.

[32] T. E. a. K. Matsuda, "Determination of the central position of roation of a rotating object by laser Doppler velocimetry," *Optical Engineering,* vol. 30, no. 11, Nov. 1991.

[33] J. Goodman, Speckle Phenomena in Optics: Theory and Applications, Greenwood Village, CO: Roberts & Company, 2005.

[34] J. W. Goodman, Statistical Optics, New York: John Wiley and Sons, Inc., 2000.

[35] W. Janos, "Speckle Correlation Time of Doppler Resolved Rotating Targets," *SPIE-Statistical Optics,* vol. 976, 1988.

[36] J. M. a. K. S. Schroeder, "Speckle from rough rotating objects," *Applied Optics,* vol. 27, no. 20, 1988.

[37] B. Goebel, R.-J. Essiambre, G. K. P. J. Winzer and N. Hanik, "Calculation of Mutual Information for Partially Coherent Gaussian Channels with Application to Fiber Optics," *IEEE Transaction on Information Theory,* vol. 57, no. 9, pp. 5720-5736, 2011.

[38] W. Carrara, R. S. Goodman and R. M. Majewski, Spotlight Synthetic Aperture Radar Signal Processing Algorithms, Norwood, MA: Artech House, 1995.

[39] T. J. Green, S. Marcus and B. D. Colella, "Synthetic-aperture-radar imaging with a solid-state laser," *Applied Optics,* vol. 34, no. 30, pp. 6941-6949, 1995.

[40] J. Dahl and Z. Barber, "Synthetic aperture ladar imaging demonstrations and information at very low return levels," *Applied Optics,* vol. 53, no. 24, 2014.

[41] M. Dierking and B. Duncan, "Holographic Aperture Ladar," *Applied Optics,* vol. 48, no. 6, pp. 1168-1177, 2008.

[42] M. Guizar-Sicairoz, S. Thurman and J. Fienup, "Efficient subpixel image registartion algorithms," *Optics Letters,* no. 33, pp. 156-158, 2008.

[43] S. Crouch, B. M. Kaylor, Z. Barber and R. R. Reibel, "Three dimensional digital holograpic aperture synthesis," *Optics Express,* vol. 23, no. 18, 2015.

[44] C. J. Pellizari, M. F. Spencer, J. Bos, S. Williams and S. E. Williams, "Performance Characterization of Phase Gradient Autofocus for Inverse Syntheic Aperture LADAR," in *Aerospace Conference IEEE*, Big Sky, MT. USA, 2014.

[45] J. Ricklin, B. Schumm and M. Dierking, "Synthetic Aperture Ladar for Tactical Imaging (SALTI) (Briefing Charts)," Universities of Space Research Association, Wright Patterson Air Force Base, 2007.

[46] S. T. a. J. F. M. Guizar-Sicairos, "Efficient sub-pixel image registration algorithms," *Optics Letters,* vol. 33, pp. 156-158, 2008.